SIGNAL ANALYSIS AND RADIOHOLOGRAPHIC METHODS FOR AIRBORNE RADIO OCCULTATIONS

A Dissertation
Submitted to the Faculty
of
Purdue University
by
Kuo-Nung Wang

In Partial Fulfillment of the
Requirements for the Degree
of
Doctor of Philosophy

Oct 2015
Purdue University
West Lafayette, Indiana

In loving memory of my grandmother, Jie-Yu Liu, who taught me how to live a life with her stories.

ACKNOWLEDGMENTS

I would like to thank my advisor, Professor James L. Garrison immensely for his guidance and support. Dr. Garrison is a brilliant scientist and a caring mentor always providing invaluable suggestions toward academic research as well as personal career development during my studies.

I am also thankful to my committee members, Professor Jennifer Haase, Professor Arthur Frazho, and Professor Michael Zoltowski for their help and advice. I want to give my special thanks to Professor Jennifer Haase, who always encourages me and is extremely patient with my awful language skill.

I would like to extend my gratitude to fellow student Brian Murphy, who generously offers his assistance and advice to move airborne RO forward. Also great thanks to Professor Feiqin Xie and his post-doc, Dr. Loknath Adikari for sharing their useful insight on this exciting project. I want to recognize former fellow students Paytsar Muradyan, Ulvi Acikoz, Tyler Lulich, Brian Ventre and all the other giants who made airborne RO technique come true. I am also grateful for all the discussions and encouragements from my lab mates Zenki Lin, Ben Ashman, Oscar Yang, Rashmi Shah, and Gary Lee.

I would like to acknowledge the National Aeronautics and Space Administration (NASA) for the support of 3-year research assistantship and National Science Foundation (NSF) for the flight campaigns experiments. I also want to thank Taiwan's Ministry of Education, ASTRA corporation, COSMIC workshop student travel grant, and Purdue Engineering travel grant for generous financial support.

Finally, I am truly grateful for my family and my fiancee's continuous support, tolerance and understanding. This journey is long and tough, but I'm lucky enough that all of you have never quit believing in me. I deeply appreciate your sacrifice and encouragement, and I love you all.

TABLE OF CONTENTS

Page

LIST OF TABLES

LIST OF FIGURES

Figure Page

ABBREVIATIONS

ARO	Airborne Radio Occultation
CL	Closed-Loop
COSMIC	Constellation Observing System for Meteorology, Ionosphere, and Climate
ECMWF	European Center for Medium Range Weather Forecasts
ERAI	European Re-Analysis Interim
EIRP	Equivalent Isotropically Radiated Power
FSI	Full Spectrum Inversion
GISMOS	GNSS Instrument System for Multistatic and Occultation Sensing
GNSS	Global Navigation Satellite System
GPS	Global Positioning System
GRACE	GRAvity recovery and Climate Experiment
GRS	GPS Recording System
GV	Gulfstream V
IGS	International GNSS Service
IMU	Inertial Measurement Unit
LEO	Low Earth Orbit
NASA	National Aeronautics and Space Administration
NSF	National Science Foundation
OL	Open-Loop
PLL	Phase Locked Loop
PM	Phase Matching
PREDICT	PRE-Depression Investigation of Cloud Systems in the Tropics
PRN	Pseudo-Random Number
PSR	Purdue Software Receiver

RF	Research Flight
RO	Radio Occultation
RH	Radio Holographic
SNR	Signal-to-Noise ration

ABSTRACT

Wang, Kuo-Nung PhD, Purdue University, Oct 2015. Signal Analysis And Radio-holographic Methods For Airborne Radio Occultations. Major Professor: James L. Garrison.

Global Positioning System (GPS) radio occultation (RO) is an atmospheric sounding technique utilizing the change in propagation direction and delay of the GPS signal to measure refractivity, which provides information on temperature and humidity. The GPS-RO technique is now operational on several Low Earth Orbiting (LEO) satellite missions. Nevertheless, when observing localized transient events, such as tropical storms, current LEO satellite systems cannot provide sufficiently high temporal and spatial resolution soundings. An airborne RO (ARO) system has thus been developed for localized GPS-RO campaigns. The open-loop (OL) tracking in post-processing is used to cross-correlates the received Global Navigation Satellite System (GNSS) signal with an internally generated local carrier signal predicted from a Doppler model and extract the atmospheric refractivity information. OL tracking also allows robust processing of rising GPS signals using backward tracking, which will double the observed occultation event numbers.

However, RO signals in the lower troposphere are adversely affected by rapid phase accelerations and severe signal power fading. The negative bias caused by low signal-to-noise ratio (SNR) and multipath ray propagation limits the depth of tracking in the atmosphere. Therefore, we developed a model relating the SNR to the variance in the residual phase of the observed signal produced from OL tracking, and its applicability to airborne data is demonstrated. We then apply this model to set a threshold on refractivity retrieval based upon the cumulative unwrapping error bias, to determine the altitude limit for reliable signal tracking. To enhance the SNR and decrease the unwrapping error rate, the CIRA-Q climatological model and pre-filtering of the signal residual phase are utilized to process the ARO residual phase. The more accurate modeled phase with less noisy received signal are shown to greatly reduce the bias caused by unwrapping error at lower altitude.

On the other hand, to process the superimposed signal at lower troposphere due to a highly variable moisture distribution, the Radio-Holographic (RH) methods such as Phase Matching (PM) have been adapted for ARO platforms to untangle the bending angle of each signal path. Under the assumption of spherically symmetric atmosphere, ARO PM using the Method of the Stationary Phase (MSP) can identify different subsignals and determine the arrival angle for each impact parameter. As a result, each subsignal can be distinguished and its correspnding bending angle can be retrieved without producing negative bias. The refractivity retrieval results using ARO PM are compared to those using traditional Geometrical Optics (GO) method, and the improvements are shown and discussed in the dissertation.

We applied this new methods on the received ARO data collected by the GNSS instrument system for multistatic and occultation sensing (GISMOS) in the PREDepression Investigation of Cloud systems (PREDICT) campaign in 2010. A data set of 5 research flights with 57 occultation events during the formation stage of the hurricane Karl are processed and analyzed. In this research, the refractivity fractional difference with ERA-I model can be maintained at an average 2% above a height of 2km with climatological model and ARO PM. Compared to the traditional geometrical optics (GO) method without climatological method assistance, the new ARO processing can effectively decrease the refractivity negative bias and significantly improve the retrieval depth of ARO.

1. Introduction

In a space mission, scientists always seek to extract the most information from the limited received data. Radio occultation (RO) is one of the atmosphere property retrieving technique by using the transient observations of the signals transmitted by spacecrafts, either setting or rising, passed behind the planet. When signals passes through the atmosphere of the planet, the radio wave's transmission is delayed and a bending of the propagation ray path is induced because of the atmospheric refraction. As a matter of fact, the refraction effect of the atmosphere is most observable with occultation signals received at low, even negative, elevations (Figure 1.1). The cumulative effect of this refraction is observed as a time-varying excess phase in the received signal. The RO method, which utilizes the excess phase observation for refractivity retrieval, was applied for the first time to the Mariner missions in 1964 to observe Venus's atmosphere. Despite followed by a series of interplanetary RO missions, this useful technique had never applied to the Earth until the development of the Global Navigation Satellite System (GNSS) in recent years [1].

1.1 GPS RO

Global Positioning System (GPS) RO is an active microwave sounding technique utilizing GPS signal, which has global coverage and all-weather penetration capability, as the signal source of RO. While GPS signal travels through the Earth atmosphere, its accumulated bending of the signal path can be extracted from the observed phase delay due to the gradients in the atmospheric refractivity field. By using the calculated bending angle, an atmospheric refractivity profile can be retrieved with inverse Abel-Transform [2] which will be introduced in Chapter 2 for a spherically symmetric atmosphere. This remote sensing technique is valuable to obtain high resolution

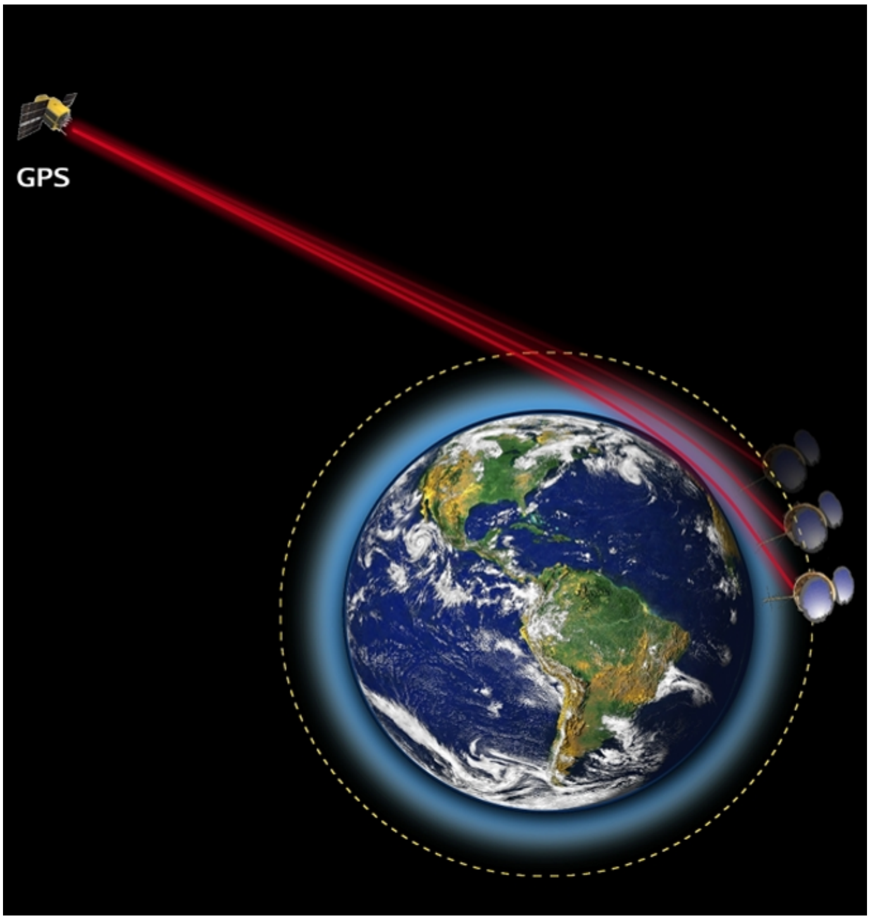

Figure 1.1. Radio occultation (RO) is the remote sensing technique to detect the bending of the ray path due to refraction, and retrieve the refractivity profile of the atmosphere. This figure is referenced from: http://www.cosmic.ucar.edu/ro.html

vertical profiles of atmospheric refractivity, which can then be inverted to retrieve atmospheric pressure, temperature or water vapor profiles [3].

$$N = k_1 \frac{P_d}{T} + k_2 \frac{e}{T} + k_3 \frac{e}{T^2} \tag{1.1}$$

where N is the atmospheric refractivity, k_1, k_2, and k_3 are three known constants, P_d is the dry air pressure, e is the water vapor pressure, and T is the temperature. The Refractivity N can be defined in terms of atmospheric refractive index:

$$N = (n - 1) \times 10^6 \tag{1.2}$$

This connection between the retrieved refractivity and the humidity and temperature information makes GPS RO a powerful system in forecast error reduction and global weather analysis. GPS RO was first demonstrated with the Global Positioning System/Meteorology (GPS/MET) mission in 1995. Initial results showed that the system accurately measured the temperature and had great potential for improving global weather prediction [4] [5]. Higher resolution and accuracy temperature information near the tropopause and the lower stratosphere can be obtained from the GPS RO observation compared to that calculated from infrared sounder measurements [6]. The experiments in forecast impact with assimilating the GPS RO refractivity and bending angle data show that GPS RO is able to provide a positive impact with the largest improvements in the Southern Hemisphere extratropics [7].

The success of GPS/MET has led to several new missions. The German Challenging Minisatellite Payload (CHAMP) and Argentinian Satelite de Aplicacionas Cientifcas-C (SAC-C) were both launched in 2000, and collected 400-500 soundings per day from 2001 to 2011 [8] [9]. The Constellation Observing System for Meteorology, Ionosphere, and Climate (COSMIC) consists of 6 microsatellites launched in April 2006. COSMIC had retrieved about 2,000 high-quality soundings daily on a global basis during its peak [10], and currently provides 1600 per day. GRACE, the Gravity Recovery and Climate Experiments, provides 150 per day [11]. The most recent GPS RO satellite program is METOP, operated by EumetSat, which will consist of 3 low earth orbit satellites in 2017 (2 have been launched as of August, 2014). The Global Navigation Satellite System (GNSS) Receiver for Atmospheric Sounding (GRAS) on METOP-A and METOP-B produce about 1200 measurements per day. [12] The first six satellites of COSMIC II will be launched in 2016 into low inclination orbits, to be followed by six more with inclined orbits in 2018 [13].

1.2 Airborne RO

Although with several spaceborne GPS RO missions in operation, the temporal and spatial density of observations provided by spaceborne receivers is still relatively sparse, and largely depends on the health status of the constellation. For example, the total number of spaceborne occultations has decreased to about 1600 per day compared to that of 3000 per day in year 2009 due to the malfunction of two satellites in the constellation. In addition, even with thousands of profiles daily GPS-low Earth Orbit (GPS-LEO) systems cannot provide dense sounding measurements in a specific area within a given time period due to the constraints of the orbits and limited number of available receiver satellites. Tropical storms, for instance, only ranged within a limited area and cannot be independently observed by spaceborne RO at the desired time. GPS RO measurements using a receiver inside the atmosphere was proposed [14] [15] to overcome this limitation. The airborne GPS radio occultation (ARO) system, which the receiver is installed onboard an airplane, is able to target a desired area to make a dense sampling over a specific period of time attributes to the mobility of the aircraft.

For this reason, the GNSS Instrument System for Multistatic and Occultation Sensing (GISMOS) has been developed for ARO experiment. GISMOS was designed to receive occulted GPS signals on the NSF/NCAR High-performance Instrumented Airborne Platform for Environmental Research (HIAPER) Gulfstream V (GV) aircraft which was firstly tested while flying over the southeastern United States in 2008 [16] [17]. A preliminary analysis of the data from the 2010 PRE-Depression Investigation of Cloud systems in the Tropics (PREDICT) field campaign, which aims to investigating the developing tropical cyclone, demonstrated the proof-of-concept. [18] The In this research, all the ARO data were also collected from PREDICT campaign which the flight path crossed the Caribbean Sea. The details of the signal processing, retrieval algorithms for ARO platform, and the hardware installation will be given in Chapter 2 and Chapter 3.

1.3 N-bias

In spaceborne RO, a large amount (more than several percent) of negative bias in refractivity retrieval can be observed at lower troposphere. Several sources causing the bias have been identified. The receiver tracking process using closed-loop (CL) tracking was one of the cause since CL suffers from lock losses when receiving SNR is low [19] [9]. Due to the improvement of the open-loop (OL) tracking implemented on ARO, the tracking bias has been largely reduced. Superrefraction [20] [21], which happens when vertical atmospheric refractivity gradients less than -158 km^{-1}, will causing the invalidity of the Abel-inversion and results in negative bias. In this research, we will focus on the two bias sources that are more significant than superrefraction - unwrapping error and multipath.

Because of its low elevation characteristic, the RO signal is normally in company with low signal to noise ratio (SNR). Low SNR will increase error rate in unwrapping the excess phase, and the same direction of the excess phase accumulation will cause negative bias in OL tracking result [22]. This bias is more significant in ARO, because the entire occultation period usually takes more than 10 minutes in ARO compared to that in 2 minutes of spaceborne RO, and the unwrapping error will accumulate much longer. The analysis and the impact assessment of low SNR to the resulting residual phase is described in Chapter 3, which is the also the journal paper accepted by Transactions on Geoscience and Remote Sensing, IEEE in 2015. On the other hand, the classical Geometric Optics (GO) inversion (Chapter 2) is currently applied on ARO to the partial bending angle calculation for refractivity retrieval, and the full theory is described in [23], [18] and [24]. GO method, however, is valid only under the assumption that the received signal is transmitted by single ray path through the atmosphere. Due to the highly variable moisture distribution in lower troposphere, the received ARO signal will suffer multipath effect by strong refractivity gradients in practice. The bending angle calculation with GO under severe interference will then produce multiple values at a given impact parameter because of GO's incapability of identifying superposition signals from multiple ray paths. The applied method maintaining monotonic property of partial bending angle - impact parameter function $\alpha'(a)$ by force causes the negative bias in refractivity retrieval [9]. In [22] it is shown that the low SNR and negative refractivity bias will eventually limit the height of ARO retrieval profile.

To enable refractivity retrievals when the assumption of single ray path is not valid and extend the penetration to lower altitudes, Radio-Holographic (RH) methods such as Full Spectrum Inversion and Phase Matching (PM) have been developed and applied to spaceborne RO measurements [25] [26]. These two methods utilizes Method of Stationary Phase (MSP) and Fourier Integral Operator (FIO) to take multipath effect into account. In this research we modified PM method to adapt to airborne version inverse Abel to decrease negative refractivity retrieval bias and extend valid ARO profile height. The spaceborne PM methods is reviewed in Chapter 4, which is the manuscript to be submitted to Journal of Geophysical Research, and its modification for ARO environment are also derived and described. The refractivity retrieval result using airborne RO experiment data is shown and the comparison between PM and traditional GO methods is also being discussed in Chapter 4. The summary and minor discussion will be provided in Chapter 5

2. Airborne Radio Occultation

2.1 ARO excess phase

As mentioned in Chapter 1, the signal ray path will be bent by refraction of the atmosphere and causing the path length deviate from the straight line, which is the path when the signal is transmitted in vacuum. Due to the constant signal transmitting frequency during the refraction, the extra signal path length compared to the straight line will be proportional to the increased amount of the received signal carrier phase. This excessive carrier phase, which called "excess phase", is caused by refraction in the neutral atmosphere and can be used to calculate the bending angle of the signal ray path. To extract the excess phase, the total carrier phase of the received ARO signal in terms of length can be modeled as [24]:

$$\Phi_R^T(t) = D_R^T(t) + \phi_R^T(t) + cC^T(t) + cC_R(t) + M_R^T + \varepsilon(t) \tag{2.1}$$

in which the D_R^T is the length of the geometric straight line in meters between the GPS satellite and the aircraft, and ϕ_R^T is the excess phase in meters caused by the neutral atmosphere refraction. c is the speed of light in meters per second, C^T is the satellite clock error, C_R is the receiver clock error, M_R^T is the distance caused by carrier phase integer ambiguity in the beginning, and ε is the error due to multipath and thermal noise. The superscript T and the subscript R refers to the transmitter and the receiver. The ionosphere and relativistic effects are ignored in this research due to their relatively small impact on the measurements at the height below aircraft's altitude.

The measurement of the total phase can be acquired with conventional GPS receivers using a Closed-Loop (CL) tracking method, such as a phase locked loop (PLL), delay-locked loop (DLL), frequency lock loop (FLL). CL tracking computes the signal from the correlation between the received signal and a local generated sine wave which its frequency is adjusted using a feedback loop. This feedback relies on continuous tracking from the previous time interval. These CL methods cannot track the low elevation signals, because of the rapid accelerations on the phase and signal fading caused by multipath propagation related to sharp gradients in the refractivity structure of the atmosphere [9]. The Open-Loop (OL) tracking method was proposed by [27] to extend the tracking duration and then implemented in spaceborne receivers, starting with SAC-C.

OL tracking computes the phase difference (defined as the residual phase) between that predicted by a Doppler model and the received signal. The Doppler model can be calculated as the sum of D_R^T and C^T using the aircraft position and velocity recorded by Applanix and the GPS satellite trajectory information in IGS orbit file [28]. As a result the OL tracking will give us the signal residual phase which removes the geometric straight line length and the transmitter clock error from the total phase measurement. OL tracking has been demonstrated in tracking of lower tropospheric occultations from orbiting receivers [29]. Doppler models for OL tracking of setting and rising occultations were derived for the SAC-C and COSMIC receivers [30]. The OL tracking algorithm described by Beyerle et al. (2002) [31] has been implemented in a software receiver and more details are provided in Section 3.2.

The differentiation of the signal residual phase can be calculated as:

$$f_{ED}(t) = \frac{d}{dt}\left\{\phi_R^T(t) + cC_R(t) + \varepsilon(t)\right\} \tag{2.2}$$

The frequency f_{ED} is called excess Doppler in which the integer ambiguity M_R^T has been removed by differentiation. For GPS satellites in high elevation, the received excess phase ϕ_R^T and the multipath effect which mostly happens in lower troposphere are assumed to be negligible. Therefore, we can further remove the receiver clock error C_R by subtracting the excess Doppler of high elevation GPS satellite from the occulted satellite excess Doppler that received at the same time. The resulting excess

Doppler can then be processed with bending angle retrieval algorithms which will be introduced in the next section.

2.2 Geometric Optics (GO) Method

Under the assumption of spherically symmetrical distribution of atmosphere refractivity, each ray in an occultation event can be identified by its impact parameter $a = nrsin\psi$, where n is the refractive index , r is the distance of each location on the ray path to the center of curvature and ψ is the incident angle. The impact parameter a will remain the same at each point on the same ray path. Bending angle profile $\alpha(a)$, which can be written as the function of the impact parameter, is valuable for its capability of being inverted to atmospheric refractivity. The relationship between the ray path bending angle and the excess Doppler obtained from the OL observations can be determined when a spherically symmetric atmosphere is assumed. The excess Doppler f_{ED}, which defined as the excessive received frequency due to longer signal path through atmosphere, is given by [32]

$$f_{ED} = \frac{1}{\lambda}\left[n_T\hat{k}_T \cdot \vec{v}_T - n_R\hat{k}_R \cdot \vec{v}_R - \hat{k} \cdot (\vec{v}_T - \vec{v}_R)\right] \tag{2.3}$$

where n_T is the refractive index at transmitter location, which equals to unity because of the locations of the GPS satellites are outside the Earth atmosphere. n_R is the refractive index at the receiver location. $\hat{k}_T$ and $\hat{k}_R$ are the unit vectors in the signal direction at the transmitter and at the receiver, respectively. $\hat{k}$ is the unit vector in the direction of the straight line from transmitter to the receiver. $\vec{v}_T$ and $vecv_R$ are the velocity vector of the transmitter and the receiver, respectively. The equation (2.3) can be written as the scalar form as equation (2.4) [33], where the geometry and the angles are illustrated in the figure 3.1.

$$f_{ED} = \frac{f_T}{c}\left\{V_T\left[n_T sin\left(\Omega_T - \beta_T\right) sin\left(\gamma_T\right) + \left(n_T cos\gamma_T - 1\right) cos\left(\Omega_T - \beta_T\right)\right]\right. \\ \left. -V_R\left[cos\left(\Omega_R - \beta_R\right)\left(n_R cos\gamma_R - 1\right) + n_R sin\left(\Omega_R - \beta_R\right) sin\left(\gamma_R\right)\right]\right\} \tag{2.4}$$

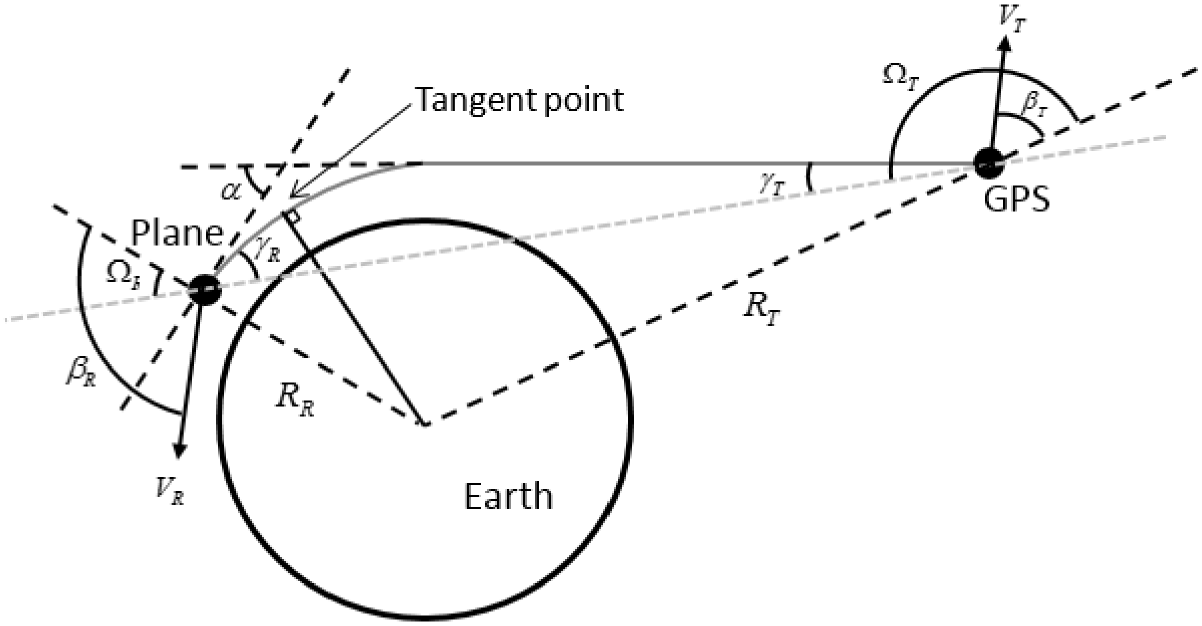

Figure 2.1. Geometric optics method to retrieve bending angle α from excess phase observation from GPS receiver. a is the impact parameter. V_T and V_R are the components of the transmitter and receiver velocity respectively in the occultation plane.

V_T and V_R are the magnitude of the velocity vector components lying in the plane of the occultation (formed by the transmitter, receiver, and the Earth's center of curvature) of the transmitter and the receiver respectively. The angles are also defined in the occultation plane. f_T is the transmitted signal frequency, and c is the speed of light. The refractive index at the receiver n_R can be obtained from the in situ measurement of air pressure and temperature at the location of the aircraft. The bending angle α can thus be expressed as

$$\alpha = \gamma_T + \gamma_R \tag{2.5}$$

On the other hand, Bouger's law [34] relates the angle of the ray path tangent to the atmospheric refractivity under the assumption of a spherically symmetric atmosphere.

$$n_T R_T sin\left(\Omega_T - \gamma_T\right) = n_R R_R sin\left(\Omega_R + \gamma_R\right) = a \tag{2.6}$$

R_T and R_R are the distances from transmitter and receiver to the center of curvature of the Earth. Equations (2.4) and (2.6) are then iteratively solved with repeated substitution of γ_T and γ_R. The bending angle α can be obtained with Equation (2.5) while γ_T and γ_R are converged, and its corresponding impact parameter a can be calculated by (2.6). To take the oblateness of the Earth into account, the GO is processed after the occultation geometry is transformed to coordinates centered on the local center of curvature of the Earth [35].

The geometry of an ARO system are shown in Figure 2.2. r_G and r_A are the distance from GPS transmitter and the aircraft receiver to the center of curvature of Earth, respectively. θ is the "open angle" between r_G and r_A at the center of curvature, and both r_G and r_A will change with respect to time during occultation period. a is the impact parameter of the signal path where $a = nrsin\psi$. To be noted as a special case, $a = nr$ at the point of closest approach of the ray to the Earth since the incident angle is the right angle, and the location of the point is called the "tangent point". The important difference in the retrieval algorithm for airborne vs. satellite RO is the contribution of the atmosphere above the aircraft. As shown in Figure 2.2(b), the signal path will bend even when the signal is received at positive elevation, while the occultation only occur at negative elevation for spaceborne platform. Under the spherical symmetry assumption, there is a corresponding positive elevation angle ray with the impact parameter a for every negative elevation angle ray having the same impact parameter. In ARO, this impact parameter a never exceeds $n_A r_A$. Therefore, The ARO sounding will range only from the surface to $n_A r_A$, and the unknown atmosphere structure above the aircraft is needed to be given as the refractivity at the aircraft altitude.

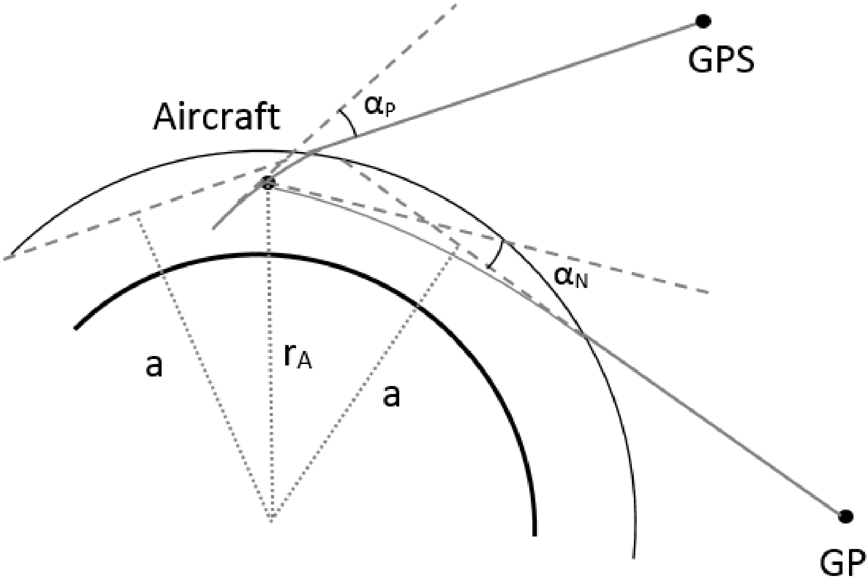

Figure 2.2. The ARO geometry for positive elevation and negative elevation. a is the impact parameter, r_A is the distance from the center of curvature to the aircraft and α_P and α_N are the bending angles in positive and negative elevation, respectively. As the figure shows, there is a corresponding positive elevation angle ray with the impact parameter a for every negative elevation angle ray having the same impact parameter

GO algorithm is capable of extracting the bending angle from positive and negative elevation ray path separately. An example of the bending angle result is shown in Figure 2.2(a). As a case of setting satellite, the occultation begins with positive elevation, which is the left side of the curve, and the increasing impact parameter. The impact parameter reaches its maximum when the elevation angle from the aircraft decreases to zero. The bending angle continuously increases while the satellite enter into negative elevation zone where the impact parameter start decreasing, and it will grows rapidly at the end of occultation. In GO, the impact parameter - bending angle pair are calculated by the order of the receiving time, and the impact parameter will monotonically increase and decrease with respect to time at positive and negative elevation, respectively. However, in multipath region the relationship between the impact parameter and time is no longer monotonic because the ray paths are twisted and will not be received in order. The non-monotonic impact parameter - bending angle curve as shown in Figure 2.3(a) is not usable for inverse Abel transform (Section 2.3). To retrieve the refractivity by using inverse Abel, an Ad-hoc correction should be applied on impact parameter measurement to make it monotonically increasing or decreasing by force as shown in 2.3(b). This correction can cause negative bias in bending angle calculation, which will be propagated to refractivity retrieval and cause large negative bias at lower troposphere.

2.3 ARO inverse Abel

Fjeldbo et al. (1971) [2] described the retrieval of atmospheric profiles using the Abel inversion, a fundamental principle for spaceborne RO which is shown in the following paragraph. In this reference, a typical geometry of the radio occultation is used and shown in Figure 2.3.

By using this geometry, two following properties can be found,

$$\theta + \phi = \psi + \pi/2 \tag{2.7}$$

$$tan\theta = \frac{rd\phi}{dr} \tag{2.8}$$

The incident angle θ for each point of the ray path can be derived by differentiating the Bougar's law.

$$d\theta = \frac{-a\left[n + r\frac{dn}{dr}\right]dr}{nr\sqrt{n^2r^2 - a^2}} \tag{2.9}$$

Using the equation 2.8 and the Bougar's Law the dynamic of angle ϕ can be acquired:

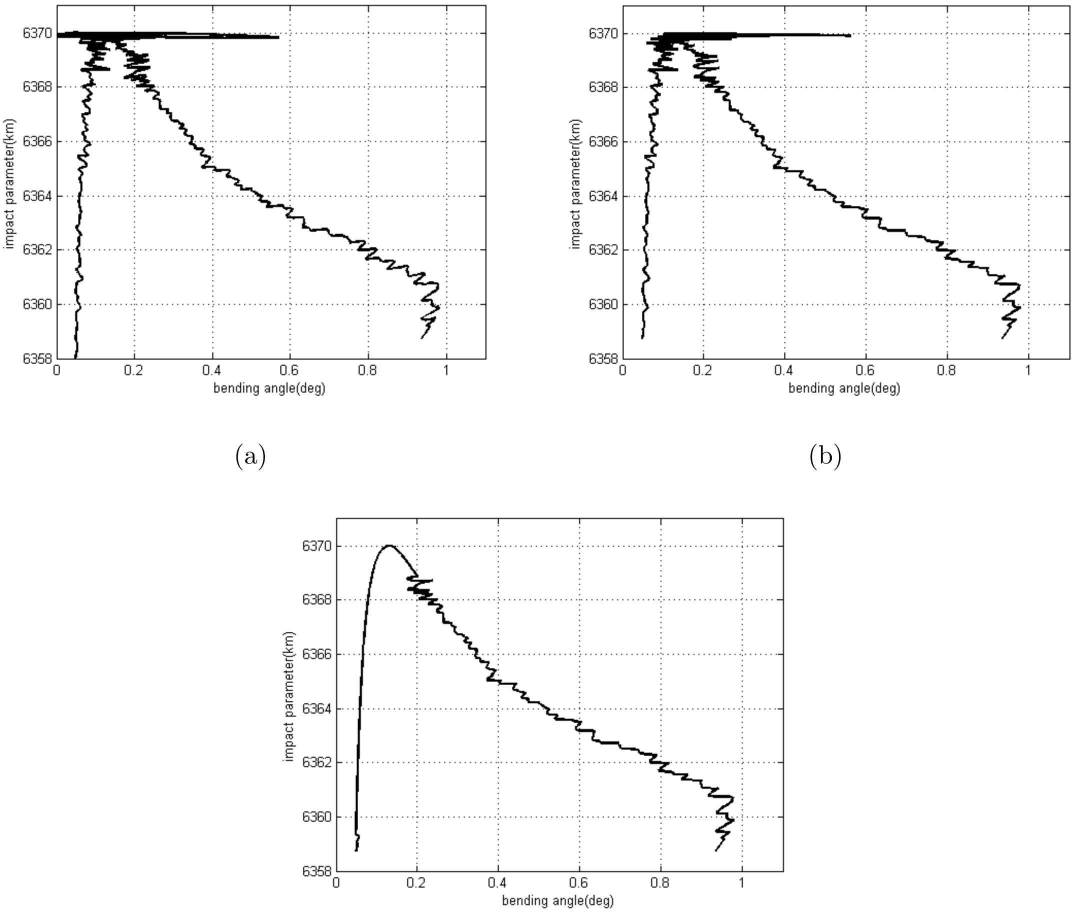

(a)

(b)

(c)

Figure 2.3. RF18 PRN25 bending angle retrieval by GO method. (a) The original retrieval from GO (b) The result after monotonic correction (c) The replacement with smoothed bending angle profile. The curve at left side in all three panels are in positive elevation, while the ones at the right side are in negative elevation. It can be observed that the impact parameter is not monotonic in (a), while it is corrected by an Ad-hoc method in (b).

$$d\phi = \frac{adr}{r\sqrt{n^2r^2 - a^2}} \tag{2.10}$$

Since we have the rate of the angle θ and ϕ, we can simply calculate the derivative of the angle ψ by using the equation 2.7.

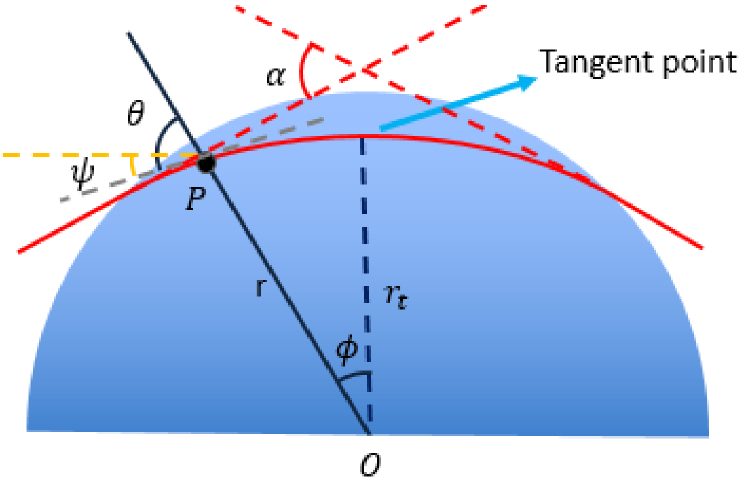

Figure 2.4. The RO geometry for Abel-inversion calculation. P is any certain point at the red ray path, θ is the incident angle, ϕ is the angle between $\overline{OP}$ and the tangent point vector, and ψ is the angle between ray path tangent line and the horizontal direction. r is the length of $\overline{OP}$, and α is the bending angle of the whole ray path.

$$d\psi = \frac{a}{n\sqrt{n^2r^2 - a^2}} \frac{dn}{dr} dr \tag{2.11}$$

ψ is the angle between the direction of the ray path at each point and the horizontal direction, hence, the half of the bending angle can be found by integrating the rate of ψ from tangent point to the one end of the ray path. the total bending angle α ca be expressed as:

$$\alpha(a) = -\int_{r_t}^{r_T} \frac{a}{n\sqrt{n^2r^2 - a^2}} \frac{dn}{dr} dr - \int_{r_t}^{r_R} \frac{a}{n\sqrt{n^2r^2 - a^2}} \frac{dn}{dr} dr \tag{2.12}$$

in which r_t is the radius of the tangent point in certain ray path, r_T is the radius of transmitter, and r_R is the radius of the receiver. In spaceborne case, the two terms in (2.12) are equal since the signal path will penetrate the atmosphere on both ends to the vacuum, and the bending portion is symmetric with the tangent point. The inverse of equation (2.12) has an explicit form:

$$n\left(x\right)=exp\left[\frac{1}{\pi}\int_{x}^{\infty}\frac{\alpha\left(a\right)}{\sqrt{a^{2}-x^{2}}}da\right] \tag{2.13}$$

The independent variable $x = nr$, will give the radius, r at which the refractive index $n(r)$ is retrieved. The equation (2.13) is called "inverse Abel" and it is widely used in RO technique for refractivity retrieval. Although both systems utilize GPS signal as the source of RO, the ARO retrieval method is different with spaceborne RO because ARO receiver always locate inside of the atmosphere and its ray path is not symmetric. Healy et al. (2002) [14] proposed a modified version of the Abel inversion for occultation measurements from a receiver within the atmosphere. In airborne RO, the signal path bending can be calculated in two different cases. For positive elevation, the bending directly comes from the ray path section between transmitter to the receiver, which doesn't pass the tangent point.

$$\alpha_P(a)=-\int_{r_R}^{r_T}\frac{a}{n\sqrt{n^2r^2-a^2}}\frac{dn}{dr}dr \tag{2.14}$$

On the other hand, the bending angle in negative elevation should be integrated from receiver to tangent point along with the section from tangent to transmitter.

$$\alpha_N(a)=-2\int_{r_t}^{r_R}\frac{a}{n\sqrt{n^2r^2-a^2}}\frac{dn}{dr}dr-\int_{r_R}^{r_T}\frac{a}{n\sqrt{n^2r^2-a^2}}\frac{dn}{dr}dr \tag{2.15}$$

The partial bending angle, which is a function of impact parameter, can then be defined as the subtraction of the positive elevation angle bending from the negative elevation angle bending. The result will be:

$$\alpha'\left(a\right)=\alpha_N\left(a\right)-\alpha_P\left(a\right)=-2\int_{r_t}^{r_R}\frac{a}{n\sqrt{n^2r^2-a^2}}\frac{dn}{dr}dr \tag{2.16}$$

This partial bending angle is the symmetric portion where the radius of the ray path r is decreased from r_R to r_t and back to r_R. To acquire the partial bending angle profile $\alpha'(a)$,the bending angle of the signal ray path during positive elevation $\alpha_P(a)$ and negative elevation $\alpha_N(a)$ need to be calculated by GO separately. We can invert the partial bending angle to produce refractivity profiles below the receiver height [14], [23]. The refractive index n can be calculated through the modified version ARO inverse Abel transform.

$$n\left(x\right) = n_A exp\left[\frac{1}{\pi}\int_{x}^{n_A r_A}\frac{\alpha'\left(a\right)}{\sqrt{a^2 - x^2}}da\right] \tag{2.17}$$

In which, n_A is the refractive index at the receiver, r_A is the distance between the receiver and the center of Earth curvature. As the equation 2.17 shows the upper limit of the ARO refractivity retrieval is at the altitude of the aircraft.

As shown in Figure 2.2(a) and Figure 2.2(b), the bending angle is noisy in both positive and negative elevation, and the noise level reaches the greatest at the top ($n_A r_A$) of the curve. To reduce the noise effects on partial bending angle calculation, a "smoothed" bending angle near top and positive elevation is used to replace the original noisy profile. The smoothed bending angle is generated by forward-Abel from Equation (2.15) and (2.14) with the smoothed refractivity profile. We can smooth the refractivity profile by fitting the log of the refractivity at the height below the aircraft, and extrapolate it to 30 km with scale height of 7 km [24]. The smoothing result is shown in Figure 2.3(c), where most of the noise is removed from top and positive elevation portion of the curve.

2.4 ARO hardware and flight campaign

As shown in Figure 2.5, GISMOS consists of a 10 Mhz GPS recording system (GRS), four Trimble NetRS survey quality dual frequency GPS receivers, an Applanix POS AV GPS/INS system, and a Symmetricom ExacTime600 timing receiver. The GRS, which was developed by the John Hopkins University Applied Physics Laboratory (JHU/APL), sampled both GPS L1 and L2 frequency signals and recorded the complex-interleaved data to disk drives with 1-bit quantization. Four Trimble NetRS GPS receivers used traditional closed loop (CL) tracking to track L1 and L2 signals. The accurate position and velocity of the aircraft are provided by Applanix 510 GPS Position and Orientation System for airborne vehicles (POS-AV) integrated with the inertial measurement unit(IMU). Fulfilled the requirement of 5 mm/s velocity precision [23] [36], the receiver trajectory is precisely known from the Applanix system's accurate navigation measurement. The Symmetricom ExacTime 6000 GPS frequency generator with an oven-controlled crystal oscillator (OCXO) provided a 10 MHz reference frequency for the GRS, POS AV and NetRS receivers.

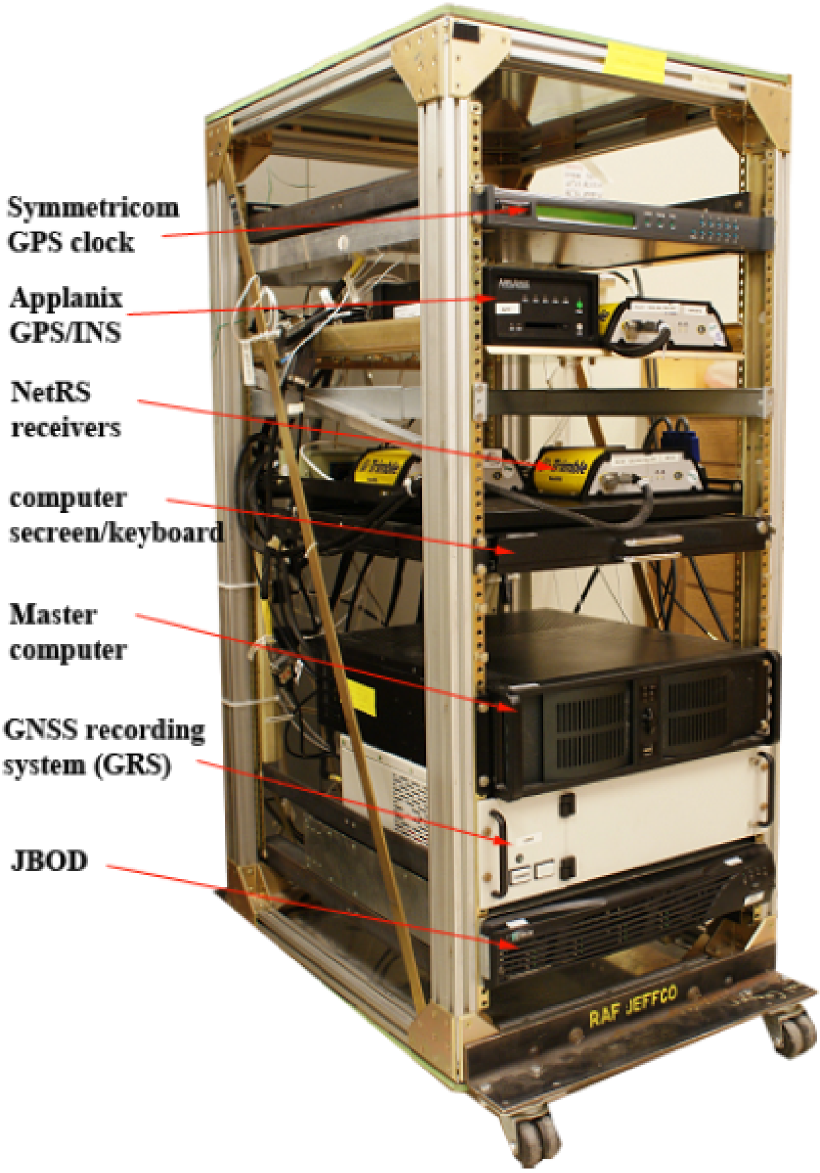

Figure 2.5. The GISMOS instrument rack

Seven antennas were mounted on the aircraft as shown in Figure 2.6. Three isotropic lower gain avionics antennas were placed on the top and both exterior sides of the aircraft. Two high gain antennas, which installed on the interior of the aircraft window on both sides of the aircraft, were designed for observing low elevation RO signals with their narrow vertical and wide horizontal gain pattern [16]. Two different polarized antennas, one righthand circularly polarized (RHCP) and one lefthand circularly polarized (LHCP), were also mounted on the nadir of the aircraft for making reflectometry measurements, which are not included in this research. The received signals from the high gain antennas on both sides were split to NetRS receivers and the GRS, which has one channel for each side. The third channel of the GRS can receive the signal from the top avionics antenna. In this dissertation, all the data were collected at field experiment with GISMOS installed on the National Science Foundation (NSF) Gulfstream-V (GV) research aircraft.

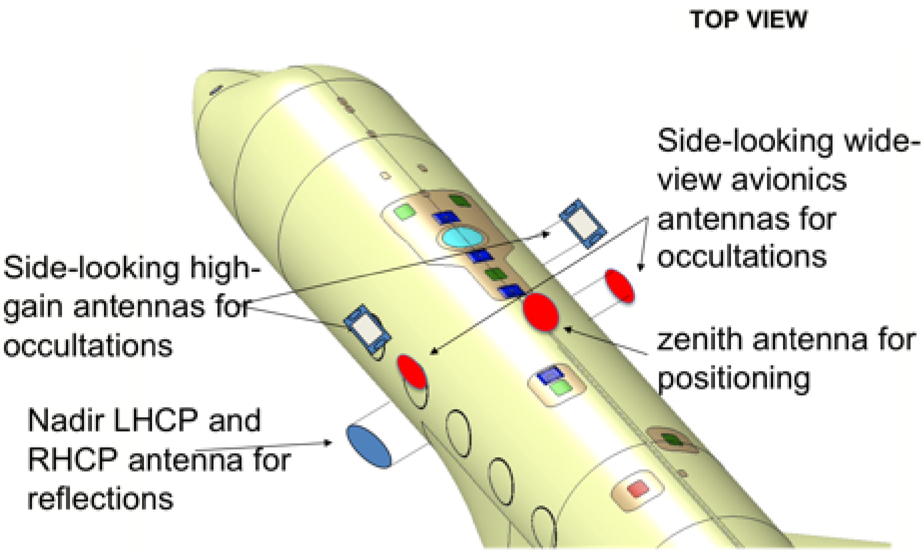

Figure 2.6. The placement of seven antennas on the aircraft. Three avionics antennas, two high gain antennas, and two opposite polarized antennas were mounted on the aircraft [37].

In this research the data sets recorded during the PREDICT campaign are analyzed. This flight campaign was planned to investigate the moisture development during the genesis phase of hurricane Karl [24], and the flight path will cross the Caribbean Sea while the cyclone system moved west during the campaign. The data sets collected from four research flights used in this research were recorded on 11 to 14, September 2010, day 254 to 257, and these four flights are numbered as RF16, RF17, RF18, and RF19, respectively. The flight trajectory are shown in Figure 2.7. As the Figure 2.7 shows, A modified lawnmower pattern was flown to regularly sample the development region except the avoidance of the deep convection locations. Significant amount of moisture at lower altitude is expected due to the tropical oceanic area that the flight pass through and the late summer the campaign in, which will cause multipath effect and interfere the RO measurements.

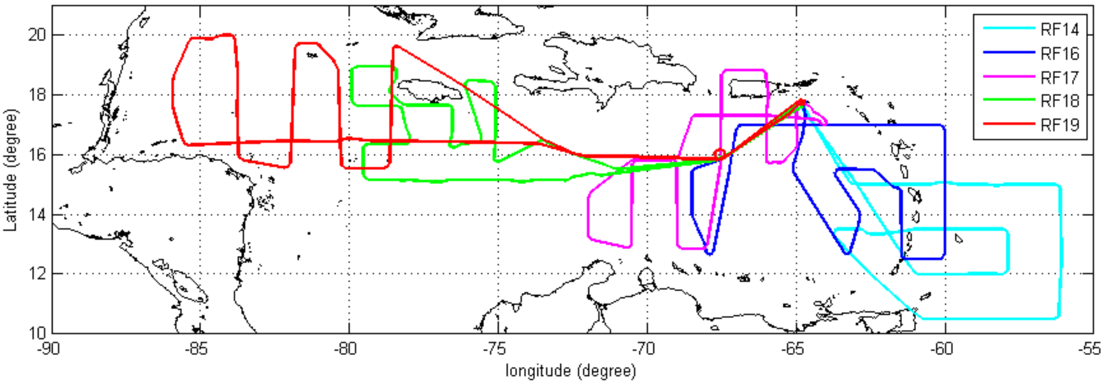

Figure 2.7. The flight path of all four research flights in PREDICT campaign which crossed the Caribbean Sea on 11 to 14 September, 2010 to observe the cyclogenesis process of hurricane Karl. Each flights are identified in different colors

3. Open-loop tracking of rising and setting GPS radio-occultation signals from an airborne platform: signal model and error analysis

(MANUSCRIPT: Accepted by IEEE Transactions on Geoscience and Remote Sensing)

ABSTRACT

Global Positioning System (GPS) radio occultation (RO) is an atmospheric sounding technique utilizing the change in propagation direction and delay of the GPS signal through the stratified atmosphere to measure refractivity, which provides information on temperature and humidity. The GPS-RO technique is now operational on the Constellation Observing System for Meteorology, Ionosphere, and Climate (COSMIC) constellation and several other Low Earth Orbiting (LEO) satellites. LEO systems, however, cannot provide high temporal and spatial resolution soundings necessary to observe localized transient events, such as tropical storms. An airborne RO (ARO) system has thus been developed for localized GPS-RO campaigns.

RO signals in the lower troposphere are adversely affected by rapid phase accelerations and severe signal power fading. These signal dynamics often cause the phase-locked loop in conventional GPS survey receivers to lose lock, limiting the availability of measurements in the lower troposphere. To overcome this problem, open-loop (OL) tracking in post-processing is used. In contrast to a conventional tracking loop, post-processed OL tracking cross-correlate the received Global Navigation Satellite System (GNSS) signal with an internally generated local carrier signal predicted from a Doppler model. OL tracking also allows robust processing of rising GPS signals, approximately doubling the number of observed occultations. An

approach for “backward” OL tracking was developed, in which the correlations are computed sequentially in reverse time so that the signal can be acquired and tracked at high elevations for rising occultations.

Ultimately, the signal-to-noise ratio (SNR) limits the depth of tracking in the atmosphere. We have developed a model relating the SNR to the variance in the residual phase of the observed signal produced from OL tracking. In this paper, we demonstrate the applicability of the phase variance model to airborne data. We then apply this model to set a threshold on refractivity retrieval based upon the cumulative unwrapping error bias, to determine the altitude limit for reliable signal tracking. We also show consistency between the ARO SNR and collocated COSMIC satellite observations, and use these results to evaluate the antenna requirements for an improved ARO system.

3.1 introduction

A radio occultation (RO) event occurs when the signal from a setting or rising GPS satellite is occulted by the Earth’s limb before arriving at a receiver. The atmosphere causes signal refraction which induces a bending of the ray path and delay in the signal. The cumulative effect of this refraction is observed as a time-varying excess phase in the received signal. Excess phase can be inverted to retrieve atmospheric refractivity, pressure, temperature or water vapor profiles [3]. GPS RO was first demonstrated with the Global Positioning System/Meteorology (GPS/MET) mission in 1995. Initial results showed that the system accurately measured atmospheric temperature and had great potential for improving global weather prediction [4] [5]. The success of GPS/MET has led to several new missions. The German Challenging Minisatellite Payload (CHAMP) and Argentinian Satélite de Aplicaciones Cientificas-C (SAC-C) were both launched in 2000, and collected 400-500 soundings per day from 2001 to 2011 [8] [9]. The Constellation Observing System for Meteorology, Ionosphere, and Climate (COSMIC) consists of 6 microsatellites launched in April 2006. These satellites retrieved about 2000 high-quality soundings daily on a global basis during the mission's peak [10], and currently provide 1600 soundings per day. The Gravity Recovery and Climate Experiment (GRACE) twin satellites provide 150 soundings per day [11]. RO profiles are also provided by two MetOp polar orbiting meteorological satellites, operated by the European Organisation for the Exploitation of Meteorological Satellites (EUMETSAT), with the third satellite scheduled to be launched in 2017. The Global Navigation Satellite System (GNSS) Receiver for Atmospheric Sounding (GRAS) on METOP-A and METOP-B produce about 1200 measurements per day. [12] The first six satellites of COSMIC II will be launched in 2016 into 24 degree inclination orbits, to be followed by six more with 72 degree inclination orbits in 2018 [13]. Even with thousands of daily profiles, GPS - Low Earth Orbit (GPS-LEO) systems cannot provide dense sounding measurements in a specific area within a given time period due to the constraints of the orbits and limited number of available receiver satellites. GPS RO measurements using a receiver onboard an airplane can overcome this limitation for localized regions.

Fjeldbo et al. (1971) [2] described the retrieval of atmospheric profiles using the Abel inversion, a fundamental principle for the RO technique. Healy et al. (2002) [14] proposed a modified version of the Abel inversion for occultation measurements from a receiver within the atmosphere. The airborne RO (ARO) proof-of-concept was demonstrated by Haase et al. (2014) [18] with flights of the GNSS Instrument System for Multistatic and Occultation Sensing (GISMOS) over tropical storms. In addition to commercial off-the-shelf geodetic receivers, GISMOS contains a GNSS signal recorder which enables OL tracking in post-processing.

The important difference in the retrieval algorithm for airborne vs. spaceborne RO is the contribution of the atmosphere above the aircraft. Under the assumption of spherical symmetry, for every positive elevation angle ray with the impact parameter a there is a corresponding negative elevation angle ray having the same impact parameter, $a = nr$, at the point of the closest approach of the ray to the Earth. In ARO, the partial bending angle, $\alpha'(a) = \alpha_N(a) - \alpha_P(a)$, defined as the difference of negative and positive elevation bending angles, can be inverted to produce refractivity profiles below the receiver height [14], [23].

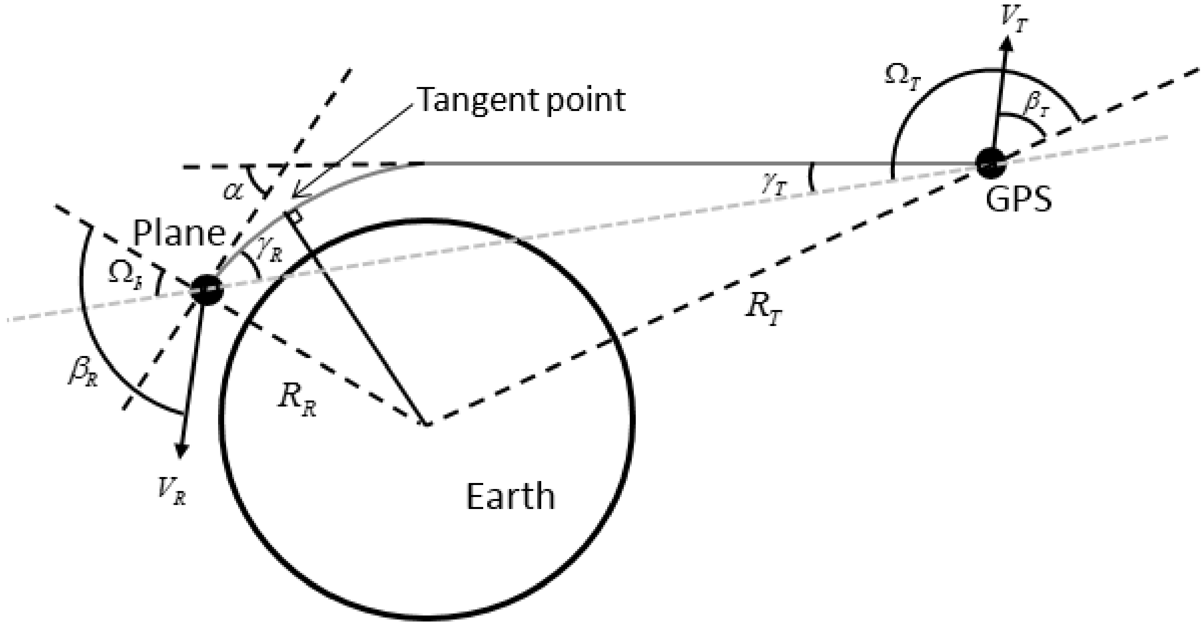

Figure 3.1. Geometrical parameters used in the retrieval of bending angle α from the excess phase observations from a GPS receiver onboard an aircraft. V_T and V_R are the transmitter and the receiver velocity components in the occultation plane. The bending angle, α, is the angle between the tangents to the raypath at the GPS transmitter and aircraft receiver.

The refractive index n can be calculated through the inverse Abel transform of the bending angle profile,

$$n(x) = n_R exp\left[\frac{1}{\pi}\int_{x}^{n_R R_R} \frac{\alpha'(a)}{\sqrt{a^2 - x^2}} da\right] \tag{3.1}$$

in which n_R is the refractive index at the receiver, and R_R is the distance between the receiver and the center of the Earth's curvature. The independent variable $x = nr$, will give the radius, r, at which the refractive index $n(r)$ is retrieved. The relationship between the ray path geometry and the excess Doppler obtained from the GPS observations of carrier phase, assuming a spherically symmetric atmosphere, is given by [33]:

$$f_{ED} = \frac{f_T}{c} \left\{ V_T \left[n_T sin\left(\Omega_T - \beta_T\right) sin\left(\gamma_T\right) + \left(n_T cos\gamma_T - 1\right) cos\left(\Omega_T - \beta_T\right) \right] \right. \tag{3.2}$$
$$\left. -V_R \left[cos\left(\Omega_R - \beta_R\right)\left(n_R cos\gamma_R - 1\right) + n_R sin\left(\Omega_R - \beta_R\right) sin\left(\gamma_R\right) \right] \right\}$$

where f_{ED} is the observed excess Doppler. V_T and V_R are the magnitudes of the transmitter and receiver velocity vector components in the occultation plane (formed by the transmitter, receiver, and the Earth's center of curvature). The angles are also defined in the occultation plane. The occultation geometry is transformed to coordinates centered on the local center of curvature of the Earth (Syndergaard (1998) [35]). Fig. 3.1 illustrates the ARO geometry [18]. f_T is the transmitted signal frequency, n_T is the refractive index at the transmitter location ($n_T = 1$) and c is the speed of light. In addition, assuming a spherically symmetric atmosphere, the Bouguer's law [34] describes the bending of the signal raypaths:

$$n_T R_T sin\left(\Omega_T - \gamma_T\right) = n_R R_R sin\left(\Omega_R + \gamma_R\right) = a \tag{3.3}$$

R_T and R_R are the distances of the transmitter and receiver from the Earth's center in the assumed spherical geometry. The bending angle α can thus be calculated as:

$$\alpha = \gamma_T + \gamma_R \tag{3.4}$$

The Doppler frequency is calculated by differentiating the excess phase observations. Equations (3.2) and (3.3) are then iteratively solved for the bending angle α and impact parameter a. The inverse Abel transform (4.3) is used to retrieve the atmospheric refractive index profile. The full theory for the geometric optics inversion of ARO measurements is described in Xie et al. (2008) [23] and Haase et al. (2014) [18].

Conventional GPS receivers, designed for navigation and surveying, use a closed-loop (CL) tracking method, such as a phase-locked loop (PLL), delay-locked loop

(DLL), frequency-locked loop (FLL) or some integrated combination of these to produce observations of the signal carrier phase and Doppler frequency. These CL methods cannot track the low elevation signals, because of rapid accelerations of the phase and signal fading caused by multipath propagation related to sharp gradients in the refractivity structure of the atmosphere [9]. The open-loop (OL) tracking method was proposed [27] to solve this problem and was implemented in spaceborne receivers, starting with SAC-C. OL tracking computes the phase difference (defined as the residual phase) between that predicted by a Doppler model and the received signal. CL tracking, in contrast, computes this error signal from the correlation between the received signal and the signal replica in which the Doppler is adjusted using a feedback loop. This error feedback relies on continuous tracking from the previous time interval. OL tracking has been demonstrated in tracking of lower tropospheric occultations from orbiting receivers [38] [30].

Doppler models for OL tracking of setting and rising occultations were derived for the SAC-C and COSMIC receivers [30]. Beyerle et al. (2006) [39] described the OL tracking algorithm that we have implemented in a software receiver. The OL tracking algorithm will be explained in Section 3.2. Since the OL technique does not rely on properties of the incoming signal, it will continue to produce phase estimates even after the signal has disappeared. Therefore, it is necessary to develop an objective method for determining the threshold below which the measurement is no longer valid in order to truncate the excess phase profile prior to applying the inverse Abel transform. We have developed a model relating the phase error to the signal-to-noise ratio (SNR) of RO signals, presented in Section 3.3. This model is used to carry out an error analysis of the residual phase calculation and unwrapping error rate, which can be used to derive a threshold on the minimum SNR for successful phase retrieval. In Section 3.4, the ARO recording instrument, the research flights, and the data are described. In Section 3.5 the performance of OL tracking for both rising and setting ARO measurements is assessed through comparison with the tracking threshold established by the SNR model.

3.2 Open-Loop Tracking

Following Beyerle et al. (2006) [39] the down-converted, or intermediate frequency (IF), RO signal $u\left(t\right)$ can be modeled as:

$$u\left(t\right) = A\left(t\right) D\left(t-\tau\right) p\left(t-\tau\right) exp\{j\left(2\pi f_{IF}t + \Phi\left(t\right) + \Phi_0\right)\} + \varepsilon\left(t\right) \tag{3.5}$$

Where $A\left(t\right)$ is the signal amplitude at the receiver, $D\left(t\right)$ is the data message, $p\left(t\right)$ is the baseband pseudorandom noise (PRN) code, f_{IF} is the intermediate frequency, $\Phi\left(t\right)$ is the time-varying total phase, τ is the time of travel delay, Φ_0 is the initial phase and $\varepsilon\left(t\right)$ is Gaussian white noise. This model includes only one visible satellite. The noise term $\varepsilon\left(t\right)$, however, could include multiple-access noise due to the presence of other GPS satellite signals. For the GPS C/A code on the L1 signal, $D\left(t\right)$ and $p\left(t\right)$ use binary phase shift key (BPSK) modulation at nominal rates of 50 Hz and 1.023 MHz, respectively. The Doppler frequency, including both the geometric and excess Doppler effect (3.2) of the signal, is the derivative of the time-varying phase:

$$f_D\left(t\right) = \frac{1}{2\pi}\frac{d\Phi(t)}{dt} \tag{3.6}$$

Closed-loop receivers track the incoming carrier signal by correlating it with a replica signal generated locally by the receiver. The Numerically Controlled Oscillator (NCO) frequency is steered toward the incoming signal frequency with a discriminator which monitors phase deviations between the incoming and local signals. By using feedback control from the error discriminator function, the NCO can adjust the rate of the local reference code and carrier to maximize the correlation and maintain a lock on the signal.

The OL tracking uses a local signal replica generated from a reference Doppler model. Cross-correlation of the local and the received signals produces an observation of the phase difference between these two, defined as the residual phase. In contrast to CL tracking, this local signal model is not adjusted based upon the observed phase difference. The positions and velocities of the receiver and transmitter must be known to a high degree of accuracy in order to generate the local signal for OL tracking. Post-processed satellite orbits are available from the International GNSS Service (IGS) and accurate position, velocity, and attitude solutions for the aircraft are produced by the use of GPS/Inertial Navigation System (GPS/INS). Airborne receivers can record a much larger volume of raw data for post-processing by OL tracking, compared to spaceborne receivers which are limited by telemetry bandwidth. For this reason, a software-defined radio (SDR) approach will be used [40] [16], in which the full spectrum of IF signals is analyzed. This system has a unique benefit that many techniques for improving the tracking can be tested, and reapplied to the raw recorded data.

3.2.1 Residual Phase

The total phase, $\Phi(t)$, of the received GPS signal is the sum of the phase due to the changing geometry between the transmitter and receiver, $\Phi^G(t)$, and the excess phase due to refraction in the atmosphere, $\Phi^E(t)$.

$$\Phi(t) = \Phi^G(t) + \Phi^E(t) \tag{3.7}$$

The OL tracking correlates the received signal with a local signal generated from a model prediction of the phase, $\Phi^M(t)$. The difference between the total and the predicted phase is defined as residual phase, $\Phi^R(t)$.

$$\Phi^R(t) = \Phi(t) - \Phi^M(t) \tag{3.8}$$

The residual phase is the argument of the complex result of cross-correlating the local and received signals, as will be shown in section 3.2.4. The model-predicted phase should be close enough to the true phase for the cross-correlation to give a valid observation. For the spaceborne case, it is necessary to include an initial prediction (from climatology) of the excess Doppler due to the atmosphere when computing $\Phi^M(t)$ in order to reduce the Doppler difference to within $\pm 15-20$ Hz [29]. For ARO, the atmospheric excess phase is accumulated over a longer time period (approximately 10 minutes) caused by much lower aircraft velocity (about 230 m/s) relative to that of the LEO spacecraft (about 7.5 km/s). Therefore, the difference between the Doppler produced due to changing geometry and the true Doppler is expected to be less than 6 Hz and remain within the range of $\pm 15 - 20$ Hz. Because the pre-recorded signal is sampled at 10 MHz and the cross-correlation is calculated at this data rate, the integration interval can be varied from 1000 Hz to 50 Hz to optimally increase SNR while easily remaining within this expected range. Atmospheric climatology is thus not included in our Doppler model. The excess phase is therefore simply the residual phase,

$$\Phi^{E}(t) = \Phi^{R}(t) \tag{3.9}$$

and our estimate of the excess phase will be taken directly from the residual phase produced from OL tracking. This will then be differentiated as in (3.6) to produce a bending angle profile through (3.2) and (3.3), and a refractive index profile through the inverse Abel transform (4.3).

3.2.2 Doppler Prediction

The model phase history, $\Phi^{M}(t) = \Phi^{G}(t)$, is computed by integrating the predicted Doppler time series. The predicted Doppler frequency is generated by calculating the relative motion between the transmitter and the receiver. The receiver position and velocity are determined by the GPS/INS [41] in GISMOS, and precise GPS satellite position data are obtained from the IGS daily orbital files [28]. Interpolation of the IGS data is required, since the position and velocity are required at a 1 kHz update rate and the satellite positions are provided at 15 minute intervals. A degree n polynomial is used for this interpolation [42].

$$P_k\left(t\right) = \mu_0^k + \mu_1^k t + \cdots + \mu_{n-1}^k t^{n-1} + \mu_n^k t^n, \qquad k = x, y, z \tag{3.10}$$

$P_k(t)$ represents the three components of the satellite position in the Earth-Centered Earth-Fixed (ECEF) reference frame. Velocity in the ECEF reference frame can be determined by differentiating (3.10).

$$\frac{dP_k}{dt}(t) = \mu_1^k + 2\mu_2^k t + \cdots + (n-1)\,\mu_{n-1}^k t^{n-2} + n\mu_n^k t^{n-1}, \qquad k = x, y, z \tag{3.11}$$

The optimal degree for the interpolation polynomial has been found to be between 9 and 13 [42]. A degree of 10 is chosen in this work. The relative position and velocity vectors between the transmitter and the receiver are then used to compute the model Doppler frequency, $f^M(t)$. This is then integrated from the start of occultation, t_0, to generate the model phase $\Phi^M(t)$:

$$\Phi^M(t) = 2\pi \int_{t_0}^{t} f^M(t')dt'. \tag{3.12}$$

3.2.3 Code Delay Prediction and Wipe-off

Code wipe-off is the removal of the PRN code modulation from (3.5), leaving only the carrier. This is accomplished through multiplying $u(t)$ by the PRN code $p(t-\tau_M)$ at the model-predicted delay, τ_M. $p(t)$ is generated by a published algorithm with a period of 1023 chips [43]. The PRN code $p(t)$ requires that the code delay τ_M be predicted within one sample ($\approx 30\ m$ for the 10 MHz sample rate). We will assume that the PRN code $p(t)$ will be aligned in code delay τ_M close enough, such that the product of the received and model-predicted codes approximately equals unity, $p(t-\tau)p(t-\tau_M) \approx 1$. Code wipe-off produces the "de-spread" signal $u^{DS}(t) = u(t)\,p(t-\tau_M)$.

$$u^{DS}(t) = A(t)\,D(t-\tau)\,exp\left\{j\left(2\pi f_{IF}t + \Phi(t) + \Phi_0\right)\right\} + \varepsilon^{DS}(t) \tag{3.13}$$

As the excess phase increases, this alignment will not be maintained using a geometric model without any atmospheric climatology included, and the average of the code product will decrease slowly. The rate of decrease is expected to be slow enough such that the average will remain constant over the integration time, with the net effect of a decrease in the apparent amplitude $A(t)$. The subsequent analysis would remain correct, with an effective reduction in SNR due to the code mis-alignment. $p(t)$ only takes values of ± 1 at nearly equal probability, thus the noise in the de-spread signal, $\varepsilon^{DS}(t) = p(t - \tau_M)\,\varepsilon(t)$, will have the same power as $\varepsilon(t)$.

The model-predicted code delay is computed by integrating the predicted Doppler model. CL tracking must be performed on the signal segment when the satellite is at high elevation to provide the initial code delay and Doppler value. In case of a rising occultation, the SNR at the start of the occultation is too low for acquisition and CL tracking. To overcome this difficulty, a "backward tracking" method [37] was developed to initialize the CL tracking using the signal at the end of the occultation where the signal power is sufficiently high. After signal acquisition and CL tracking in this manner, the rising satellite signal is then processed in reverse time, as described in section 3.2.4.

Cross correlation of $u^{DS}(t)$ with a signal replica is computed over a finite time interval, T_I, which must start and end on the edge of a C/A code cycle (1023 chips). In discrete time, this interval is a finite number of samples, representing one complete Doppler-compensated code cycle.

To calculate the code delay, τ_M, at the start of each cycle we also need the actual code rate f^A (chips/sec), which can be determined from the predicted Doppler frequency f^M. The predicted Doppler at the beginning of the time index m, $f^M[m]$, is computed at discrete steps in each millisecond . f_{L1} is the L1 signal carrier frequency in the absence of Doppler (1575.42 MHz).

$$f^A[m] = f^N\left(1 + f^M[m]/f_{L1}\right) \tag{3.14}$$

f^N is the nominal code rate, 1.023 MHz for the C/A code [44]. With the actual code rate we can calculate the samples per code cycle $N[m]$ (a real number),

$$N[m] = \left(1023\frac{chips}{cycle}\right)\left(f^S\frac{samples}{second}\right)\left(\frac{1}{f^A[m]}\frac{second}{chips}\right) \tag{3.15}$$

where f^S is the sampling rate of the recorder (10 MHz). Two numbers are used to define the code delay; the index location $l[m]$ and the fractional offset $d[m]$. $l[m]$

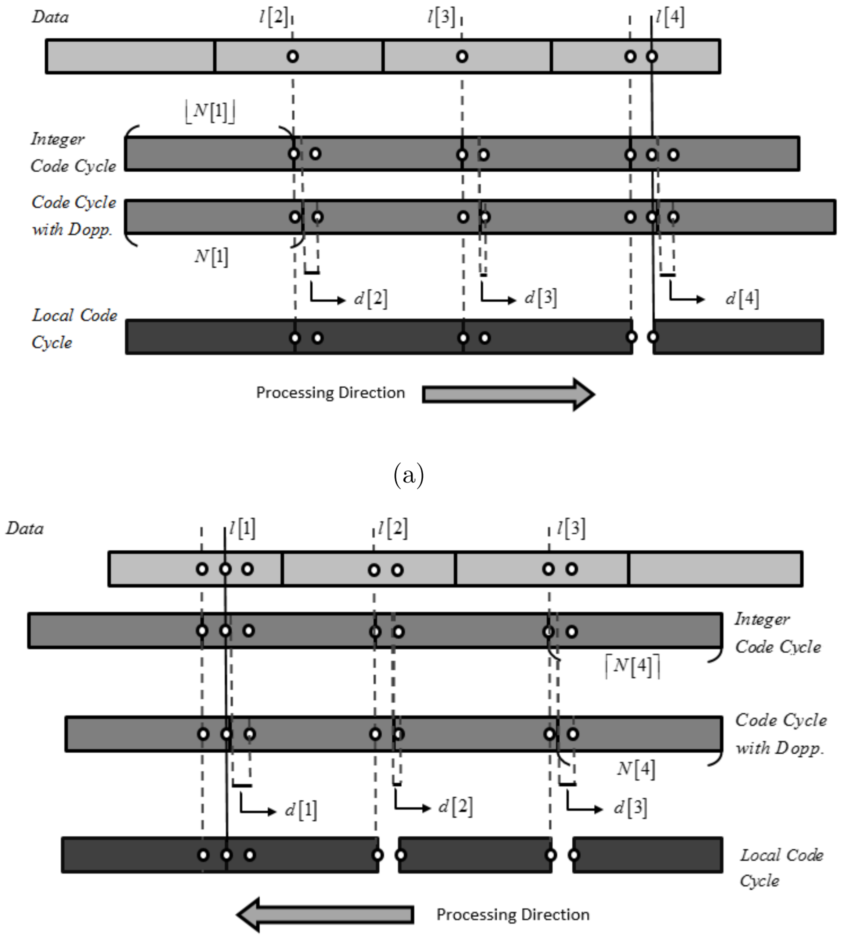

(a)

(b)

Figure 3.2. The calculation of the code delay. Each block is the length of a code cycle. Increased or decreased cycle length is due to the Doppler. To cross-correlate the samples within a code cycle we adjust $d[m]$ and $l[m]$ for location reference as the start of the correlation in (a) Forward tracking and (b) Backward tracking. Note that the fractional offset $d[m]$ for both forward and backward tracking ranges from 0 to 1, and decreases with each integration until it reaches a negative value, at which point a sample is skipped to re-align the integration with the code cycle in the received signal.

is a positive integer indicating the location of the IF signal sample where the code cycle edge occurs. $d[m]$ is the fraction of a sample indicating the offset of the code phase at the beginning of the correlation interval.

As Fig. 3.2 shows, the code cycle length changes when we take Doppler into account. Normally, the code cycle length extension does not exceed IF sampling time (1×10^{-7}sec), and the next cycle starts at the same sample in the next millisecond. To ensure the IF data with Doppler and the replica code cycle have the same phase in the next interval, the fractional offset $d[m]$, which, after initializing it with CL tracking, is then decreased each code cycle to align replica code phase with IF data code phase. In this way, $d[m]$ and $l[m]$ are accumulated and used to adjust the partial code phase in successive integrations. In forward tracking (setting occultation case),

$$d[m+1] = d[m] - (N[m] - \lfloor N[m] \rfloor) \tag{3.16}$$

$$l[m+1] = l[m] + \lfloor N[m] \rfloor \tag{3.17}$$

Here $\lfloor\ \rfloor$ is the greatest integer, or "floor", function. For forward tracking, the index location moves to the next sample when the fractional sample reaches a negative value.

$$d[m+1] = d[m] - (N[m] - \lfloor N[m] \rfloor) + 1 \qquad if \quad d[m+1] < 0 \tag{3.18}$$

$$l[m+1] = l[m] + \lfloor N[m] \rfloor + 1 \qquad if \quad d[m+1] < 0 \tag{3.19}$$

For backward tracking (rising occultations), the integration is in reverse, and the fractional offset $d[m]$ and index location $l[m]$ are updated as:

$$d[m-1] = d[m] - (\lceil N[m] \rceil - N[m]) \tag{3.20}$$

$$l[m-1] = l[m] - \lceil N[m] \rceil \tag{3.21}$$

Here $\lceil\ \rceil$ is the greatest integer plus 1, or "ceiling", function. If fractional offset $d[m]$ decreases below zero, the index location moves to the next sample.

$$d[m-1] = d[m] + (N[m] - \lfloor N[m] \rfloor) \qquad if \quad d[m-1] < 0 \tag{3.22}$$

$$l[m-1] = l[m] - \lfloor N[m] \rfloor \qquad if \quad d[m-1] < 0 \tag{3.23}$$

The m^{TH} discrete-time correlation described in the next section is performed over an integer number $\lfloor N[m] \rfloor$ of samples between indices $l[m]$ and $l[m+1]$. Fig. 3.2 shows this process for both forward and backward processing.

3.2.4 Carrier Wipe-off

The next step in OL tracking is to correlate $u^{DS}(t)$ with a local signal $v(t)$ generated using the model phase, $\Phi^{M}(t)$.

$$v(t) = exp\left\{j\left(2\pi f_{IF} t + \Phi^{M}(t)\right)\right\} \tag{3.24}$$

We integrate over time T_I to produce the complex correlation sum.

$$z[m] = \frac{1}{T_I}\int_{t[m]}^{t[m]+T_I} u^{DS}(t)\, v^{*}(t)\, dt \tag{3.25}$$

The integration time T_I is set to one period of the PRN code, as described above. $t[m]$ is the start time of this interval which equals $l[m]/f^{s}$. In practice, we implement (3.25) on the discrete-time $u^{DS}(t)$ by sampling $v(t)$ at $f^{S} = 10$ MHz and calculating the discrete sum,

$$z[m] = \sum_{b=1}^{l[m+1]-l[m]} u^{DS}[b + l[m]]\, v^{*}[b,m] \tag{3.26}$$

where the local signal

$$v[b,m] = exp\left\{j\left[2\pi\left(f_{IF} + f^{M}[m]\right)\left(\frac{b}{f^{S}}\right) + \Phi^{M}[m]\right]\right\} \tag{3.27}$$

is generated at sample index b assuming a constant Doppler $f^{M}[m]$ over the integration time T_I. CL tracking is applied to 30 sec of high-elevation, high SNR data at the beginning of a setting occultation or the end of a rising occultation, to detect the data bit edge and to determine the initial Doppler frequency f^M. The index location $l[m]$ and fractional offset $d[m]$ are also initialized by determining the integer and fractional parts of the code delay τ^M at the last integration interval of CL tracking.

We substitute (3.13) and (3.24) into (3.25) to produce a measurement of the average residual phase at the beginning and at the end of the interval.

$$z[m] = D[m]A[m]\text{sinc}\left(\pi f^R[m]T_I\right)\exp\left\{j\left(\frac{\Phi^R[m]+\Phi^R[m+1]}{2}\right)\right\} + \varepsilon^z[m] \quad (3.28)$$

The effect of the error in the Doppler model is present in the *sinc* function, which would reduce the post-correlation SNR for large residual Doppler, having a null at $f^R T_I = 1$. Equation (3.28) also assumes that the value of the data bit $D[k]$ remains the same over the integration time (through aligning the bit edge with a starting index $l[0]$), and that the signal amplitude $A(t)$ does not fluctuate significantly over this time. For backward tracking, this algorithm remains the same, but the correlation of each code cycle is performed starting at the latest time for which OL tracking is applied, to the beginning of the occultation event. Equation (3.26) is thus identical for both forward and backward tracking, with m increasing in the forward method but decreasing in the backward method.

3.2.5 Residual Phase Calculation

The complex correlation $z[m]$ from (3.25) is coherently summed over 1 data bit (approximately 20 ms), reducing the data rate from 1 KHz to 50 Hz.

$$\bar{z}[k] = \sum_{m=20(k-1)+1}^{20k} z[m] \quad (3.29)$$

This phase of $\bar{z}[k]$ is an estimate of the average residual phase within the one data bit interval with an increase in the SNR by a factor of $\sqrt{20}$ over (3.28).

$D[m]$ is assumed to be constant when the summation is performed across a single data bit period. This is assured by initializing the index k at the data bit edge, first found through the CL tracking initialization. $\bar{i}[k]$ and $\bar{q}[k]$ are the in-phase (real) and quadrature (imaginary) components of $\bar{z}[k]$.

$$\bar{z}[k] = \bar{i}[k] + j\bar{q}[k] \tag{3.30}$$

An estimate of the residual phase is then extracted from $\bar{i}[k], \bar{q}[k]$ by using a four-quadrant *arctangent* function. The data bit $D[k]$ is required for the determination of the residual phase, and it can be obtained from an external source of global GPS tracking stations, such as the COSMIC Bit Grabber Network [45].

$$\hat{\phi}^R[k] = atan2\left(\frac{\bar{q}[k]}{D[k]}, \frac{\bar{i}[k]}{D[k]}\right) \tag{3.31}$$

Equation (3.31) produces an estimate of the wrapped residual phase, $\hat{\phi}^R[k]$, limited to the range $[-\pi, \pi]$. Computing the residual phase requires maintaining a count, $C[k]$, of the number of accumulated integer cycles over the duration of the occultation measurement, giving an estimate of the "unwrapped" residual phase $\hat{\Phi}^R[k]$.

$$\hat{\Phi}^R[k] = \hat{\phi}^R[k] + 2\pi C[k] \tag{3.32}$$

Following the procedure defined in [39], the change in phase between two consecutive 20 ms samples is monitored.

$$S[k] = \text{atan2}\left(\frac{\bar{q}[k]}{D[k]}, \frac{\bar{i}[k]}{D[k]}\right) - \text{atan2}\left(\frac{\bar{q}[k-1]}{D[k-1]}, \frac{\bar{i}[k-1]}{D[k-1]}\right) \tag{3.33}$$

and if the magnitude of this change exceeds π, a cycle is added or subtracted.

$$C[k] = \begin{cases} C[k-1] + 1 & \text{if } S[k] < -\pi \\ C[k-1] - 1 & \text{if } S[k] > +\pi \\ C[k-1] & \text{, otherwise} \end{cases} \tag{3.34}$$

Figs. 3.3 to 3.5(a) show examples of excess phase profiles extracted from ARO data (details of the experiment are given in section 3.4). Fig. 3.3(a) and Fig. 3.4(a) also show the results for the same occultation recorded on a CL receiver. As Fig. 3.4(a) shows, OL tracking (solid line) produces meaningful results from the signal for at least 3 more minutes beyond the loss of CL tracking (gray dots) due to signal fading in the lower atmosphere. In this example, the refractivity profile can be retrieved down to 2.1 km with OL tracking before the noise dominates the excess phase versus 4 km with CL tracking [24]. This provides a longer set of observations extending into the lower troposphere. The lower plots in Figs. 3.3 to 3.5 show the SNR (to be defined later) and the aircraft heading. Fig. 3.4(b) presents a setting occultation in which the SNR is decreasing with time. On the other hand, Fig. 3.5(b) shows a rising occultation case, in which the SNR is increasing with time and the backward tracking is used. In both cases, the OL tracking is able to extract and unwrap a residual phase profile. Qualitatively, one can see that the loss of information in the OL tracking result is correlated with a decrease in the SNR. A model for this relationship will be developed in the next section.

3.3 Noise and Error Model

A model for the error propagation in the OL tracking is developed for two purposes: First, to relate the SNR to the variance in the residual phase and, second, to use the relationship between the phase variance and the SNR to provide a theoretical basis for setting a threshold beyond which a refractivity profile cannot be reliably recovered. In contrast to CL tracking, in which the receiver indicates a loss of lock at a low SNR value, the OL tracking continues to produce a phase measurement, albeit meaningless, even after the signal has dropped below the noise level and disappeared. The point at which the effect of noise on the phase measurement is so large as to produce an unacceptable bias in the retrieved refractive index sets an effective minimum ray-path altitude through the atmosphere. We simulate the refractivity bias due to the failure of the unwrapping described in section 3.3.2, and set this bias as a criterion indicating the loss of the measurement.

3.3.1 Residual Phase PDF

In this section, we derive a model for the probability density function (PDF) of the residual phase as a function of the SNR, and compare the variance predicted from that model to experimental measurements from rising and setting occultations.

Expressing the model for the post-correlation signal (3.30) in polar form

$$\bar{z}[k] = \hat{w}[k] e^{j\hat{\phi}^R[k]} \tag{3.35}$$

presents the amplitude and phase estimates and their random errors.

$$\hat{w}[k] = w[k] + \varepsilon^r[k], \tag{3.36}$$

$$\hat{\phi}^R[k] = \phi^R[k] + \varepsilon^\phi[k] \tag{3.37}$$

We can assume that the in-phase and quadrature components of the noise in (3.35) are two independent, identically distributed, Gaussian, white noise processes, with variance σ^2.

The joint PDF for $\bar{i}[k]$ and $\bar{q}[k]$, conditioned on the true phase and amplitude can therefore be written as:

$$\psi\left(\bar{i}[k], \bar{q}[k] \mid w[k], \phi^R[k]\right) = \frac{1}{2\pi\sigma^2} \exp\left\{ -\frac{(\bar{i}[k] - w[k]\cos\phi^R[k])^2 + (\bar{q}[k] - w[k]\sin\phi^R[k])^2}{2\sigma^2} \right\} \tag{3.38}$$

Given that $\bar{z}[k]$ and $\bar{z}[j]$ are independent for $k \neq j$, we drop the index in the following derivation to simplify the nomenclature. Unwrapping, however, involves the comparison of subsequent measurements between steps k and $k-1$, so this index will be re-introduced in section 3.3.2 when applying the result from this section.

With a change of variables, the joint density of $\hat{w}$ and $\hat{\phi}^R$ can be derived from the Gaussian density in (3.38)

$$\psi_w\left(\hat{w}, \hat{\phi}^R \mid w, \phi^R\right) = \hat{w}\psi\left(\hat{w}\cos\hat{\phi}^R, \hat{w}\sin\hat{\phi}^R \mid w, \phi^R\right) \tag{3.39}$$

The marginal density for $\hat{\phi}^R$ can then be computed by integrating over $\hat{w}$.

$$\psi\left(\hat{\phi}^R \mid w, \phi^R\right) = \int_0^\infty \psi\left(\hat{w}, \hat{\phi}^R \mid w, \phi^R\right) d\hat{w} \tag{3.40}$$

giving

$$\psi\left(\hat{\phi}^R \mid w, \phi^R\right) = \frac{1}{2\pi}\Pi\left(\frac{\hat{\phi}^R}{2\pi}\right) \times$$
$$\left\{\exp\left(-\frac{\Sigma^2}{2}\right) + \Sigma\sqrt{\frac{\pi}{2}}\cos\left(\hat{\phi}^R - \phi^R\right)\exp\left[-\frac{\Sigma^2}{2}\sin^2\left(\hat{\phi}^R - \phi^R\right)\right]\left[\operatorname{erf}\left(\frac{1}{\sqrt{2}}\cos\left(\hat{\phi}^R - \phi^R\right)\right) + \right.\right. \tag{3.41}$$

where $\Sigma = w/\sigma$ is the SNR of the post-correlation signal at the k^{TH} step [46]. Here $\Pi(x)$ is the unit pulse:

$$\Pi(x) = \begin{cases} 1 & \text{for} \quad |x| < 1/2 \\ 0 & \text{for} \quad |x| > 1/2 \end{cases} \tag{3.42}$$

If no signal is present, $w = 0$ and (3.41) simply reduces to a uniform density for phase:

$$\psi_\phi\left(\hat{\phi}^R[k]\right) = \frac{1}{2\pi}\Pi\left(\frac{\hat{\phi}^R[k]}{2\pi}\right) \tag{3.43}$$

The amplitude $\hat{w}$ can be shown to have a Rician density, which reduces to a Rayleigh density for $w = 0$ [47].

This model was compared to experimental measurements of the phase variance and SNR obtained from four occultations during research flight (RF) #18 (Section 3.4). The phase variance of the piece-wise de-trended signal was computed using a 1 sec sliding time window for the entire duration of an occultation event. The post-correlation signal amplitude, $\hat{w}$, was obtained from the average amplitude of the complex correlation $\hat{w} = \left\langle \sqrt{\bar{i}^2 + \bar{q}^2} \right\rangle$ over each 1 sec sliding window. Noise variance, σ^2, was estimated from the variance of $\bar{i}$ and $\bar{q}$ extracted from a time period of 1 sec following the end of the occultation. σ^2 was assumed to remain constant over the duration of the occultation. On Figs. 3.6 to 3.9, the theoretical phase standard deviation, calculated by integrating (3.41), is shown as the solid lines and the data collected from

RF18 are grey dots. Phase standard deviation was computed from the experimented data,

$$\sigma_\phi = \sqrt{\left\langle (\phi^R - \langle \phi^R \rangle)^2 \right\rangle} \tag{3.44}$$

in which < > indicates a time average over a 1 sec sliding window. At low SNR, the phase variance is very high and the measurements follow a random walk process, whereas when SNR increases, the phase standard deviation in all four cases decreases because there is less uncertainty in the in-phase and quadrature component values. These figures show that the model for phase standard deviation accurately reproduces the statistics of the observed phase.

3.3.2 Threshold Determination

To investigate the hypothesis that unwrapping error will eventually limit the ability of OL tracking to produce an unbiased phase and Doppler frequency observable, we will derive a statistical model for the cumulative unwrapping error by connecting the phase estimate $\hat{\phi}^R[k]$ PDF (3.41) with the unwrapping algorithm (3.33) and (3.34). Assume that two consecutive phase estimates, $\hat{\phi}^R[k-1]$, and $\hat{\phi}^R[k]$, are independent. The joint conditional PDF can then be expressed as:

$$\begin{aligned} &\psi\left(\hat{\phi}^R[k-1], \hat{\phi}^R[k] \mid w[k-1], \phi^R[k-1], w[k], \phi^R[k]\right) = \\ &\quad \psi\left(\hat{\phi}^R[k-1] \mid w[k-1], \phi^R[k-1]\right) \psi\left(\hat{\phi}^R[k] \mid w[k], \phi^R[k]\right) \end{aligned} \tag{3.45}$$

The unwrapping decision (3.34) is based on the difference in consecutive phase measurements. This divides the $(\hat{\phi}^R[k-1], \hat{\phi}^R[k])$ plane into 3 different regions as shown in Fig. 3.10(a). To simulate the true excess phase without noise, we use the Radio Occultation Simulator for Atmospheric Profiling (ROSAP) ray tracing program [48] with the corresponding airborne occultation period and geometry. Fig. 3.10(b) shows the ROSAP excess phase which we utilize as true phase, $\phi^R[k]$ and $\phi^R[k-1]$ in (3.45). An unwrapping error results when the true phase difference lies in one region while the phase difference estimated from the noisy signal lies in another. The probability of an error of m cycles, in unwrapping $\Phi[k]$, is defined as

$$\gamma^m[k] = \Pr\left\{\left(\hat{\phi}^R[k-1], \hat{\phi}^R[k]\right) \in U_m \mid w[k-1], \phi^R[k-1], w[k], \phi^R[k]\right\} \tag{3.46}$$

in which U_m is one of the three regions; $S[k] < \pi$, $S[k] > \pi$, or $-\pi < S[k] < \pi$ described in (3.34). The specific U_m corresponding to the value m will also depend upon the $\phi^R[k]$ and $\phi^R[k-1]$, which are the consecutive true residual phases at time k and $k-1$. The unwrapping error in cycles is in the range $-2 \leq m \leq 2$ for each pair because of the 3 possible unwrapping results (3.34) at any time k and the 3 corresponding "true" unwrapping results defined by $\phi^R[k]$ and $\phi^R[k-1]$. The conditional probability of each of the three regions can be calculated using the joint PDF (3.45):

$$\gamma^m[k] = \iint_{U_m} \psi\left(\hat{\phi}^R[k-1], \hat{\phi}^R[k] \mid w[k-1], \phi^R[k-1], w[k], \phi^R[k]\right) d\hat{\phi}^R[k-1] d\hat{\phi}^R[k] \tag{3.47}$$

Equation (3.46) describes the probability of error as a function of SNR through (3.41), conditioned on the true phase at time step k and $k-1$. The unwrapping error accumulates with subsequent time steps. The accumulated error probability Γ, can be modeled as non-homogeneous Markov chain,

$$\begin{gathered}\Gamma^n[k] = \sum_j \Gamma^j[k-1]\gamma^{n-j}[k] \\ j = \left[max\left(-2k, n-2\right),\ min\left(n+2, 2k\right)\right],\ n = [-2k,\ 2k]\end{gathered} \tag{3.48}$$

where n is the number of accumulated error cycles and $\Gamma^n[k]$ is the probability of having accumulated n error cycles at the k-th time step due to the noise. $\Gamma^{n-j}[k]$ is the probability of accumulating $n-j$ cycle errors at step k, computed using (3.46). With the probability distribution model of total error cycles at each time step, which can be characterized by average and range of unwrapping error, we can compute the error in excess phase.

From this, we can assess the effect on retrieved refractivity. Performing this calculation requires the joint distribution of the "true" phase, $\phi^R[k]$, $\phi^R[k-1]$. We use the ROSAP ray tracing program to simulate the excess phase pair $(\phi^R[k-1], \phi^R[k])$ during a typical airborne occultation period. A spherical Earth model is used with a radius of 6370 km. In our simulation we assume constant aircraft altitude at 14 km, and an exponential atmospheric refractivity profile which has 55.2 N-units at 14 km height. We also maintain a constant SNR throughout the occultation event. The result of Γ^n at the last time step, computed with different SNR values is plotted versus unwrapping error (numbers of cycles) in Fig. 3.11.

As the result shows, when the SNR level is low, the variance of the error cycle distribution tends to be larger (wider Gaussian in Fig. 3.11), which is expected from the derived excess phase distribution. Noticeably, there also exists a bias in the error cycle distribution which will increase as SNR decreases. This biases the excess phase of the occultation signal, which exhibits a monotonic increase or decrease with time for setting or rising occultations, respectively. The relationship between the SNR and unwrapping bias is shown in Fig. 3.12 and Fig. 3.13. For a rising occultation, in which excess phase is monotonically decreasing, the bias is also negative, since the residual phase is accumulated backwards. We verified our noise model by comparing the bias calculated by the model in (3.48) (dashed line) with the one from a simulation implemented by adding the noise to the ROSAP wrapped phase (solid line). In this case, both the excess phase bias magnitude and the variance increase as the SNR decreases. The bias in the excess phase caused by low signal strength also biases the retrieval of refractivity and affects it more severely at the end of the occultation. Our objective is to use these findings to define a threshold to indicate when the RO data quality is limited by the unwrapping bias and to mitigate the possibility of producing biased retrievals.

To determine this threshold, we use the actual SNR calculated from the signal amplitude of ARO data, along with the noise-free excess phase from a ROSAP simulation using the geometry of the corresponding case. By subtracting the modeled unwrapping bias from ROSAP ray tracing excess phase $\phi^R[k]$, we simulate the excess phase of a received signal, which contains an error due to the bias caused by noise. The refractivity retrieved by the inverse Abel-transform of the noise-affected excess phase shows how low SNR observations generate a bias in refractivity retrieval. Fig. 3.14 shows fractional refractivity difference results between noisy and noise-free signal using data from satellites PRN12 (RF18) and PRN17 (RF19) respectively. Fig. 3.14 shows a bias for the simulated noisy profile retrievals near the surface. This may be due to the monotonic nature of the residual phase profile, relative to the geometric Doppler. Sokolovskiy et al. (2009) [38] argued that a Doppler model that includes an atmospheric component may reduce this bias, therefore this is a possible area for investigation in future work. This bias should then be considered a worst case estimate. Murphy et al. (2014) [24], showed that over the height range where the airborne geometric optics retrieval method is valid, the retrieval accuracy is 2% in refractivity, the limitation being primarily strong horizontal variations in moisture and refractivity structure in the lower troposphere. Therefore, assuming 2% target accuracy for a threshold, we can calculate the lowest height where any bias associated with discriminating a weak signal is below that threshold. For the case of PRN12, although OL tracking made it possible to retrieve excess phase observations down to the altitude of 2.1 km, the biases introduced by unwrapping error in the presence of noise exceeds 2% below 5.3 km. In a second case, PRN17, the OL tracking excess phase is retrieved down to 2.4 km, and the 2% refractivity error threshold is at 3.8 km. By following the same procedure with each individual case, we can theoretically calculate the threshold that represents the lowest height allowing discrimination of a weak signal from noise.

3.4 Experiment

3.4.1 GISMOS

The GNSS Instrument System for Multistatic and Occultation Sensing (GISMOS) was designed to use occulted and reflected GPS signals on the NSF/NCAR High-performance Instrumented Airborne Platform for Environmental Research (HIAPER) aircraft. The main units of GISMOS are a Symmetricom ExacTime600^{TM} timing receiver, an Applanix POS AV^{TM} GPS/INS navigation system, four Trimble NetRS^{TM} survey-quality receivers and a GNSS Recording System (GRS) built at the Johns Hopkins University Applied Physics Laboratory (JHU/APL) [49]. The Symmetricom ExacTime 600 GPS timing receiver uses an oven-controlled crystal oscillator (OCXO) and provides a 10 MHz reference frequency to the GRS, POS AV and NetRS receivers reducing the relative clock drift between them. The Applanix POS AV GPS/INS provides accurate position and velocity of the aircraft using dual frequency GPS measurements with 5 mm/s velocity precision to minimize Doppler noise which contributes to refractivity errors [41].

Seven antennas were mounted on the exterior of the airplane. One is placed on top of the aircraft and is used for positioning and velocity measurements. Two high-gain and wide-view avionics antennas were mounted on each side of the aircraft, as well as two high-gain, narrow vertical and wide horizontal gain antennas specially designed for capturing RO signals. Right-Hand and Left-Hand Circularly Polarized (RHCP and LHCP) antennas were mounted on the bottom of the fuselage for measuring ocean surface roughness and soil moisture from the reflected GPS signals.

The GRS samples the wide-band GPS signals at 10 MHz on both L1 and L2 frequencies, and writes to a disk array with 1-bit quantization in both I and Q components simultaneously on three channels. For occultation measurements, one channel is connected to the top antenna and the other two are connected to high-gain side-looking antennas (starboard and port).

GISMOS also includes survey-quality Trimble NetRS receivers. These receivers track civilian signals on L1 and L2, and codeless military signals on L2 using conventional CL tracking methods. For occultation measurements, these receivers record carrier phase and Doppler frequency from all four high-gain and wide-view side-looking antennas. We use the NetRS measurements as a reference for OL tracking to verify that the same phase measurements over the overlap time periods are produced (the gray lines in Fig. 3.3(a) and Fig. 3.4(a)). The improvement over the conventional NetRS observation from OL tracking in terms of the duration is shown and quantified in terms of the increased depth of the ray path in Section 3.2.5.

3.4.2 Research Flights

We analyze two data sets recorded during the Pre-Depression Investigation of Cloud-systems in the Tropics (PREDICT) campaign which was planned to observe developing tropical storms in the Atlantic [24]. The first data set was recorded on 13 September 2010 and the second data set was recorded on 14 September 2010, day 256 and 257 respectively. The objective of these two flights was to collect GPS RO and droponde measurements for inter-comparison, and investigate the moisture development during the genesis phase of hurricane Karl. A lawnmower pattern (Fig. 3.15) was flown to attempt to regularly sample the development region, modified where necessary (as in Fig. 3.15(a)) to avoid flying through dangerous deep convection locations. The red lines in Fig. 3.15 show the occultation tangent point paths and the stars are the tangent point locations of nearby COSMIC spaceborne measurements.

3.5 Results

3.5.1 Observation comparisons with atmospheric soundings

In order to evaluate the performance of the ARO system, measurements from this system were compared to other independent observations collected in the vicinity of the ARO profile. We compare the OL tracking excess Doppler profile for PRN06 rising satellite with the excess Doppler simulated with ROSAP for the same occultation geometry for a nearby radiosonde at Willemstad, Curacao (TNCC), where a sounding was available at 12:56 UTC. We also simulated excess Doppler profiles using the model profiles from the European Centre for Medium-range Weather Forecasts Interim Re-Analysis (ERA-interim) [50] extracted at the closest grid point to the occultation tangent point location.

There is a receiver clock error present in the occulting satellite signal. To eliminate this error, we use a single difference of the excess Doppler profiles from the occulting and a high elevation satellite recorded on the same receiver. Using a high elevation satellite excess Doppler profile ensures that we are not removing any atmospheric effect from the time series, but rather a common clock error. The comparison of the difference of PRN06 and a high elevation PRN31 satellite excess doppler profiles with the radiosonde and ERA-interim simulations are shown in Fig. 3.16(a) and Fig. 3.16(b). These figures demonstrate that the excess Doppler obtained with the OL tracking is consistent with the ERA-interim as well as the radiosonde simulations. The largest differences occur between 10.4 to 10.5 hours that show up as large spikes in the observed excess Doppler. By comparing these results with Fig. 3.3, it is evident that the large variations in the excess Doppler coincide with the time of SNR variations due to the change in the aircraft heading.

3.5.2 SNR Model

We also compare the SNR from orbital RO observations made in close proximity to our airborne experiments and use a link budget to provide an explanation for the observed differences in the SNR. In order to compare the SNR in the airborne and spaceborne RO observations, the two measurements must be transformed to common units. The COSMIC system documentation provided by the COSMIC Data Analysis and Archive Center (CDAAC) [11] states that the magnitude of the SNR SNR_v in volts from the Integrated GPS Occultation Receiver (IGOR) is proportional to the received signal amplitude. Since the sum of the noise amplitude in one second is modeled as a random walk, the noise magnitude accumulated in one second will grow with the rate of the square root of the sampling rate. Therefore, the SNR_v in an interval $T_1 = 1$ sec can be written as:

$$SNR_v = \frac{T_1 f^B \cdot A_s}{\sqrt{T_1 f^S} \cdot A_n} \tag{3.49}$$

where A_s is the measured signal amplitude with a rate f^B, and A_n is the single sample noise amplitude with a sample rate of f^S. The frequency f^B is $50Hz$ since the measured signal amplitude $A_s = \sqrt{\bar{i}[k]^2 + \bar{q}[k]^2}$ is summed every 20 ms as stated in (3.29). The sample rate f^S is $20.456MHz$ for COSMIC. The constant $A_n = 0.2905$ is the average noise amplitude in a single channel of the COSMIC system so that SNR_v is proportional to the received signal strength as stated in [11]. The spaceborne SNR_v can be converted to carrier-to-noise ratio (C/No), interpreted as the SNR in power units within a 1 Hz bandwidth, more commonly used in GNSS navigation receivers [51] [52] using

$$\left({}^{C}/_{N_0}\right)_{COSMIC} = 20log_{10}\left(\frac{SNR_v}{\sqrt{2}}\right) \tag{3.50}$$

For the airborne case we calculate the signal amplitude A_s explicitly for every sample with the rate of f^B. We set airborne A_n as the average of the last 500 samples in a setting case, or the first 500 samples in a rising case, well outside the time period of interest. Since both A_s and A_n are calculated at a rate of f^B, the comparable carrier-to-noise ratio of the airborne system can be calculated directly as:

$$\left({}^{C}/_{N_0}\right)_{Air} = 10log_{10}\left(f^B\left(\frac{A_s}{A_n}\right)^2\right) \tag{3.51}$$

Equation (3.51) does not contain the term $\sqrt{2}$ because we calculate A_n with a complex measurement, while a single-channel constant is used in the COSMIC system.

	RF18	
	COSMIC(PRN12)	Airborne(PRN12)
EIRP (Eqv. isotropically radiated power)	26.4 dBW	26.4 dBW
Range	26000 km	24700 km
Path loss	-159.3 dB	-158.84 dB
Atmospheric loss for vertical path	-0.5 dB	-0.5 dB
Received Power Density	-133.4 dBW/m^2	-132.94 dBW/m^2
Effective area of antenna	-25.4 dBm^2	-25.4 dBm^2
Boresight antenna gain	10 $dBic$	9.4 $dBic$
Pattern loss (Directivity)	0 dB	-16 dB
Received Power	-148.8 dBW	-164.9 dBW

Table 3.1. SNR comparison between COSMIC and airborne occultation signals for nearby locations at 14.5° latitude for RF18 on 13 September 2010

The signal strength model is constructed based on a link budget for the GPS satellite. The link budget includes satellite antenna transmission power, path loss, GPS satellite antenna gain at low elevation, and atmospheric loss. At the receiver, it includes receiving antenna effective area and receiving antenna gain in the line of sight direction. In this link budget, a few factors account for most of the observed differences between the spaceborne and airborne case (Table 3.1 and Table 3.2).

First of all, the range between the GPS satellite and the receiver is different in these two cases. The signal to the airborne receiver follows a shorter path (normally the difference is about 700 km) which should result in 0.6 dB increase due to the lower space loss. The COSMIC and GISMOS antennas are also quite different. In both systems the antennas designed for occultation are not omnidirectional. Therefore, the antenna directivity, the ratio of power density in the received direction with that in

	RF19	
	COSMIC(PRN11)	Airborne(PRN17)
EIRP (Equivalent isotropically radiated power)	26.4 dBW	26.4 dBW
Range	26000 km	24550 km
Path loss	-159.3 dB	-158.79 dB
Atmospheric loss for vertical path	-0.5 dB	-0.5 dB
Received Power Density	-133.4 dBW/m^2	-132.89 dBW/m^2
Effective area of antenna	-25.4 dBm^2	-25.4 dBm^2
Boresight antenna gain	10 $dBic$	9.4 $dBic$
Pattern loss (Directivity)	0 dB	-8 dB
Received Power	-148.8 dBW	-156.9 dBW

Table 3.2. SNR comparison between COSMIC and airborne occultation signals for nearby locations at 19° latitude for RF19 on 14 September 2010

the direction of strongest emission, needs to be considered for the specific observation geometry in both systems. The COSMIC and GISMOS antenna specifications [53] were used for the gain pattern calculation and were included in the above link budgets. The antenna gain pattern for GISMOS is shown in Fig. 3.17.

The combination of geometry data with the antenna orientation and gain patterns for COSMIC and GISMOS can provide an accurate estimate of the receiving antenna gain at each time step, as shown in Fig. 3.18. The effects of local multipath or obstruction are ignored. In these two cases the antenna directivity value is -16dB in the beginning and -8dB in the end for RF18 PRN12 (setting) and RF19 PRN17 (rising) satellites respectively. These two occultations were selected because of their location nearby the only available COSMIC observations. With its higher gain antenna and boresight observation geometry COSMIC retrievals are more accurate below 5 km. However, many more ARO occultations were observed. For these two flights, excess phase was retrieved below 2 km for 11 of 28 occultations and below 4 km for 24 of 28 [24] compared to 3 occultations for CL tracking. Depending on the orientation relative to boresight for each occultation, the bias threshold differs. The geometry for the airborne system was computed from the aircraft GPS/INS and from the IGS orbit data for the GPS satellites as described in Section 3.2.2. For the COSMIC system the CDAAC Precise Orbit Determination (POD) product was used. The GISMOS system was calculated to have a lower total SNR than nearby COSMIC measurements sampling a similar atmospheric path, primarily due to the lower antenna gain.

3.5.3 COSMIC and airborne comparison

We show the result of calibrated SNR calculations from both systems to discuss the cause of the SNR level differences. The SNR of the GISMOS RO measurements are compared to those from COSMIC obtained for two occultations in close proximity as shown by the tangent point locations in Fig. 3.15. Using the calibration values described in section 3.5.2, the comparable C/N_0 of both systems are shown in Fig. 3.19.

The time axis is not in the same scale for both platforms, because the duration of a satellite occultation is approximately 1 minute, whereas an airborne occultation extends on the order of 10 minutes. The two data sets are plotted together simply for comparison of the SNR levels. The light grey dots show the airborne data and the dark grey dots show the corresponding COSMIC data. There is a large difference in the SNR between these two systems prior to occultation when the signals are strong. We focus here on explaining the signal strength difference during this higher elevation angle period. The differences in signal strength between COSMIC and GISMOS are 14 dB and 9 dB for RF18 PRN12 and RF19 PRN17, respectively. We apply the link budget analysis from Section 3.5.2, with a simulation of the satellite and airborne ranges, the satellite to receiver geometry, and associated antenna gain variation (Fig. 3.18) to calculate the signal strength loss and provide this in Table 3.1.

The antenna directivity to PRN12 (RF18) is -16 dB, since the signal direction is close to the null of the azimuth gain pattern, and the boresight gain of airborne antenna is 9.4 dBic. The simulated range difference between airborne and spaceborne RO accounts for about 0.5 dB. Compared to the COSMIC occultation antenna gain which is about 10 dBic, the simulations predicted a net difference in SNR of about -16.1 dB in Table 3.1, close to the 14dB difference observed in the figure, thus giving confidence that the noise model and the signal processing strength are properly calibrated. By applying the same analysis to the PRN17 occultation, the antenna gain pattern accounts for about -8 dB and the total signal strength should be -8.1 dB compared to COSMIC. The predicted difference of -8.1 dB closely matches our observed difference of -9dB. With this analysis it is clear that the most important factor affecting the SNR is the antenna gain pattern. The possible occultation directions span the range from +/- 180 compared to +/- 125 degrees for the spaceborne platform. To improve the performance, a future ARO mission could use an antenna with a wider beam in azimuth, at the expense of a narrower beam in elevation, or a more sophisticated electronically steerable antenna incorporating GNSS technology developed for other applications [54]. Predicted satellite positions could also be considered in flight mission planning to orient the main beam of the antenna in the direction of the occultation ray path, when practical.

3.6 Couclusions

The airborne GPS RO technique has the potential to sample localized transient events with a higher regional measurement density than what is possible with spaceborne GPS RO, and thus could become a valuable remote sensing technique for the atmospheric science community. This paper has presented the design of an airborne OL tracking software receiver for post-processing IF sampled data in both forward and backward directions in time, for setting and rising occultations, respectively. With this implementation, ARO can serve localized GPS-RO campaigns and supplement spaceborne measurements with on-demand atmospheric profiling in desired areas of transient events, such as tropical storms. An error model relating phase variance to post-correlation SNR has been developed and used to derive a model for the cumulative effect of phase unwrapping error. We propose a new theoretical approach to assessing the threshold for inversion of RO profiles, based upon the net unwrapping bias. The longer duration of ARO profiles (10 minutes vs. 1 minute for satellite) results in a larger accumulation of unwrapping error. The antenna design was found to be a limiting feature of the GISMOS implementation, producing measurements with SNR about 9-14 dB below COSMIC profiles collected in the same area. Whereas airborne and satellite antennas have similar boresight gain, an aircraft's flight path and attitude are not fixed to a specific geometry, as an orbiting satellite would be. Nonetheless, the results from these measurements agreed well with the theoretical models derived in this paper. An antenna design with a wider azimuthal beam width, at the expense of a narrower beam width in the vertical direction or electronic beam-steering, would improve the performance of ARO retrievals, including the ability to extract useful measurements in the lowest part of the troposphere. Consideration of the antenna beam orientation in the mission planning when practical, could also improve the likelihood of high-SNR observations. In addition to lower antenna gain, the combination of multipath [55] and reflection signal interference at lower altitude may cause fluctuation in SNR that also contribute to the negative bias in retrieval results, which can be investigated in future studies.

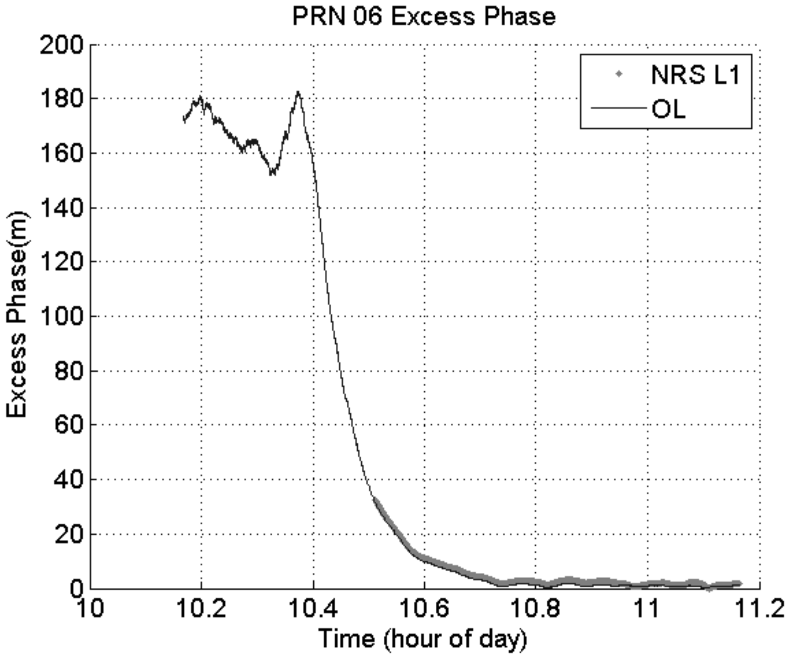

(a)

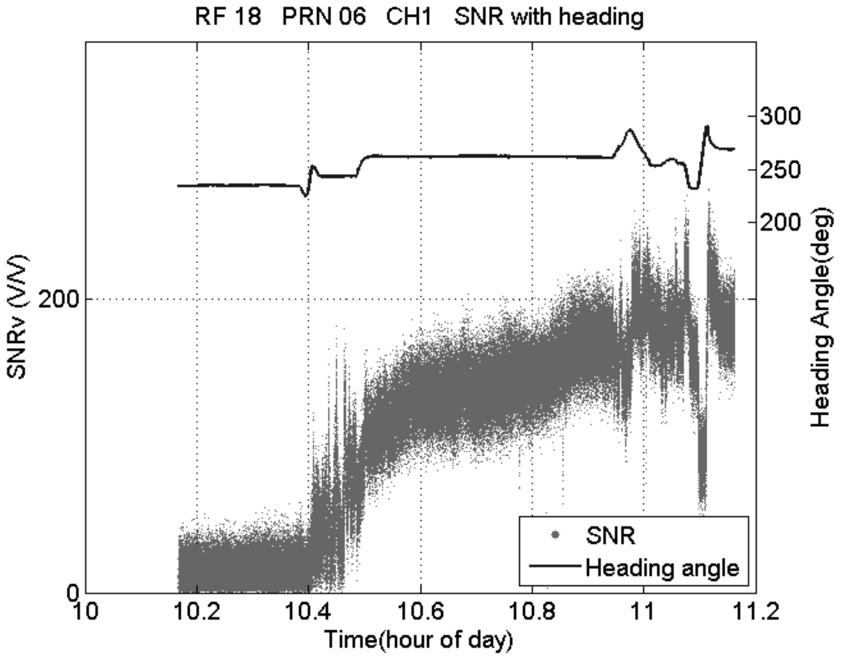

(b)

Figure 3.3. (a) Excess phase for PRN06 recorded on the top antenna with a conventional geodetic receiver (NRS L1: gray dots) and from the OL tracking data (black line). (b) SNR for rising satellite PRN06 recorded on the top antenna (CH1) during RF18 on 13 September 2010 (gray dots). The heading of the aircraft is shown with black line.

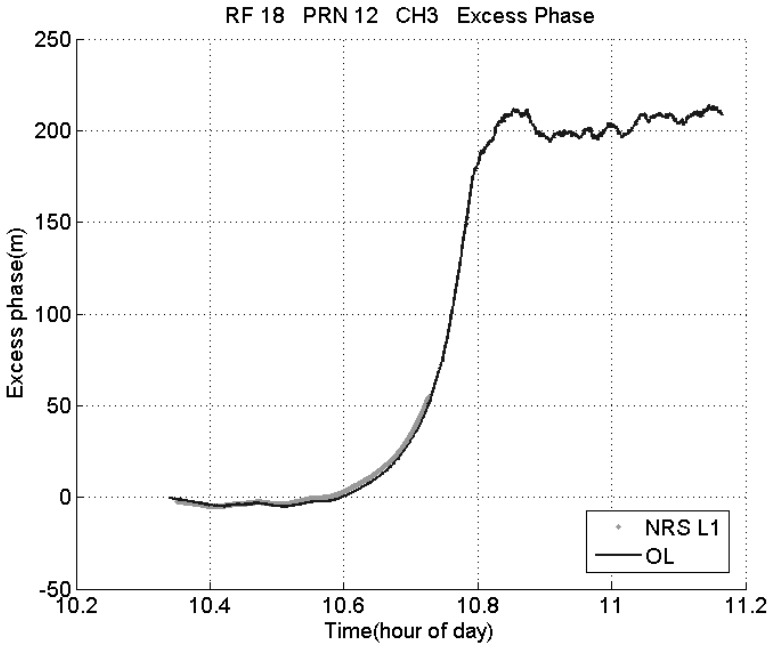

(a)

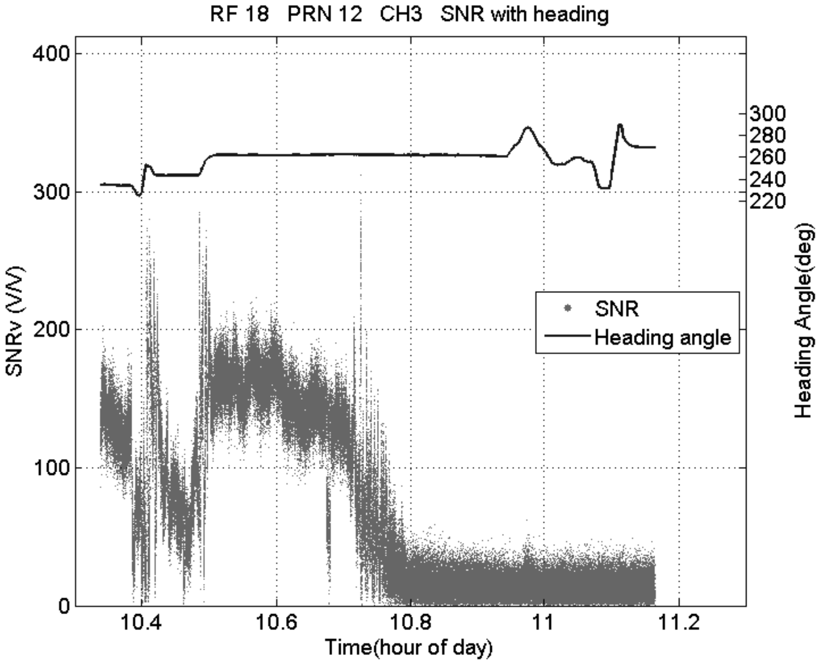

(b)

Figure 3.4. (a) excess phase for PRN12 recorded on the starboard antenna for the open loop tracking data (solid line) and closed loop data (gray dot). (b) SNR for airborne occultation of setting satellite PRN12 recorded on the starboard antenna (CH3) during RF18 on 13 September 2010, and heading of the aircraft.

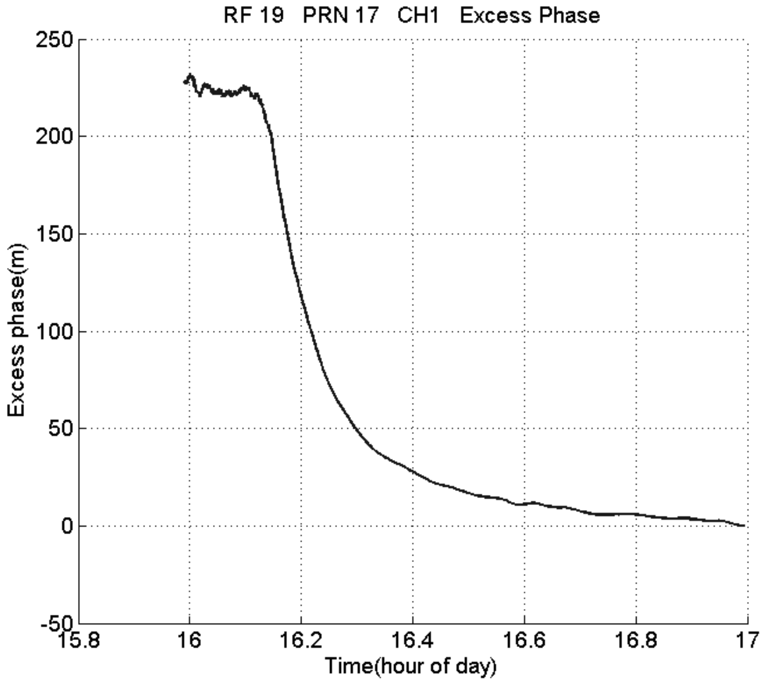

(a)

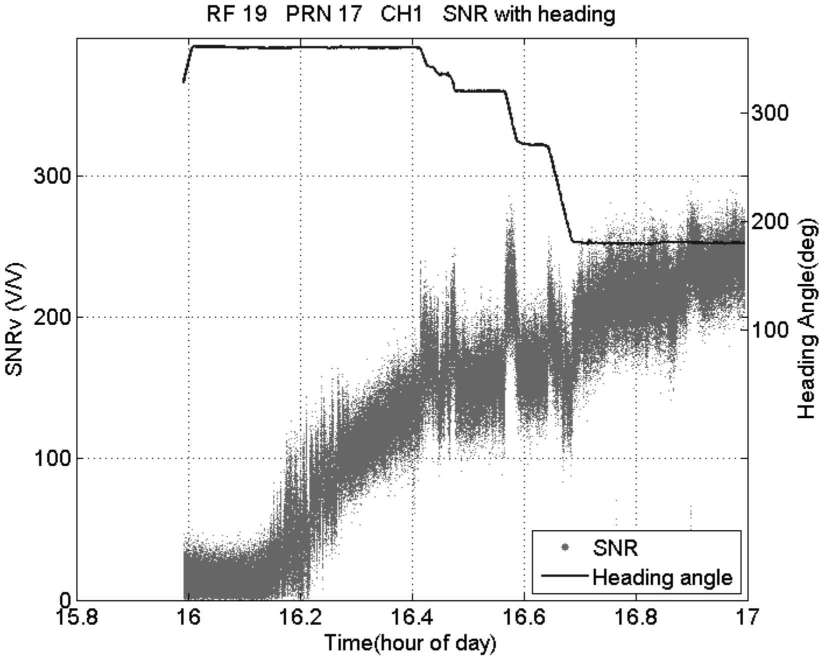

(b)

Figure 3.5. (a) excess phase for PRN17 recorded on the top antenna for the open loop tracking data. (b) SNR for airborne occultation of rising satellite PRN17 recorded on the top antenna (CH1) during RF19 on 14 September 2010, and heading of the aircraft.

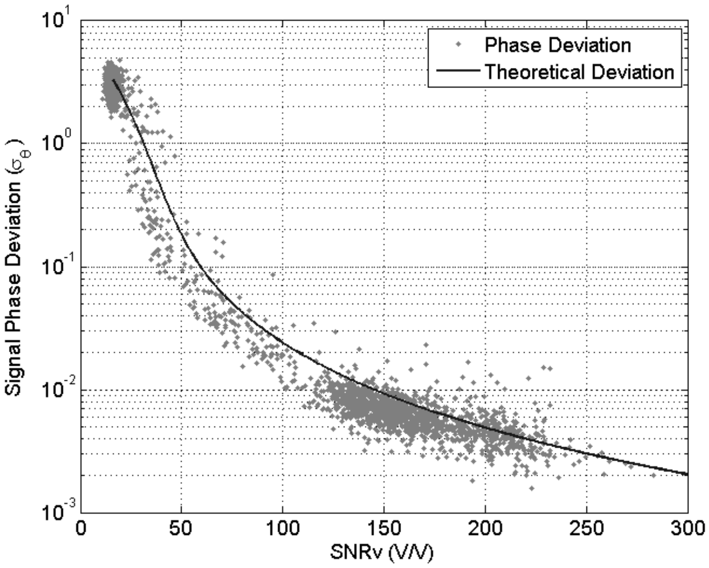

Figure 3.6. Theoretical model of phase standard deviation as a function of SNR from (3.41) (black line), and residual phase standard deviation of the observed signal (detrended over 1 second intervals) as a function of observed SNRv (dots) for PRN12 setting occultation recorded on CH1 top antenna during RF18.

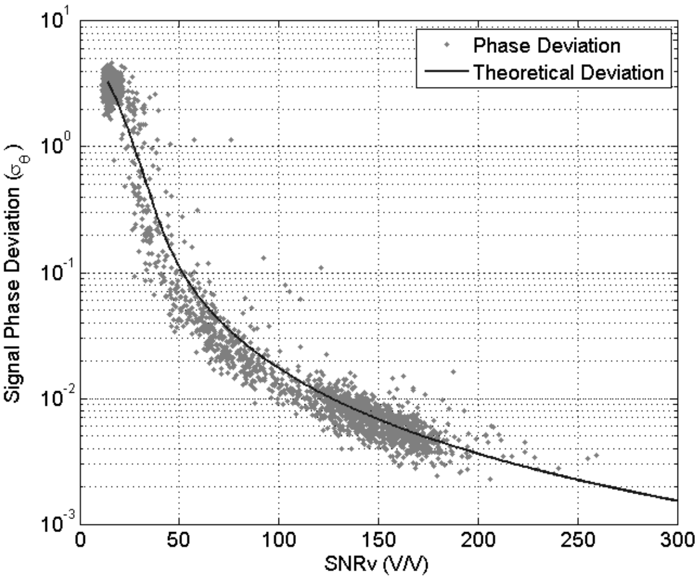

Figure 3.7. RF18 PRN12 CH3

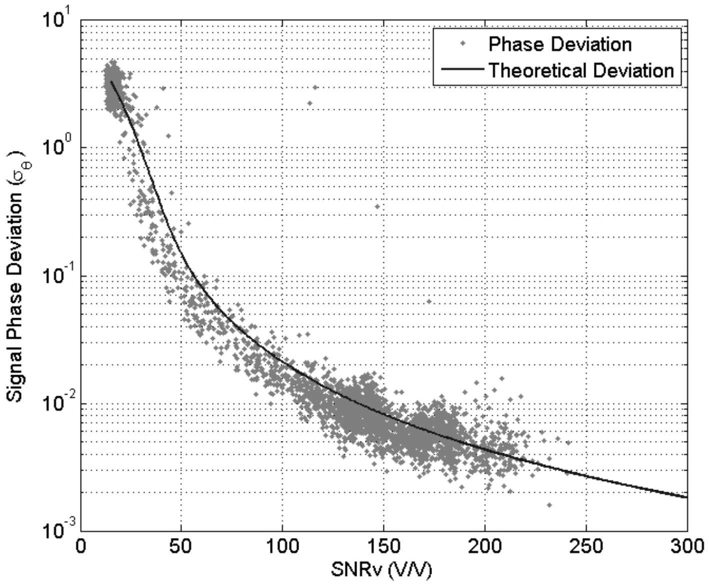

Figure 3.8. RF18 PRN06 CH1

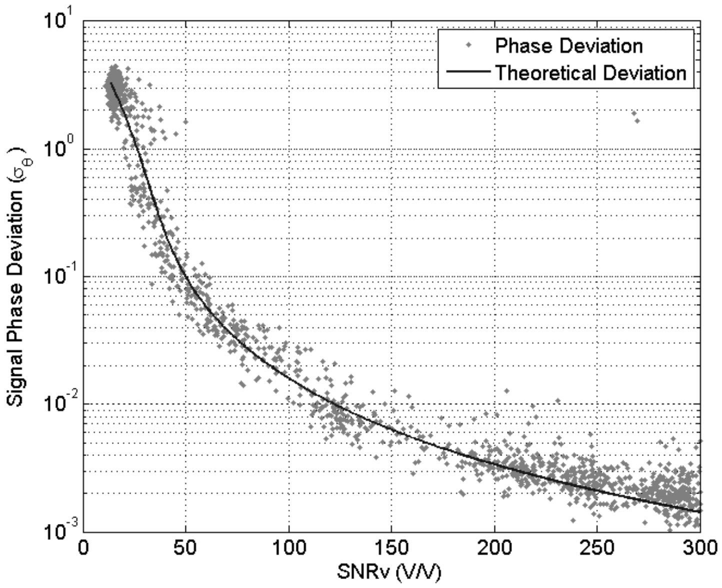

Figure 3.9. RF18 PRN06 CH3

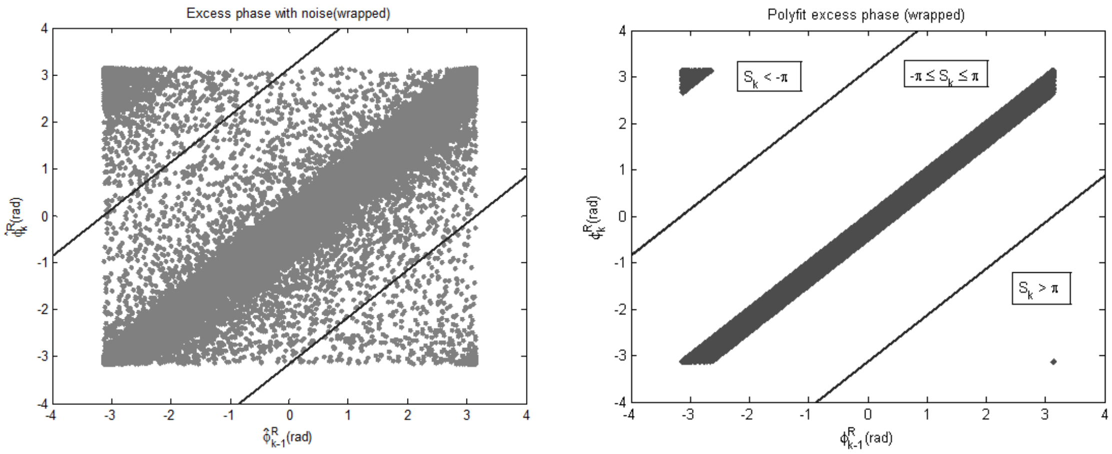

(a) (b)

Figure 3.10. (a) The distribution of $\hat{\phi}^R[k]$ and $\hat{\phi}^R[k-1]$ from observed airborne data. The solid line is the boundary of unwrapping algorithm. The noisy data will increase the failure rate of unwrapping. (b) The distribution of $\phi^R[k]$ and $\phi^R[k-1]$ from the polynomial fitting of the observed airborne data, which can be regard as the noise free excess phase.

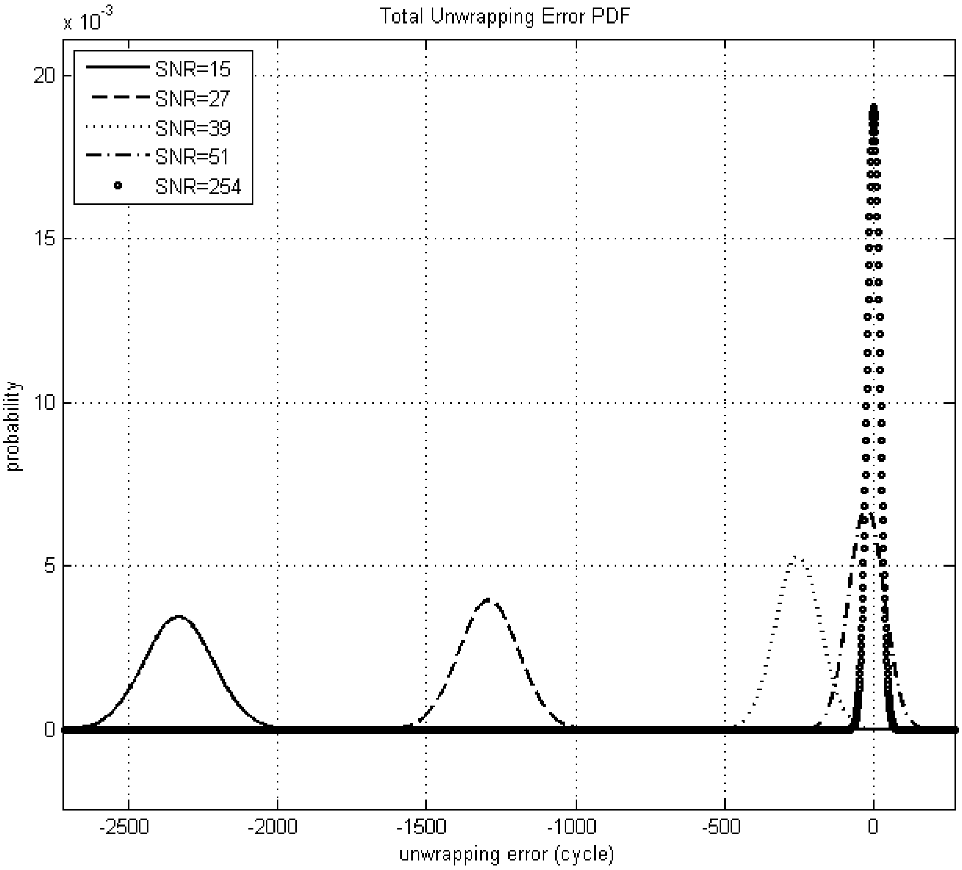

Figure 3.11. The probability density of the number of unwrapping error cycles. The variance increases as SNR decreases. When the SNR level is lower than 51 V/V the average error will have a negative bias due to the monotonically increasing excess phase in the occultation signal. The bias will also increase with decreased SNR.

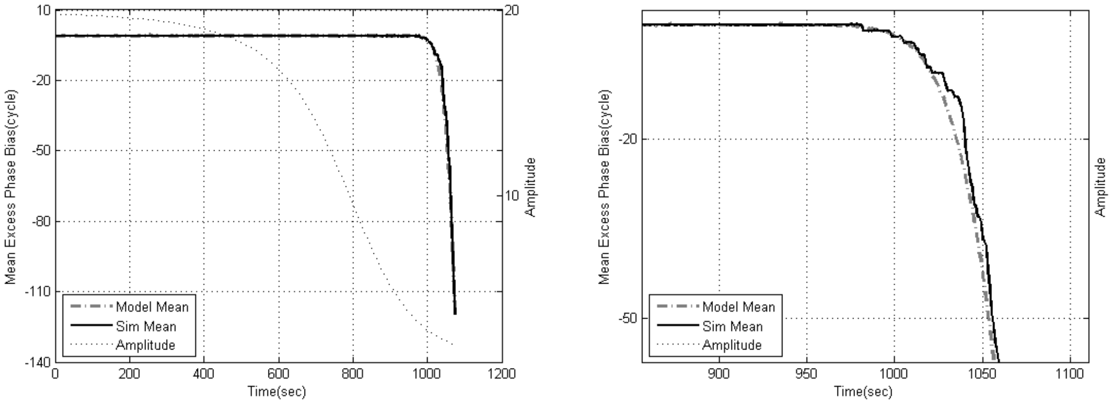

(a) Signal amplitude and excess phase distribution average

(b) Signal amplitude and excess phase distribution average(Zoom in)

Figure 3.12. The relationship between signal amplitude and excess phase distribution for a setting case (forward tracking). The bias calculated by the model (3.48) is shown in dashed line and the bias simulated with the noisy ROSAP wrapped phase is shown in solid line. The model is verified with the resemblance of the two curves.

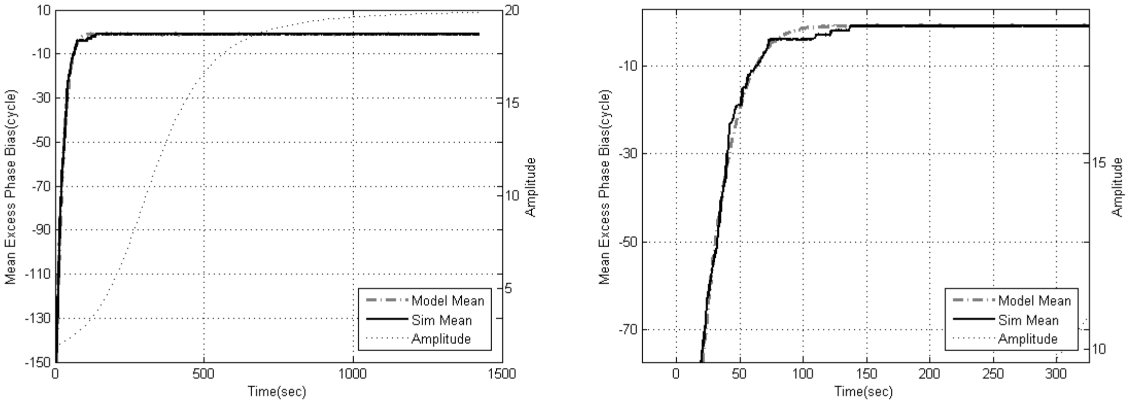

(a) Signal amplitude and excess phase distribution average

(b) Signal amplitude and excess phase distribution average(Zoom in)

Figure 3.13. The relationship between signal strength and excess phase distribution for a rising case (backward tracking). The bias calculated by the model (3.48) is shown in dashed line and the bias simulated with the noisy ROSAP wrapped phase is shown in solid line.

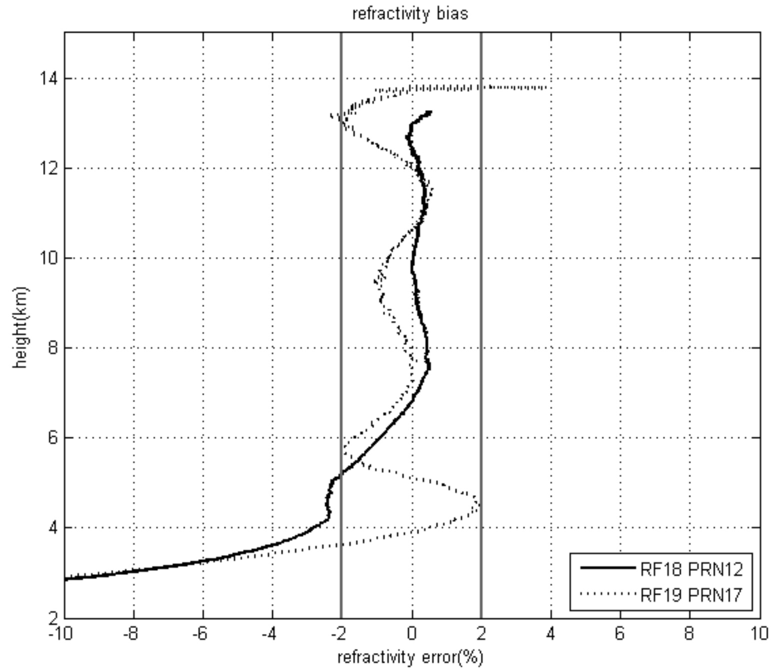

Figure 3.14. The refractivity fractional error with respect to height for RF18 PRN12 (solid line) and RF19 PRN17 (dotted line). A retrieval bias of 2% (gray line) and its corresponding heights of 5.1 km and 3.8 km are chosen as the thresholds for the tracking process.

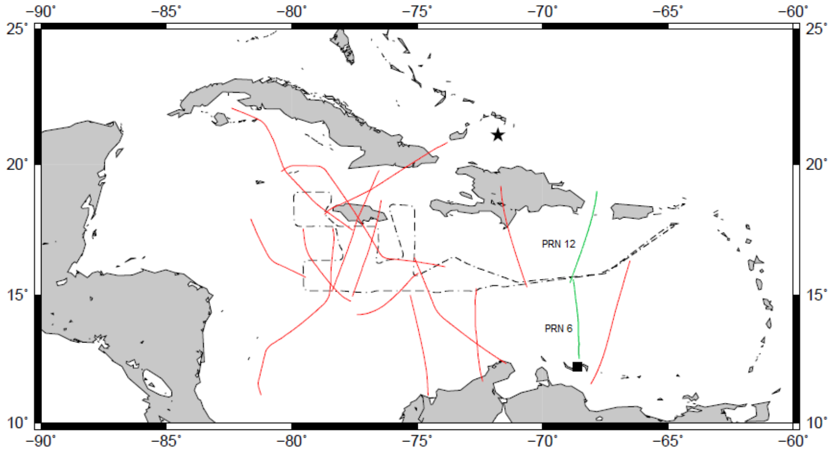

(a) RF18

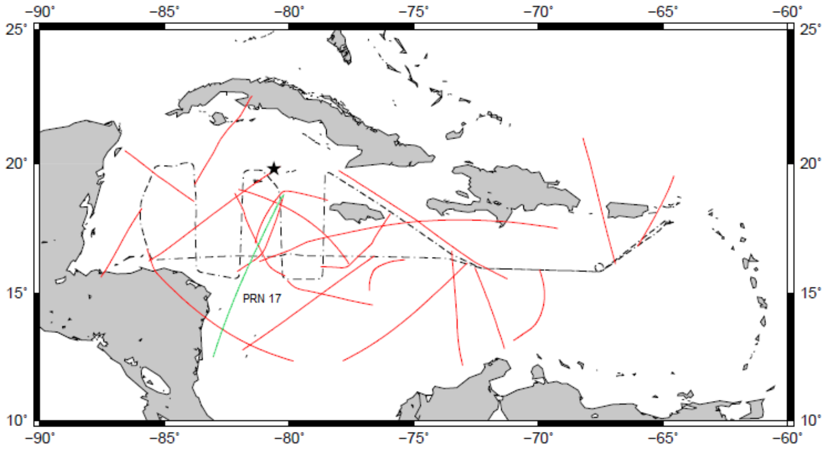

(b) RF19

Figure 3.15. The flight paths (black dash lines) during the PREDICT campaign on 13 September 2010 (RF18) (panel (a)) and 14 September 2010 (RF19) (panel (b)). Red lines show the tangent point locations for each setting and rising satellite occultation during the flight, while green lines show the occultation events examined in detail (PRN6 and PRN12 for RF18, and PRN17 for RF19). The stars show the tangent point location of a collocated spaceborne RO. The square denotes the location of the radiosonde profile from TNCC station.

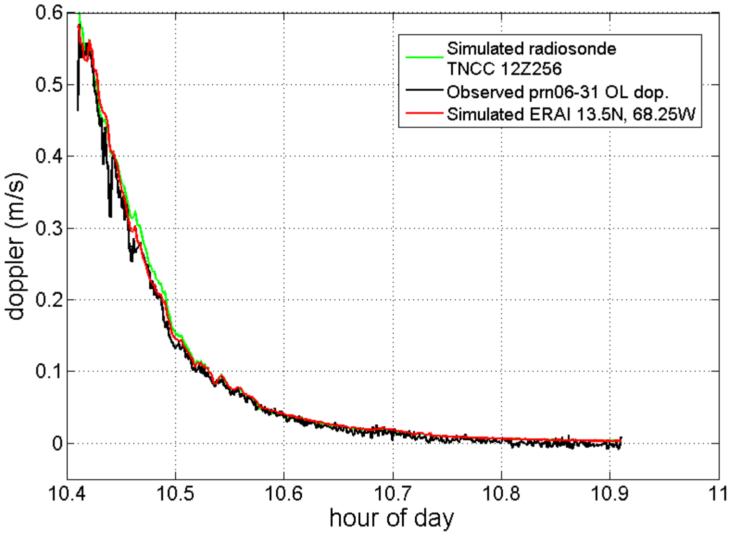

(a)

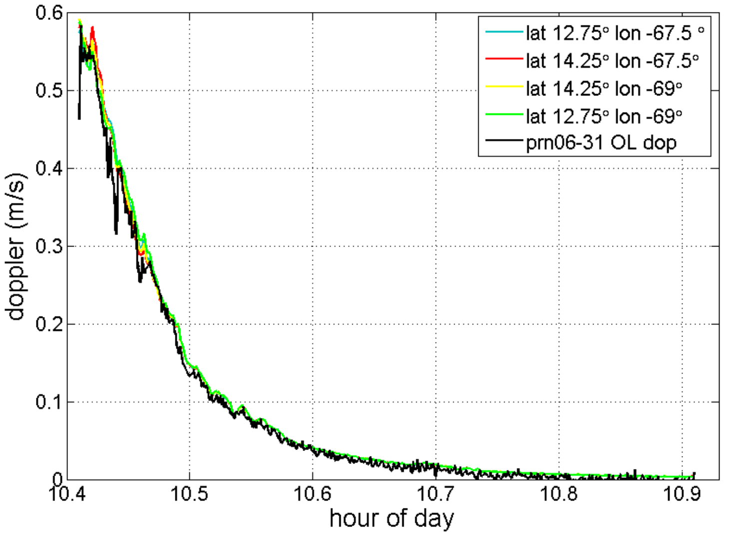

(b)

Figure 3.16. (a) Observed OL tracking excess Doppler for PRN6 on 13 September 2010 (RF18) compared with the simulated excess Doppler for propagation through the atmosphere described by a nearby radiosonde profile TNCC at 12:56 UTC and by the ERA-interim model profile at the location 13.5N 68.25W. (b) Observed excess Doppler compared to the ERA-interim model refractivity at the four closest grid points, illustrating the range of atmospheric variation.

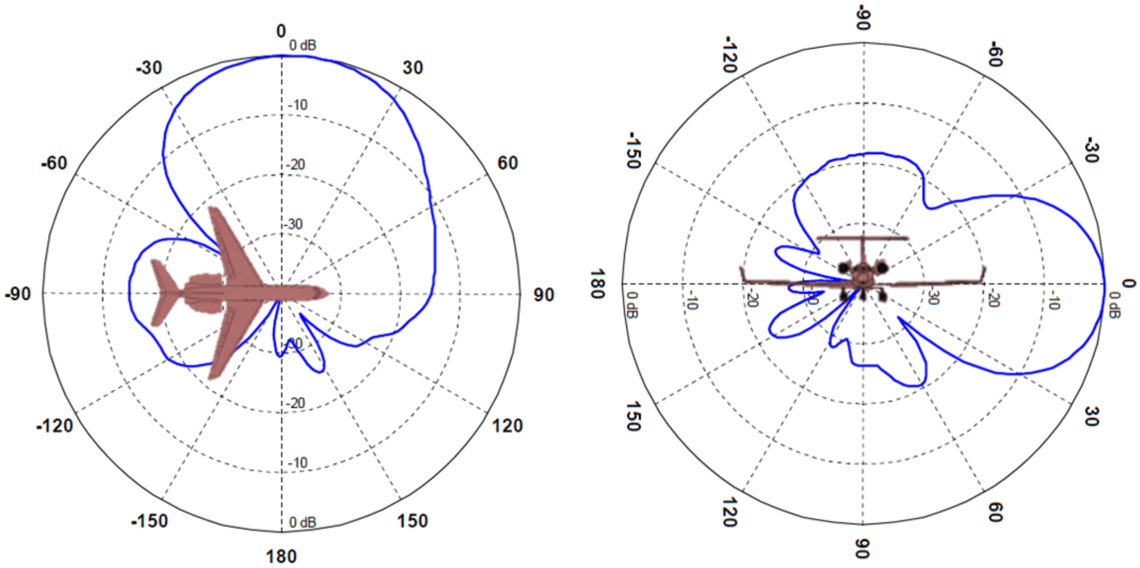

(a) (b)

Figure 3.17. Port antenna (a) azimuth and (b) elevation directivity. The azimuth and elevation in this figure are defined in the antenna body frame. 0° in both azimuth and elevation are oriented toward the horizon, 90 degrees in azimuth points forward and 90° in elevation points at zenith. A null exists at $-60°$in the antenna azimuth. The antenna gain is calculated as the sum of boresight gain (9.4 dBic) and pattern loss (directivity).

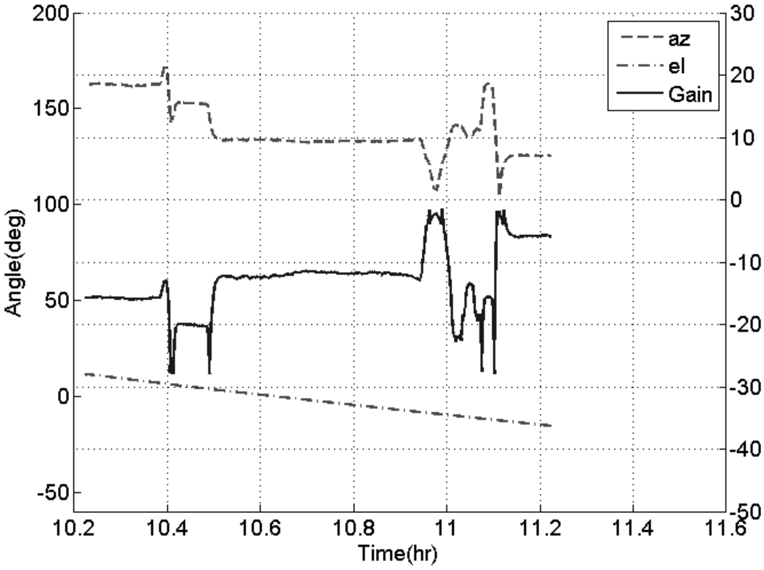

(a)

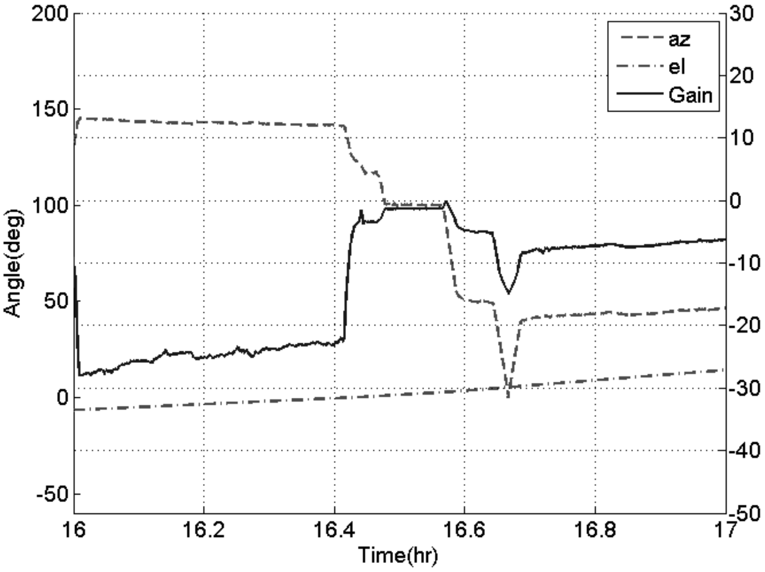

(b)

Figure 3.18. (a) Azimuth with respect to side-looking direction (dashed) and elevation angle (dot-dashed) for line-of-sight from the airborne antenna to the satellite for setting occultation of PRN12 on the starboard antenna (CH3) during RF18. The simulated variation of antenna gain for the side-looking antenna (black) is shown on the right axis. (b) Azimuth, elevation angle, and gain for rising occultation of PRN 17 on the starboard antenna (CH3) during RF19.

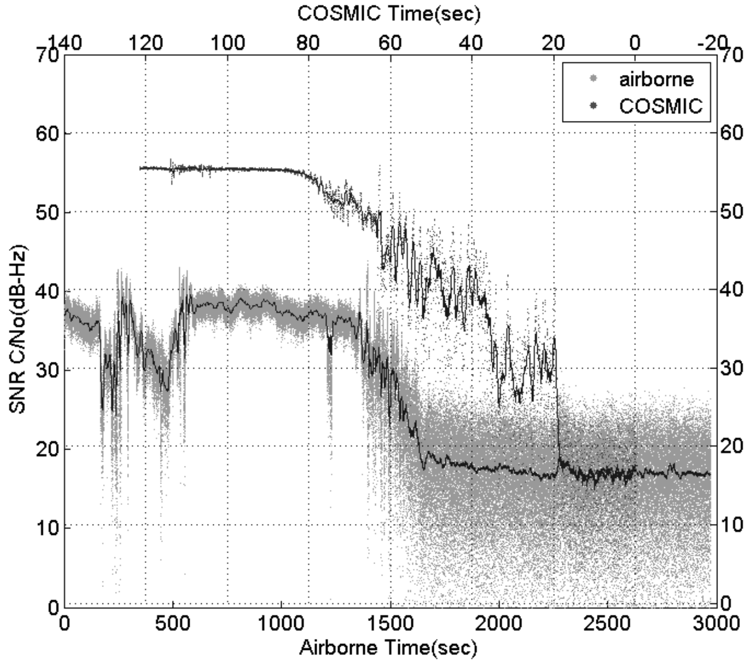

(a)

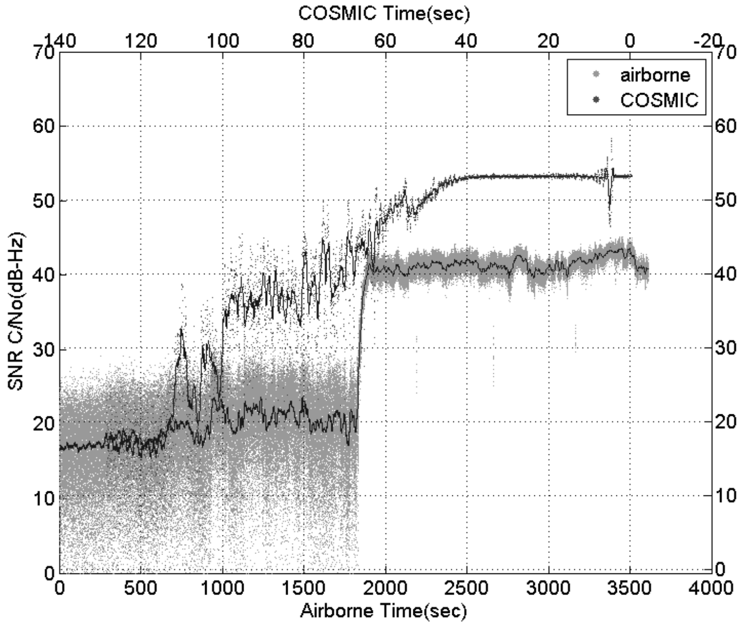

(b)

Figure 3.19. (a) Comparison of the SNR from the airborne (PRN12) (light gray dots) and spaceborne (PRN29) (dark gray dots) RO measurements on 13 September 2010 (RF18) in C/No. (b) Comparison of the SNR from the airborne (PRN17) (light gray dots) and spaceborne (PRN11) (dark gray dots) RO measurements on 14 September 2010 (RF19) in C/No. The dots are the 50 Hz data and the solid line shows the moving average with an 0.8 sec window. Note that time scales are different for spaceborne and airborne profiles.

4. Implementation of the phase matching (PM) method for the GPS airborne radio occultation (ARO) system

(MANUSCRIPT: To Be Submitted to Journal of Geophysical Research)

ABSTRACT

Airborne radio occultation (ARO) is a remote sensing technique for atmospheric sounding using the Global Positioning System (GPS) signals received by the aircraft. The atmospheric refractivity profile and parameters can be retrieved by measuring the signal delay due to the refractive medium it traverses. The ARO system is developed to complement the spaceborne RO system, which cannot provide dense soundings in a specific area. To observe transient events, such as tropical storms, with temporal resolution, an ARO system along with localized GPS-RO campaigns is needed to assist the limited observation range of traditional spaceborne RO systems.

However, both systems can suffer multipath ray propagation in the lower troposphere if there are strong refractivity gradients due to a highly variable moisture distribution. Atmospheric multipath will cause superimposed signals with different Doppler frequencies to be received at the same time, interfering with tracking as well as complicating retrievals. To untangle the bending angle with the corresponding impact parameter of each signal path, Radio-Holographic (RH) methods such as Phase Matching (PM) have been developed for spaceborne platforms. In this paper, the PM method is adapted for the ARO technique to reduce the negative bias in refractivty retrieval due to multipath effects. The phase matching functions are derived for both positive and negative elevation ray paths in ARO geometry, and the Method of Stationary Phase (MSP) is applied to determine the ARO partial bending angle. Under the assumption of spherically symmetric atmosphere, ARO PM can distinguish subsignals with different impact parameters and provide more accurate bending angle

retrieval. In addition, the climatological model and pre-filtering are utilized to process the ARO excess phase to enhance the SNR and decrease the unwrapping error rate. The retrieval results are presented of a flight campaign during September 2010 using ARO PM. With a climatological model and ARO PM, the refractivity fractional difference with ERA-I model can be maintained at an average 2% above a height of 2 km. Compared to the traditional geometrical optics (GO) method, the ARO PM can effectively decrease the refractivity negative bias up to 2 to 3% and significantly improve the retrieval accuracy of ARO.

4.1 Introduction

A radio occultation (RO) event occurs when the signal from a setting or rising GPS satellite is occulted by the Earth's limb before arriving at a receiver. The atmosphere causes signal refraction which induces a bending of the ray path and delay in the signal. The cumulative effect of this refraction is observed as a time-varying excess phase in the received signal. Excess phase can be inverted to retrieve atmospheric refractivity, pressure, temperature or water vapor profiles ([3]). Several GPS RO missions have demonstrated that this technique can accurately measure atmospheric temperature and has great potential for improving global weather prediction ([4] and [5]). Currently, even with thousands of profiles daily, GPS - Low Earth Orbit (GPS-LEO) systems cannot provide dense sounding measurements in a specific area within a given time period due to orbit constraints and the limited number of available receiver satellites. GPS RO measurements using a receiver onboard an airplane can overcome this limitation because of an aircraft's mobility and availability.

[2] described the retrieval of atmospheric profiles using the Abel inversion, a fundamental principle for the RO technique. [14] proposed a modified version of the Abel inversion for occultation measurements from a receiver within the atmosphere. The airborne RO (ARO) proof-of-concept was demonstrated by [18] with flights of the GNSS Instrument System for Multistatic and Occultation Sensing (GISMOS) over

tropical storms. The difference in the retrieval algorithm for the airborne geometry as compared to satellite RO accounts for the contribution of the atmosphere above the aircraft. The ARO geometry is shown in Figure 4.1. Under the spherical symmetry assumption, there is a corresponding positive elevation angle ray with the impact parameter $a = nrsin\psi$ for every negative elevation angle ray having the same impact parameter, where n is the refractive index , r is the distance of each location on the ray path to the center of curvature and ψ is the incident angle. The bending angle of the ray path in positive and negative elevation region are given by [14]:

$$\alpha_P = -\int_{n_A r_A}^{n_G r_G} \frac{a}{\sqrt{x^2 - a^2}} \frac{d\ln(n)}{dx} dx \tag{4.1}$$

$$\alpha_N = -2\int_{n_o r_o}^{n_A r_A} \frac{a}{\sqrt{x^2 - a^2}} \frac{d\ln(n)}{dx} dx - \int_{n_A r_A}^{n_G r_G} \frac{a}{\sqrt{x^2 - a^2}} \frac{d\ln(n)}{dx} dx \tag{4.2}$$

in which, r_G and r_A are the distance from GPS transmitter and the aircraft receiver to the center of curvature of Earth, respectively. θ is the "open angle" between r_G and r_A at the center of curvature. We can also define r_o as the distance between the tangent point to the center of curvature, which is the point closest to the the center of curvature in a ray path. n_A, n_G and n_o are the refraction indexes at the location of the ARO receiver, GPS satellite and the tangent point. n_G is usually set as zero due to the vacuum status of the GPS satellite location. Both the positive elevation bending angle α_P and the negative elevation bending angle α_N are shown in Figure 4.1. In airborne RO, the partial bending angle, $\alpha'(a) = \alpha_N(a) - \alpha_P(a)$, defined as the subtraction of the positive elevation angle bending from the negative elevation angle bending, can be inverted to produce refractivity profiles below the receiver height ([14] and [23]). The refractive index n can be calculated through the inverse Abel transform operating on the bending angle profile,

$$n(x) = n_A exp\left[\frac{1}{\pi}\int_{x}^{n_A r_A} \frac{\alpha'(a)}{\sqrt{a^2 - x^2}} da\right] \tag{4.3}$$

The independent variable $x = nr$ will give the radius r at which the refractive index $n(r)$ is retrieved. In order to utilize this algorithm for ARO refractivity retrieval, a bending angle calculation incorporating both positive and negative elevations is required. The classical Geometric Optics (GO) inversion is currently applied to the ARO partial bending angle measurements for refractivity retrieval, and the full theory is described in [23], [18] and [24].

The GO method, however, is valid only under the assumption that the received signal is transmitted by single ray path through the atmosphere. Due to the highly variable moisture distribution in the lower troposphere, the received ARO signal will suffer multipath effects from strong refractivity gradients in practice ([24], [56], and [27]). The bending angle calculation with GO under severe interference will then produce multiple values at a given impact parameter because of GO's inability to identify the superposition signals from multiple ray paths. To decrease the strong oscillation in bending angle - impact parameter calculation, the smoothing upon excess Doppler is essential to remove the high frequency components. This filtering, however, will erase not only the high frequency noise but also the refractivity profile information carried by multipath interference ([56]). As a result, the bending angle - impact parameter curve will be negative biased because of the "humps" caused by multipath in positive bending angle direction are smoothed. In addition, the method of maintaining the monotonic property of the partial bending angle - impact parameter function $\alpha'(a)$ by force also forms a negative bias in refractivity retrieval [9]. The negative bias of mean refractivity difference can be observed in ARO below 8 km height, where the moisture variation starts growing and causes interference in the received signal [24]. In [22] it is shown that the negative refractivity bias will decrease the reliability of ARO measurements and eventually limit the height of the retrieval profile. To enable refractivity retrievals when the assumption is not valid and extend the penetration to lower altitudes, Radio-Holographic (RH) methods have been developed and applied to spaceborne RO measurements. Among several proposed RH methods, the canonical transform (CT) [57], the full spectrum inversion (FSI) [25], and the phase matching (PM) [58], which utilizes the Fourier Integral Operator (FIO) are the most commonly used for spaceborne platform. CT, however, needs the back-propagation of the electromagnetic field to a straight line before it can be applied to the measurement, and this causes high computing complexity. On the other hand, the FSI can process the multipath measurement efficiently, but approximation corrections of radial variation are required to generalize FSI onto non-circular satellite orbits. In this paper, the PM method is modified to incorporate the airborne version of the Abel inversion because of its efficiency, along with its ability to be applied to a non-circular orbit, which is normally the case for aircraft trajectories. Compared to the GO method, the modified ARO PM method can largely decrease the negative refractivity retrieval bias and extend valid ARO profile height. This verifies the occurrence of the multipath effect in the lower troposphere. This paper describes the steps for applying the PM adaptation to airborne platforms, as well as the signal pre-processing for bending angle retrieval. In Section 4.2, the excess phase extraction in open-loop (OL) tracking using a climatological model with filtering is introduced to enhance the signal to noise ratio (SNR) and increase the available duration of an ARO event. The spaceborne PM method is briefly reviewed in Section 4.3, and its modification for ARO geometry is also derived and described. The refractivity retrieval result using realistic ARO experiment campaign data is shown, and the comparison between ARO PM and the traditional GO method is discussed in Section 4.4. Conclusions are provided in Section 4.6.

4.2 Climatological Model in OL Tracking

The OL processing described in [22] is useful for excess phase information extraction for each ARO event. As shown in [22], the ARO excess phase normally will not exceeds 6Hz. At this range, it is not necessary to apply an extra model to the Doppler prediction to decrease the frequency difference between the received signal and the local signal replica for sampling below Nyquist rate. However, the error model derived in [22] indicates the unwrapping error rate in excess phase calculation is highly related to SNR. More unwrapping error tends to occur when SNR is low, which usually happens at the end and the beginning of an occultation period, in setting and rising cases, respectively. The cycle slip caused by unwrapping error will more likely accumulate in the direction of the opposite sign of the residual Doppler. As a result, the observed excess phase contains significant negative bias when the tangent point height is located at low altitudes. This causes a negatively biased bending angle profile which are propagated to refractivity retrieval. To decrease the negative refractivity bias due to accumulated unwrapping error, a closer Doppler prediction for local signal replica is required for two reasons. First, a more accurate Doppler model will lead to a smaller residual phase, which may greatly decrease the amount of unwrapping and the probability to accumulate error. Second, the correlation amplitude between a received and a local signal can be magnified when the Doppler difference is reduced, thus increasing the received SNR and lowering the unwrapping error rate. [38] suggested that a more accurate Doppler model can effectively increase the SNR of the correlated result and decrease the bias of the mean signal frequency. In this research climatological Doppler estimation is used in Doppler prediction for more accurate signal replica generation of post-processing OL tracking in ARO.

For climatological excess phase estimation, the monthly mean refractivity profiles from the Climate Impact on Regional Air Quality (CIRA-Q) model [59] are utilized. In this research, the flight month (September) and approximate path latitude (20 degree) are provided, along with the interpolation method (Spline in the vertical direction and linear in the lateral direction) to retrieve average refractivity profiles. The profiles were then interpolated from the surface to a 20 km height with 0.1 km resolution. The excess phase caused by climatological refractivity profiles can be simulated with the Radio Occultation Simulator for Atmospheric Profiling (ROSAP) ([48]) ray tracing program. This program provides the excess phase $\Phi^c[k]$ with given oblateness-corrected satellite and aircraft geometry for the corresponding airborne occultation period. This estimated excess phase $\Phi^c[k]$ will then be added back into the geometric phase to generate a more accurate phase model for OL tracking. The residual phase, which is defined as the phase difference between the received and local generated signal, can be calculated from the in-phase and quadrature phase measurement of the complex correlation result by OL tracking,

$$\Phi^R[k] = U\left\{atan2\left(\frac{q[k]}{D[k]}, \frac{i[k]}{D[k]}\right)\right\} \tag{4.4}$$

in which $\Phi^R[k]$ is the residual phase at time sample k, $i[k]$ and $q[k]$ are the in-phase (real) and quadrature (imaginary) components of the correlation complex, and U is the unwrapping operator in [22]. Therefore, the signal's total phase can be acquired by summing the residual phase result with the modeled phase:

$$\Phi[k] = \Phi^R[k] + \left(\Phi^G[k] + \Phi^c[k]\right) \tag{4.5}$$

where $\Phi[k]$ is the total phase of the received signal, Φ_G is the predicted geometric phase and Φ_e is the excess phase estimation from ROSAP using the climatological model. Note that with climatological modeled phase $\Phi^c[k]$, the accumulated residual phase $\Phi^R[k]$ will be much less in order to maintain the same signal total phase. In general, by using the climatological model the residual Doppler can be reduced to under 2 Hz, which can greatly decrease the unwrapping number. Furthermore, the low frequency characteristic of the residual Doppler allows for filtering to be applied to the observed signal. In this paper, a 2 Hz bandwidth low-pass filter is used on the 50 Hz complex measurement of the correlation result before the residual phase calculation to decrease the unwrapping error rate. This filtering will largely reduce the noise power and further improve the signal SNR (V/V) to about 3.5 times.

Figure 4.2 shows the SNR, excess phase, bending angle profile using PM, and the refractivity retrieval result with and without the assistance of the climatological model in one of the ARO setting cases (RF19 PRN01). As Figure 4.2(a) shows, the SNR will be greatly enhanced by filtering the correlation result. It can be observed that at the end of occultation, the signal with the climatological model can still be identified while the one without the climatological model has already vanished. This is because the more accurately modeled phase prediction can keep the Doppler difference sufficiently small over a longer duration in order to generate correlation results in OL tracking. As a result, the valid ARO period using the climatological model is extended. To assess the improvement of the climatological model on signal phase, the excess phase is utilized:

$$\Phi^{E}[k] = \Phi^{R}[k] + \Phi^{c}[k] \tag{4.6}$$

The excess phase calculation without climatological model assistance shown in Figure 4.2(b) entered into random walk status approximately at hour 16, which indicates the OL processing can no longer track the signal at this stage. The OL processing with climatological model assistance, however, is able to keep tracking the signal through hour 16.1 before the excess phase distributed as a random walk. This extra 6 minutes in ARO data can effectively extend the lower limit of the ARO refractivity profile altitude and provide us valuable information in the lower troposphere. As the PM result shown in Figure 4.2(c), the measurement of the random walk at the end of occultation causes large negative bias at lower altitude, which will be propagated to refractivity retrieval as shown in Figure 4.2(d). With a climatological model and filtering, one can extend the effective ARO range down to the surface, which was previously limited by measurement error due to noise below 4 km.

4.3 Airborne Phase Matching (PM) Method

Radio Holographic (RH) methods can discriminate the signals from multiple ray paths using the complex signal obtained from open loop (OL) tracking. Phase Matching (PM) [58] is one of the RH methods that utilizes the method of stationary phase (MSP) to calculate the bending angle profile and its corresponding impact parameter for a noncircular orbit or flight path. In this research we modify PM to adapt the method to airborne platforms and decrease the impact of multipath effects compared to the traditional geometric optical method. The derivation and other details of PM are described in [58], and here we will focus only on the modification and implementation of the method to the ARO environment. The geometry of the ARO system is shown in Figure 4.1. During the occultation period, both $r_G(\theta)$ and $r_A(\theta)$ are functions of the open angle θ. Under the assumption of spherically symmetrical distribution of atmosphere refractivity, each ray in a occultation event can be identified by its impact parameter a. In multipath regions, the received signal with total phase Φ is the combination of many subsignals of phase Φ_j transmitted along different signal paths with distinct impact parameter a_j. The total phase Φ_j for each subsignal is related to the length of the ray path L, in radians:

$$\Phi_j = L - L_0 \tag{4.7}$$

in which j denotes the index of the subsignal, and L_0 is the constant of the initial ray path length at the beginning of the occultation. In the spaceborne case, the length of each ray path L_S, in radians, can be expressed [25] as:

$$\begin{aligned} L_S &= k\int_{r_o}^{r_L} n\frac{nr}{\sqrt{n^2r^2-a^2}}dr + k\int_{r_o}^{r_G} n\frac{nr}{\sqrt{n^2r^2-a^2}}dr \\ &= ka\left[\theta - cos^{-1}\left(a/r_L\right) - cos^{-1}\left(a/r_G\right)\right] + k\sqrt{r_L^2-a^2} + k\sqrt{r_G^2-a^2} \\ &-2k\int_a^{\infty} \sqrt{x^2-a^2}\frac{d\ln\left(n\right)}{dx}dx \end{aligned} \tag{4.8}$$

where r_L is the distance between LEO satellite to the center of curvature, $x = rn(r)$ is the refractional radius, and k is the wave number. The last term in Equation (4.8) can be written as the integral of the bending angle α:

$$-2k\int_a^{\infty} \sqrt{x^2-a^2}\frac{d\ln\left(n\right)}{dx}dx = k\int_a^{\infty} \alpha da \tag{4.9}$$

This ray path expression needs to be modified in ARO for two reasons, however. First, the ARO receiver is located inside the Earth atmosphere where the refractive index at the receiver cannot be neglected. Second, the two distinctive ARO ray path groups, positive elevation and negative elevation, should be treated differently. In contrast to the negative elevation ARO and spaceborne RO ray path, in positive elevation ARO events the transmitter and the receiver located at the same side of ray path relative to the tangent point. Therefore, in airborne PM we modify the signal path expression in the positive elevation to:

$$\begin{aligned} L_{A,p} &= -k\int_{r_o}^{r_A} n\frac{nr}{\sqrt{n^2r^2-a^2}}dr + k\int_{r_o}^{r_G} n\frac{nr}{\sqrt{n^2r^2-a^2}}dr \\ &= ka\left[\theta + cos^{-1}\left(\frac{a}{n_A r_A}\right) - cos^{-1}\left(\frac{a}{r_G}\right)\right] - k\sqrt{n_A^2 r_A^2 - a^2} + k\sqrt{r_G^2 - a^2} \\ &+k\int_{n_o r_o}^{n_A r_A}\sqrt{x^2-a^2}\frac{d\ln(n)}{dx}dx - k\int_{n_o r_o}^{n_G r_G}\sqrt{x^2-a^2}\frac{d\ln(n)}{dx}dx \end{aligned} \tag{4.10}$$

Note that the $n_A r_A$ is used in Equation (4.10) instead of r_A. The term n_A is essential in airborne case since the receiver remains in the atmosphere, and the refraction index at the receiver location will not be unity. In practice, n_A can be calculated by in situ flight level data ([24]). A negative sign is added to the first term of Equation (4.10) because the transmitter and the receiver are located on the same side, and the path length from the tangent point to the receiver should be subtracted from the path between the tangent point and transmitter in the calculation of the total path length. The sum of the last two terms can be derived with Equation (4.1) as the integral of the bending angle with respect to the impact parameter in positive elevation:

$$k\int_{n_o r_o}^{n_A r_A}\sqrt{x^2-a^2}\frac{d\ln(n)}{dx}dx - k\int_{n_o r_o}^{n_G r_G}\sqrt{x^2-a^2}\frac{d\ln(n)}{dx}dx = k\int_a^{\infty}\alpha_P da \tag{4.11}$$

On the other hand, for negative elevation, the airborne ray path length function will be the same as for a spaceborne platform since the receiver location is at the different side of the path as in the spaceborn case, except the term n_A should also be included:

$$\begin{aligned} L_{A,n} &= k\int_{r_o}^{r_A} n\frac{nr}{\sqrt{n^2r^2-a^2}}dr + k\int_{r_o}^{r_G} n\frac{nr}{\sqrt{n^2r^2-a^2}}dr \\ &= ka\left[\theta - cos^{-1}\left(\frac{a}{n_A r_A}\right) - cos^{-1}\left(\frac{a}{r_G}\right)\right] + k\sqrt{n_A^2 r_A^2 - a^2} + k\sqrt{r_G^2 - a^2} \\ &-k\int_{n_o r_o}^{n_A r_A}\sqrt{x^2-a^2}\frac{d\ln(n)}{dx}dx - k\int_{n_o r_o}^{n_G r_G}\sqrt{x^2-a^2}\frac{d\ln(n)}{dx}dx \end{aligned} \tag{4.12}$$

and the last two terms can also be expressed with positive bending angle by equation (4.2):

$$-k\int_{n_o r_o}^{n_A r_A}\sqrt{x^2-a^2}\frac{d\ln(n)}{dx}dx - k\int_{n_o r_o}^{n_G r_G}\sqrt{x^2-a^2}\frac{d\ln(n)}{dx}dx = k\int_a^{\infty}\alpha_N da \qquad (4.13)$$

Since the last two terms are independent of time, or the open angle θ, the derivative of the path length with respect to θ can be written as:

$$\frac{L_{A,p}}{d\theta} = k\left[\frac{-\sqrt{n_A^2 r_A^2 - a_i^2}}{n_A r_A}\left(r_A\frac{dn_A}{d\theta} + n_A\frac{dr_A}{d\theta}\right) + \frac{\sqrt{r_G^2 - a_i^2}}{r_G}\frac{dr_G}{d\theta}\right] + ka_i \qquad (4.14)$$

$$\frac{L_{A,n}}{d\theta} = k\left[\frac{\sqrt{n_A^2 r_A^2 - a_i^2}}{n_A r_A}\left(r_A\frac{dn_A}{d\theta} + n_A\frac{dr_A}{d\theta}\right) + \frac{\sqrt{r_G^2 - a_i^2}}{r_G}\frac{dr_G}{d\theta}\right] + ka_i \qquad (4.15)$$

The objective of the ARO PM is to acquire the bending angle information α_p and α_n from the total phase measurement Φ. To extract the bending angle, one must know the geometry of each subsignal ray path in advance as well as its corresponding arriving open angle. This can be done by the Method of Stationary Phase (MSP). If the phase matching functions are chosen as:

$$S_p(a_j,\theta) = ka_j\left[\theta + cos^{-1}\left(\frac{a_j}{n_A r_A}\right) - cos^{-1}\left(\frac{a_j}{r_G}\right)\right] - k\sqrt{n_A^2 r_A^2 - a_j^2} + k\sqrt{r_G^2 - a_j^2} \qquad (4.16)$$

$$S_n(a_j,\theta) = ka_j\left[\theta - cos^{-1}\left(\frac{a_j}{n_A r_A}\right) - cos^{-1}\left(\frac{a_j}{r_G}\right)\right] + k\sqrt{n_A^2 r_A^2 - a_j^2} + k\sqrt{r_G^2 - a_j^2} \qquad (4.17)$$

where a_j is the impact parameter for each subsignal we chose, then the derivative of the phase matching function $dS_p/d\theta$ and $dS_n/d\theta$ will be equal to the path length derivative $dL_{A,p}/d\theta$ (Equation 4.14) and $dL_{A,n}/d\theta$ (Equation 4.15) respectively only when the impact parameter of the subsignal a is identical with the chosen a_j. These two phase matching functions, which can be regarded as the approximation of the ray paths, consist of two straight lines from the GPS transceiver to the impact parameter and an arc to connect both lines. The paths are illustrated in Figure 4.3. For positive elevation (Figure 4.3(a)), the ray path is approximated as the receiver straight line (gray dashed line) subtracted from the sum of the transmitter straight line and the arc (gray solid line) due to the negative sign of the first term in Equation (4.10). In contrast, in the negative elevation case both straight lines to the transmitter and the receiver as well as the arc are summed to approximate the ray path. The approximation functions are useful when calculating the stationary phase with MSP integral. We can integrate the phase difference between the observed total phase and the constructed path length phase function $S\left(a_j, \theta\right)$ at each θ:

$$v(a_j) = \int A\left(\theta\right) exp\left[i\Phi\left(\theta\right) - iS\left(a_j, \theta\right)\right] d\theta \tag{4.18}$$

where A is the amplitude and Φ is the total phase of the received signal. By MSP, this integration function with given impact parameter a_j in (4.18) will be a complex number in which its phase is equal to the phase difference between the subsignal and the phase matching function at a stationary point $\theta_{s,j}$,

$$v(a_j) \cong \sqrt{\frac{2\pi i}{\ddot{\Phi}_j\left(\theta_{s,j}\right) - \ddot{S}\left(a_j, \theta_{s,j}\right)}} A(\theta_{s,j}) exp\left[i\Phi_j(\theta_{s,j}) - ikS\left(a, \theta_{s,j}\right)\right] \tag{4.19}$$

The rapid phase change will cause the integral to vanish if the subsignal's stationary point doesn't exist. As a result, only a subsignal received during the occultation period will cause the integral to converge to a nonzero value. The stationary point $\theta_{s,j}$, which is different for each subsignal, is determined as the open angle when the derivative of the received subsignal phase and the ray path length phase with respect to the open angle are equal:

$$\frac{d\Phi_j(\theta)}{d\theta} = \frac{S(a_j, \theta)}{d\theta} \tag{4.20}$$

By combining the Equations (4.7), (4.16) and (4.17), the equality in Equation (4.20) only exists when the subsignal arriving at stationary point $\theta_{s,j}$ has the impact parameter a_j. In this way the complex number with the phase of the difference between observed subsignal and calculated ray path can be calculated for each a_j without knowing its corresponding $\theta(a_j)$ previously. The result is a complex function of impact parameter a,

$$v(a) = B\left(a\right) exp\left[i\Psi\left(a\right)\right] \tag{4.21}$$

The phase of $v\left(a\right)$, $\Psi\left(a\right)$, is the result of the last two terms of Equations (4.10) and (4.12). In practice, $\Psi\left(a\right)$ can be smoothed to remove noise. Differentiation of $\Psi\left(a\right)$ with respect to the impact parameter will then give the value of the corresponding bending angle of given impact parameter a:

$$\alpha(a) = -k^{-1}\frac{d\Psi\left(a\right)}{da} \tag{4.22}$$

The bending angle profile for positive and negative elevation angles can be calculated separately with Equations (4.21) and (4.22) at corresponding times in an ARO period. We can then acquire the partial bending angle profile and use this for the ARO inverse Abel transform described in Section 1.

4.4 Results

The hardware installation of GISMOS was described by [22] and [24]. In this research the data sets recorded during the Pre-Depression Investigation of Cloud-systems in the Tropics (PREDICT) campaign are analyzed. This flight campaign was planned to investigate the moisture development during the genesis phase of hurricane Karl ([24]) and the flight path crossed the Caribbean Sea while the cyclone system moved west during the campaign. The data sets from five research flights used in this research were recorded on 9, 11, 12, 13, and 14, September 2010. These four flights are numbered as RF14, RF16, RF17, RF18, and RF19, respectively. The flight trajectories are shown in Figure 4.4. As Figure 4.4 shows, a modified lawnmower pattern was flown to regularly sample the development region, except for the avoidance of deep convection locations. The significant amount of moisture at lower altitudes due to the tropical oceanic area that the flight passed through, as well as the timing of the campaign in late summer, was expected to cause multipath effect and interfere with RO measurements. These five research flight trajectories are further examined in Figure 4.5, and each occultation event used for processing is marked. In ARO, the tangent point drift usually exceeds 400 km horizontally and is represented as grey dash lines in Figure 4.5. The x marks are the locations of the occultation points for each occultation, defined as the location of tangent point at 5.9 km altitude. There are 13, 8, 10, 13, and 15 occultation events occur in RF14, RF16, RF17, RF18, and RF19 respectively, and therefore 59 ARO events in total. The GO and PM methods are applied to these recorded ARO data and the refractivity profile for each case is retrieved by inverse Abel. The retrieved refractivities are then compared with those from the ERA-interim model at the closest grid to the occultation point.

The results of GO and PM of each research flights are shown in the top and bottom panels respectively for each subfigure of Figure 4.6. The grey lines are the refractivity retrieval of each case, the black solid lines are the retrieval average of the specific research flight, and the black dash line indicate the 1-σ range of the retrieval. It can be observed that the refractivity retrieval by using GO will be negatively biased compared to ERA-I model below 7 km, which is about the height where the amount of the moisture start accumulating. The biased refractivity fractional difference varies in each cases, while the mean negative bias of -2% to -5% are shown between 2 to 6 km which suggests the occurrence of the multipath effect at lower troposphere. This bias can be greatly reduced by using PM instead of GO for bending angle calculation. As shown in PM results for each research flight, the mean fractional difference can be maintained between -2% to 2% above 2 km. The refractivity retrieval compared to the ERA-I model for all 59 cases are shown in Figure 4.7. As the figure shows the mean fractional difference start being biased from 7 km, and the bias reaches -3%

at about 5 km through the surface. In contrast, the mean fractional difference using PM is less than 1% until 2 km height and just slightly biased at 2 to 4 km. The fractional difference standard deviation in both GO and PM are increasing in lower troposphere, but 2% s.t.d of PM is slightly better than 3% s.t.d by using GO. This unbiased and more accurate result above 2 km using PM can greatly improve the performance of data assimilation in weather prediction models.

Both mean refractivity fractional difference for GO and PM are shown in Figure 4.8 for each research flight. The fractional difference have 2% increment in average from 2 to 6 km when calculated by PM, and 1% from 6 to 8 km. This increment, which normally complement the negative bias at lower height, varies from 0 to 4% in different research flights. The variation might depends on the regional moisture distribution, flight path, the location of occultation occurrence, and the tangent point trajectories for each research flight experiment. In addition, although the ERA-I model is used as a reference in the research, this measurement dependent model should not be taken as the absolute ”truth” of the environment. Note that both refractivity retrieval with PM and GO in RF17 have a sharp decreasing at about 5 km altitude compared to the ERA-I model. This sudden drop in refractivity retrieval may related to the location difference between the occultation points which locates inside the Karl system, and the dropsondes which were released at flight path that avoid the deep convection. In this particular case ARO measurement may provide more reliable information for atmosphere refractivity profile calculation. The PM and GO results compared to the nearby dropsondes measurements are shown in Figure 4.9. The reference dropsonde profiles are picked within 3 hours and 250 km difference in time and distance from the occultation points. The comparison shown in Figure 4.9 contains 44 ARO results in total due to the time and distance criteria could not be satisfy for every occultations. As the figure shows, the standard deviation is larger at lower troposphere in both PM and GO compared to that with ERA-I model. However, the improvement of more than 2% in refractivity retrieval can still be observed from 2 to 6 km.

4.5 Error Analysis

One of the most obvious error in PM results is the retrieval under 2 km. As shown in Figure 4.7 and Figure 4.9, the biased fractional difference can reach −5% when compared to ERA-I model close to the surface, and even reach −8% when compared to the dropsonde data. The serious negative bias which makes ARO measurements almost not usable below 2 km can be explained by two causes. The first reason is the low SNR of the received ARO signal at lower altitude. At this altitude the residual signal phase in OL tracking could be mainly composed of Gaussian noise due to extremely weak received signal strength. The unwrapped residual phase will then become random walk with zero mean, which cause the refractivity retrieval is calculated only by known geometrical and climatological models. As a result, the refractivity retrieval will converge to the climatological refractivity profile at lower altitude. The climatological refractivity profile for each ARO case from RF16 to RF19 compared to the corresponding ERA-I model are shown in Figure 4.10. It can be seen that the climatological model has −5% negative bias at the surface compared to ERA-I, which can approximately explain the −5% bias observed in Figure 4.7. Another reason which could cause the negative bias is the cut-off time in OL tracking which was stated in [26]. Since the large bending angle subsignals are always received in low elevation, earlier cut-off time in setting cases or later cut-off time in rising cases could truncate the subsignals with larger bending angle and causing negative bias in PM. In this research the cut-off time is set when the single ray path given by ROSAP ray tracing program touches the surface of the earth. This cut-off time determination might be too conservative that the following large bending subsignals are truncated, which cause negative bias when calculating the bending angle.

Another error can be observed when the bending angle and refracitivity retrieval are applied on setting and rising cases separately. The retrieval results of the setting and rising cases compared to ERA-I model are shown in Figure 4.11. It can be observed in the figure that the fractional difference of the rising cases have positive bias at about 0.5 to 1% at all altitude, whereas the negative bias of 1 to 2% are shown in the setting cases. Currently no conclusion is made for the cause of this rising-setting bias, which will be studied and investigated in the future.

4.6 Conclusion

As a complementary system for regional atmospheric sounding to assist traditional spaceborne GPS RO, the negative biased refractivity retrieval caused by mis-modeling and multipath effect at lower troposphere will downgrades the applicability of the ARO data. To reduce the negative bias, this paper utilize the combination of climatplogical model and the ray tracing program to provide more accurate phase model and enhance the SNR at lower heights. Large amount of unwrapping error in excess phase can thus be removed by reducing the number of unwrapping and decreasing the unwrapping error rate. In addition, we adapt the PM method to the airborne platform to distinguish different subsignals arriving at the same time and untangle the multipath of the GPS RO signal due to complicated structure of moisture variation. The using of radio holographic method can greatly improve the bending angle calculation and decrease the refractivity retrieval negative bias from -3% fractional difference to less than -1% in average between 2 and 8 km height while retaining 2% standard deviation. A negative bias using PM can still be observed below 2 km, which might caused by higher cut-off height and extremely low SNR due to low elevation and limited antenna gain pattern. The refractivity retrieval bias in rising and setting case could also attributes to forward and backward OL tracking difference which should be further investigated in the future studies.

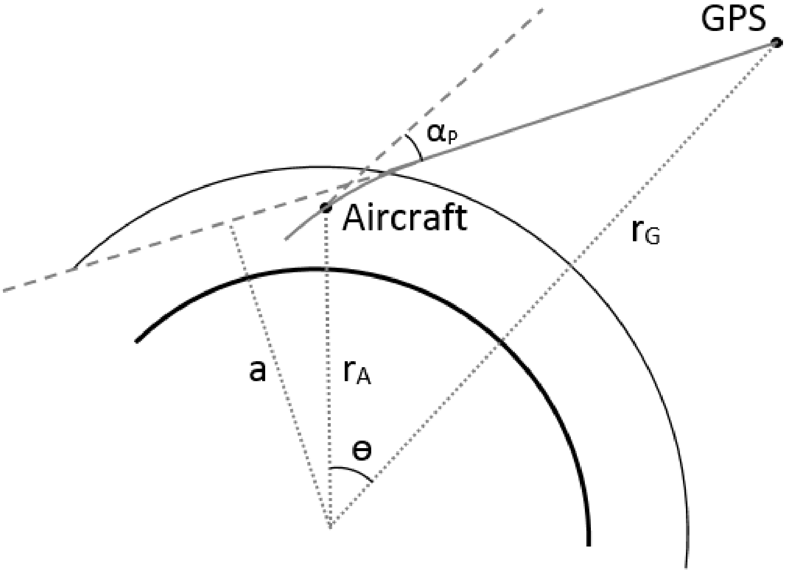

(a)

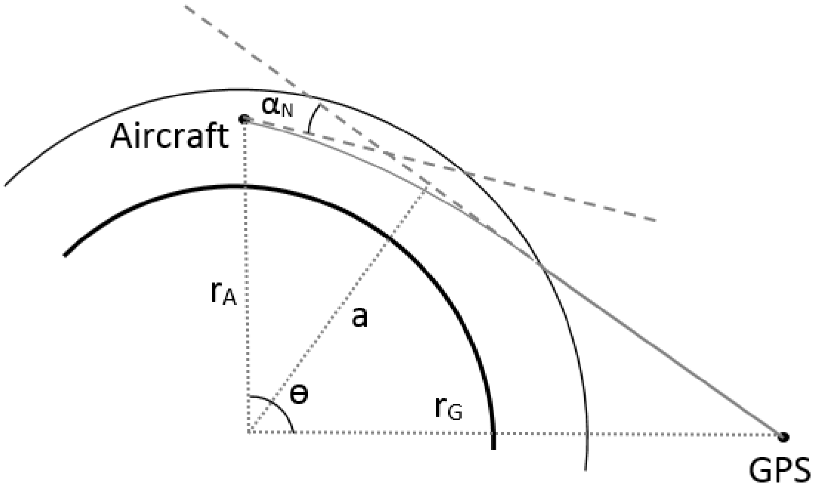

(b)

Figure 4.1. The ARO geometry for (a) positive elevation and (b) negative elevation. a is the impact parameter, r_A and r_G are the distance from the center of curvature to the aircraft and GPS satellite, respectively. θ is the open angle, and α_P and α_N are the bending angles. As the figure shows, there is a corresponding positive elevation angle ray with the impact parameter a for every negative elevation angle ray having the same impact parameter

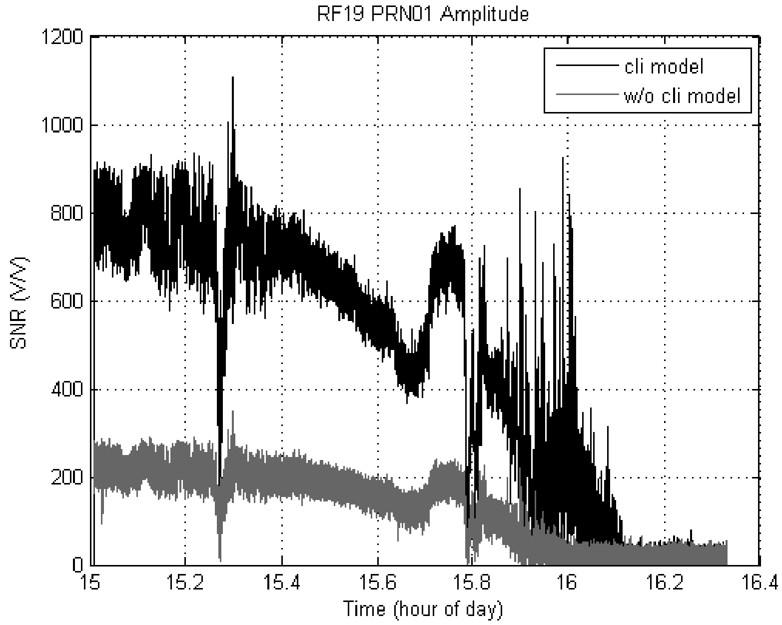
RF19 PRN01 Amplitude
SNR (V/V)
1200
1000
800
600
400
200
0
15
15.2
15.4
15.6
15.8
16
16.2
16.4
Time (hour of day)
cli model
w/o cli model

(a)

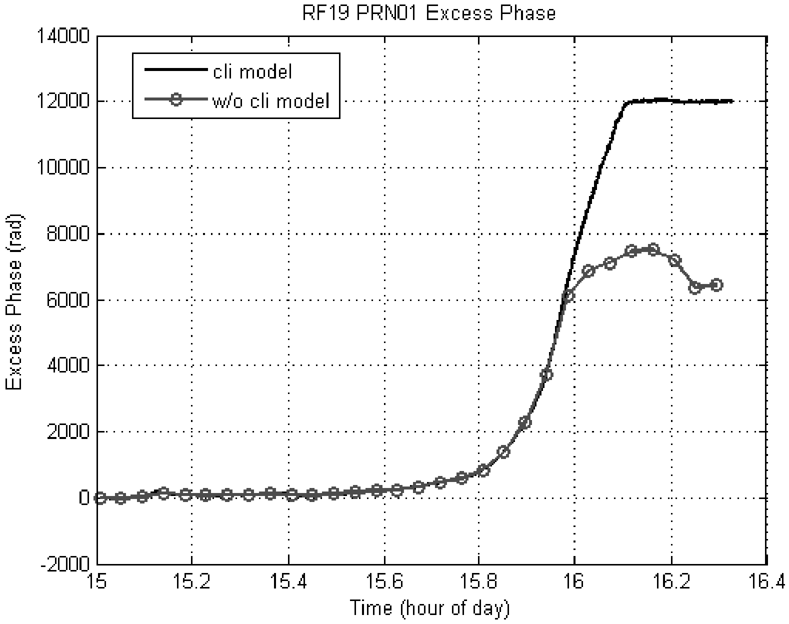
RF19 PRN01 Excess Phase
Excess Phase (rad)
14000
12000
10000
8000
6000
4000
2000
0
-2000
15
15.2
15.4
15.6
15.8
16
16.2
16.4
Time (hour of day)
cli model
w/o cli model

(b)

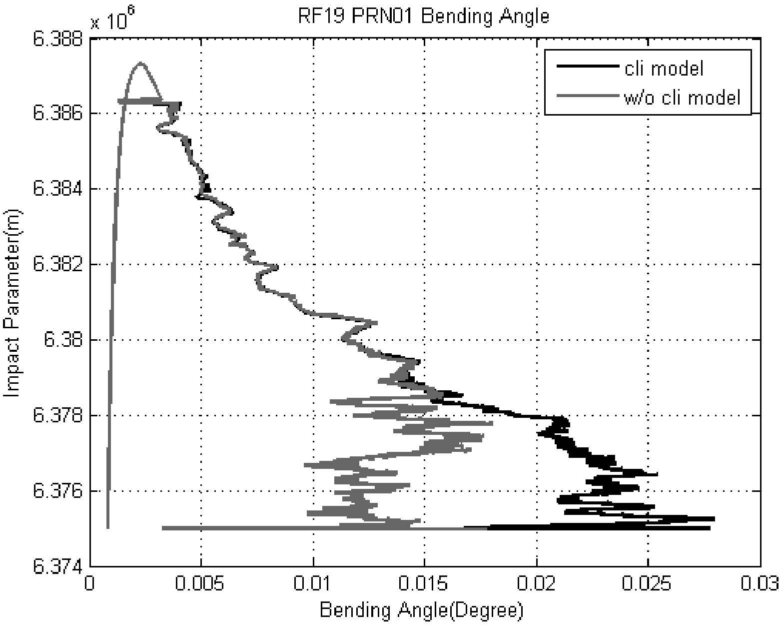

(c)

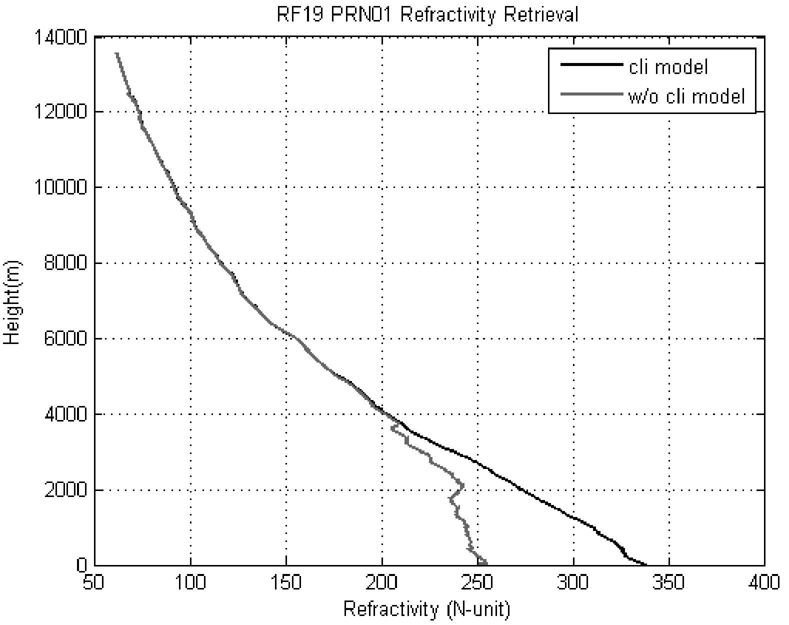

(d)

Figure 4.2. The (a) SNR (b) excess phase (c) bending angle and (d) refractivity retrieval of the case RF19 PRN01 using the phase model with and without the assistance of the climatological model. The SNR is largely increased at the end of occultation when using the climatological model, which allows the excess phase to be calculated after hour 16. Note that the sudden SNR change at hour 15.8 is due to the turns made by the aircraft. The phase matching method is used in both cases, and the reduction of the unwrapping error largely decrease the negative bias at lower height.

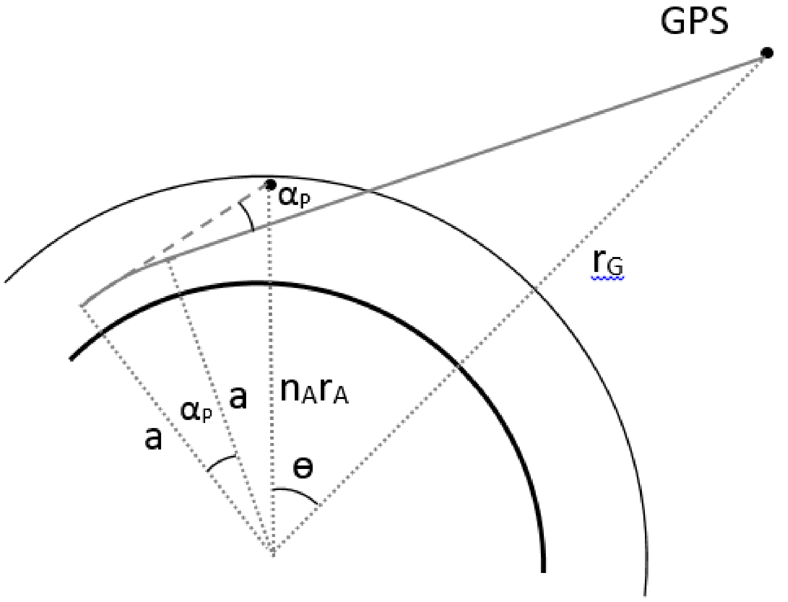

(a)

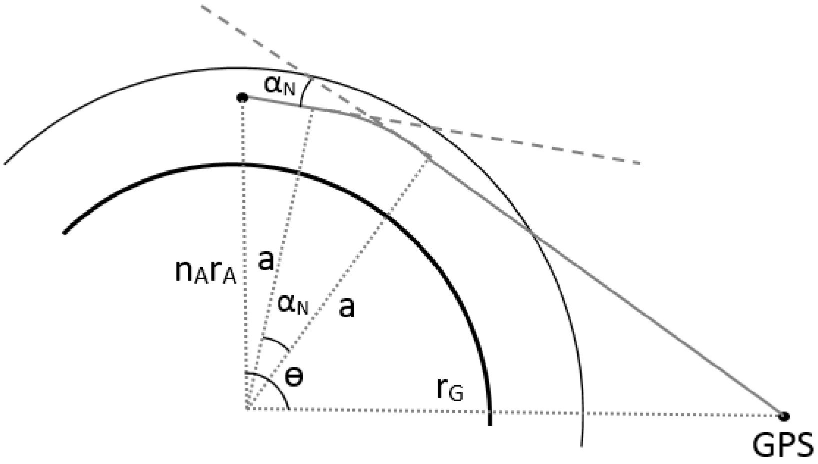

(b)

Figure 4.3. The ray path approximation used in ARO phase matching for (a) positive elevation and (b) negative elevation. Note that in this approximation the ray path end is at the point where its distance to the center of curvature is $n_A r_A$ instead of r_A.

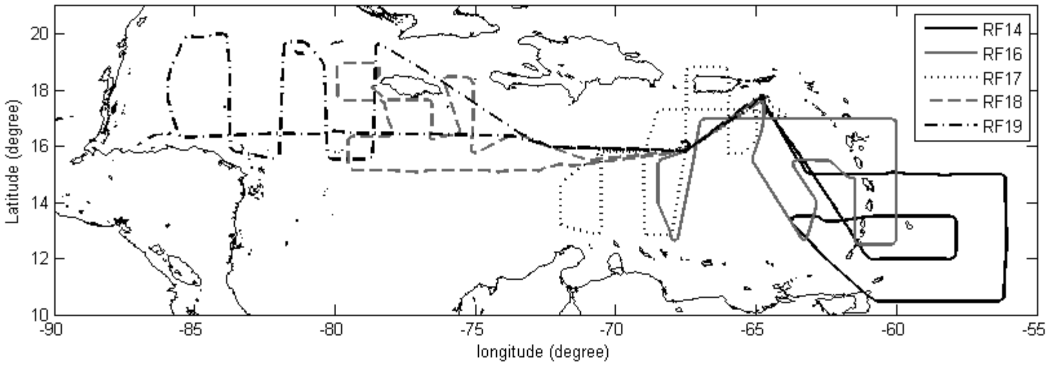

Figure 4.4. The flight path of all four research flights in the PREDICT campaign which crossed the Caribbean Sea on 11 to 14 September, 2010 to observe the cyclogenesis process of hurricane Karl. Each flight is identified by different line styles.

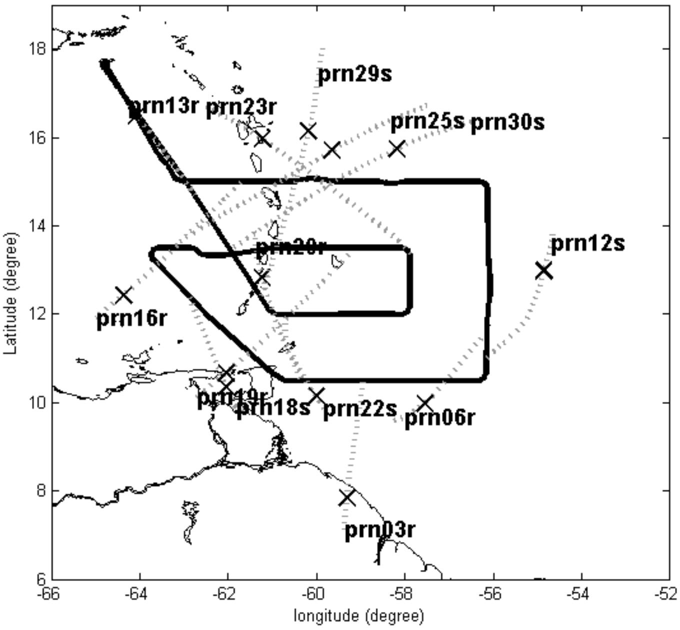
prn29s
prn13r
prn23r
prn25s
prn30s
prn20r
prn12s
prn16r
prn19r
prn18s
prn22s
prn06r
prn03r
18
16
14
12
10
8
6
-66
-64
-62
-60
-58
-56
-54
-52
Latitude (degree)
longitude (degree)

(a)

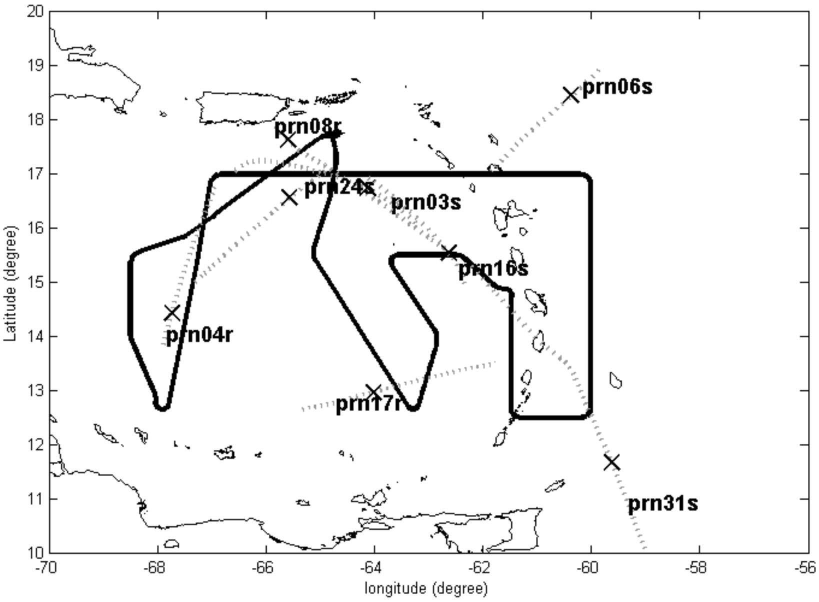
prn06s
prn08r
prn24s
prn03s
prn16s
prn04r
prn17r
prn31s
20
19
18
17
16
15
14
13
12
11
10
-70
-68
-66
-64
-62
-60
-58
-56
Latitude (degree)
longitude (degree)

(b)

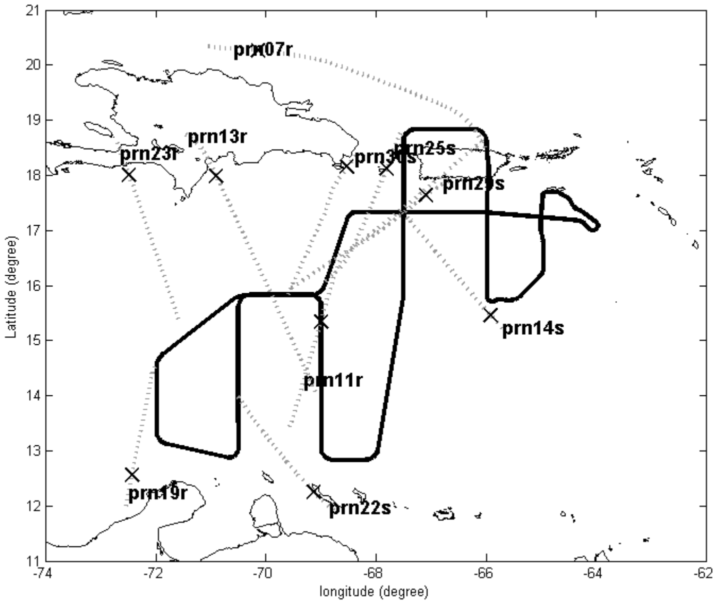
prn07r
prn13r
prn23r
prn30s
prn25s
prn29s
prn14s
prn11r
prn19r
prn22s
Latitude (degree)
longitude (degree)
21
20
19
18
17
16
15
14
13
12
11
-74
-72
-70
-68
-66
-64
-62

(c)

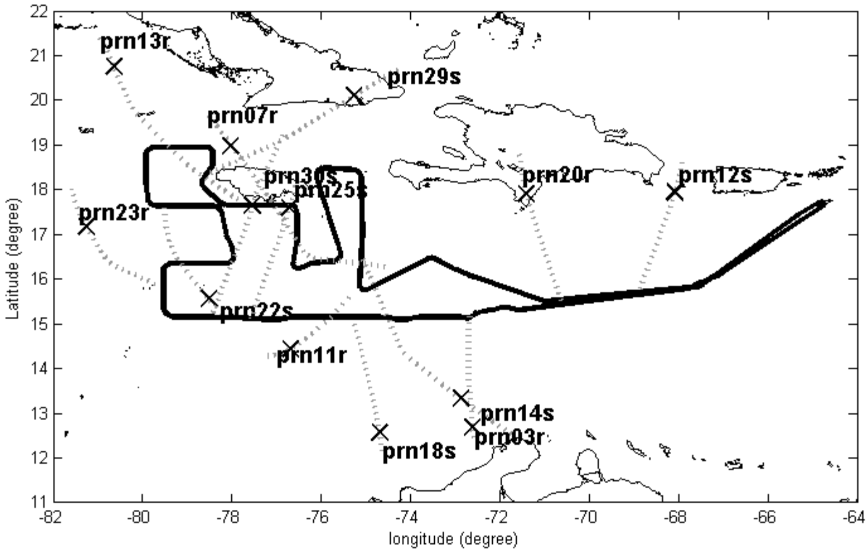
prn13r
prn29s
prn07r
prn30s
prn25s
prn20r
prn12s
prn23r
prn22s
prn11r
prn14s
prn03r
prn18s
Latitude (degree)
longitude (degree)
22
21
20
19
18
17
16
15
14
13
12
11
-82
-80
-78
-76
-74
-72
-70
-68
-66
-64

(d)

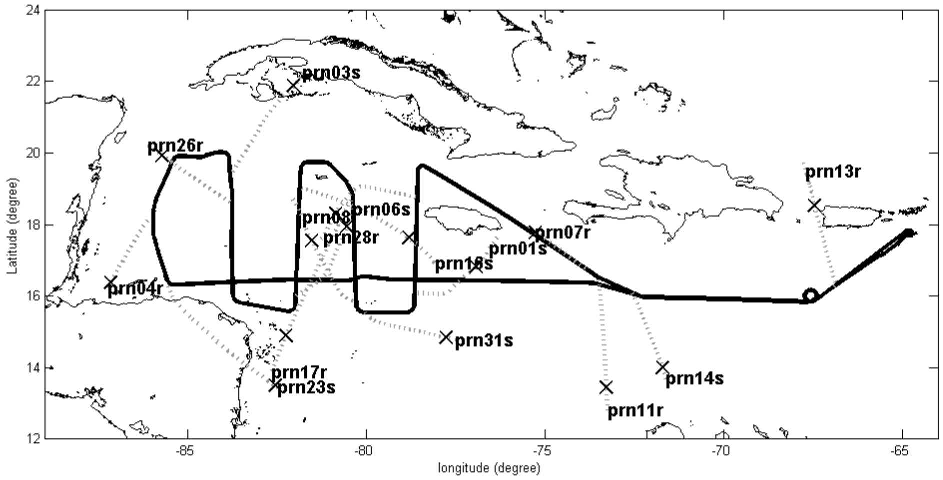

(e)

Figure 4.5. The maps for each research flight of (a)RF14 (b)RF16 (c)RF17 (d)RF18 (e)RF19. The flight trajectories are plotted with solid black lines. The grey dashed line is the tangent point drift for each occultation, and the black cross is the occultation point which is located at the tangent point location at 5.9 km height.

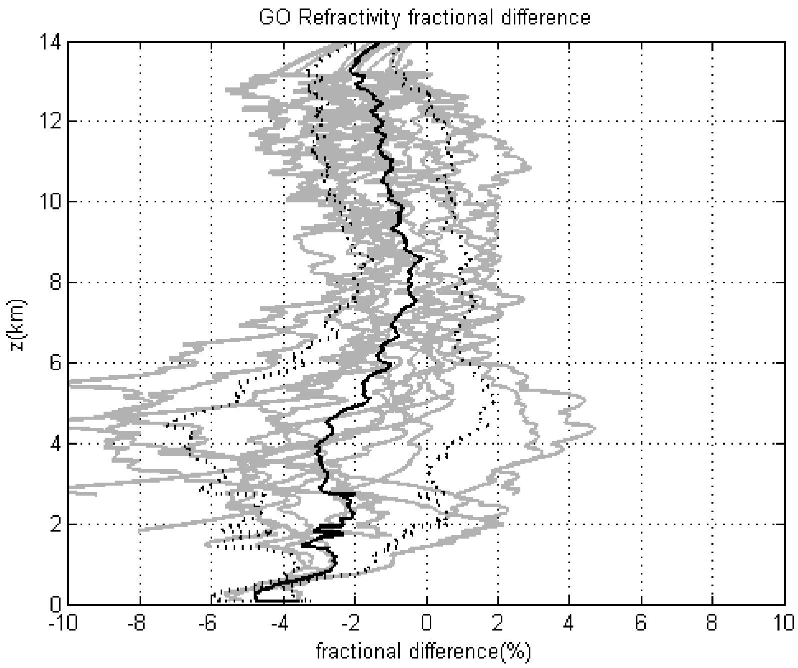
GO Refractivity fractional difference
z(km)
fractional difference(%)
0
2
4
6
8
10
12
14
-10
-8
-6
-4
-2
0
2
4
6
8
10

(a)

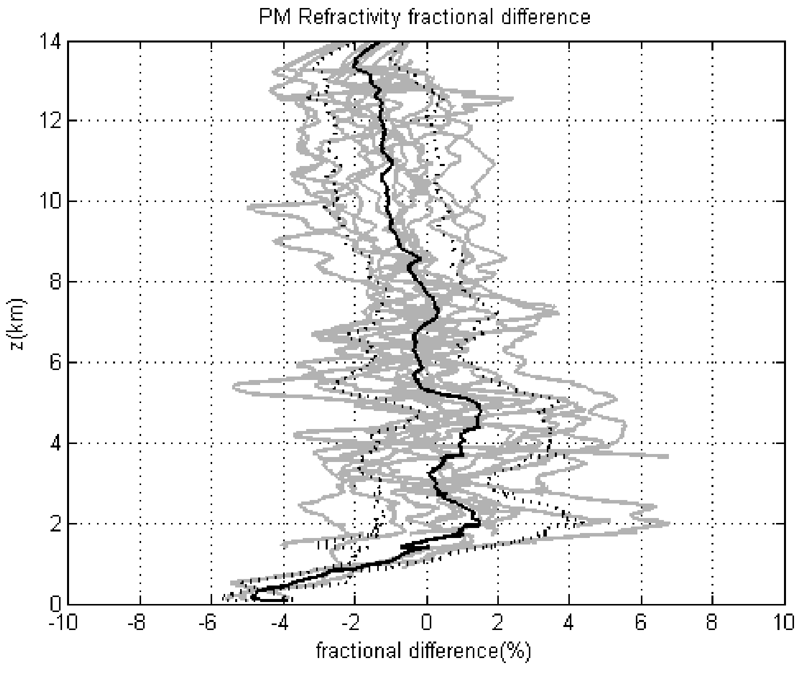
PM Refractivity fractional difference
z(km)
fractional difference(%)
0
2
4
6
8
10
12
14
-10
-8
-6
-4
-2
0
2
4
6
8
10

(b)

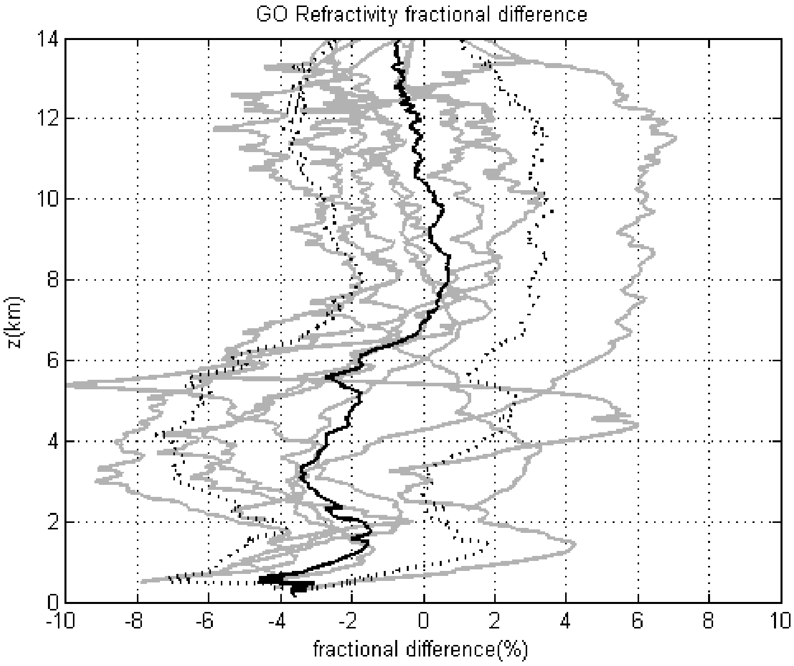
GO Refractivity fractional difference
z(km)
0
2
4
6
8
10
12
14
-10
-8
-6
-4
-2
0
2
4
6
8
10
fractional difference(%)

(c)

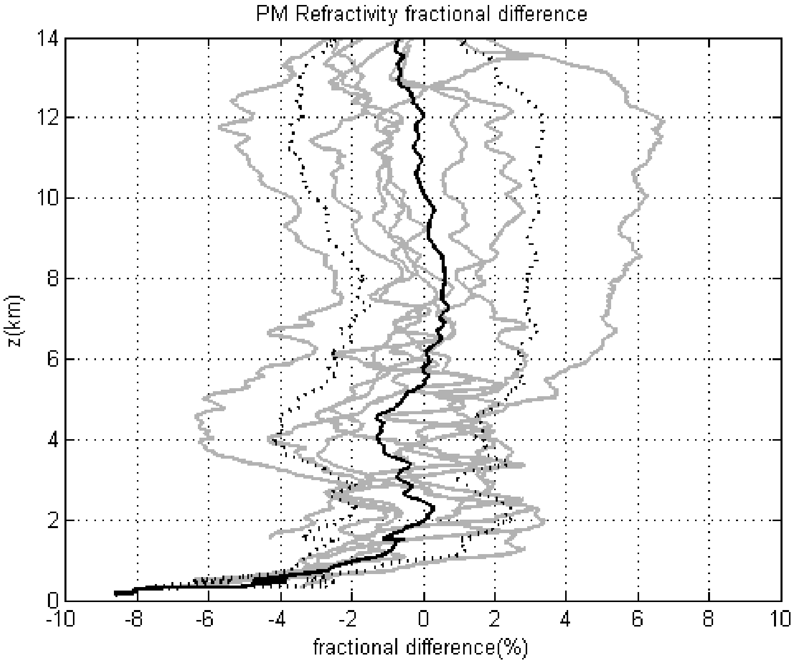
PM Refractivity fractional difference
z(km)
0
2
4
6
8
10
12
14
-10
-8
-6
-4
-2
0
2
4
6
8
10
fractional difference(%)

(d)

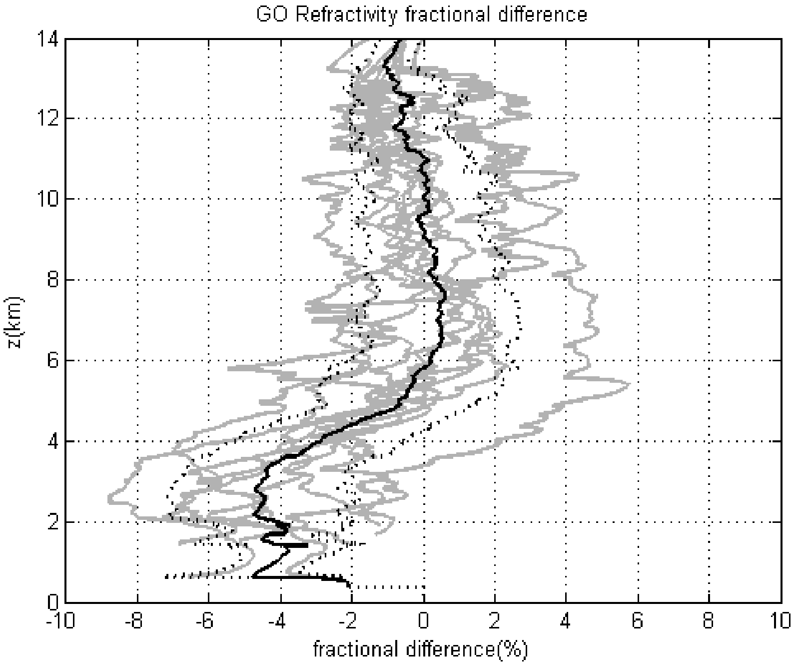
GO Refractivity fractional difference
z(km)
0
2
4
6
8
10
12
14
-10
-8
-6
-4
-2
0
2
4
6
8
10
fractional difference(%)

(e)

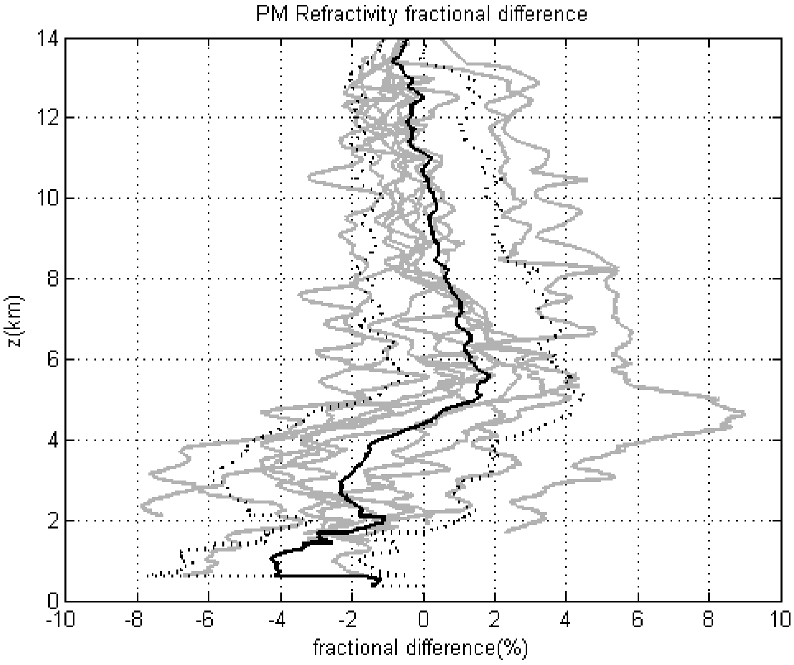
PM Refractivity fractional difference
z(km)
0
2
4
6
8
10
12
14
-10
-8
-6
-4
-2
0
2
4
6
8
10
fractional difference(%)

(f)

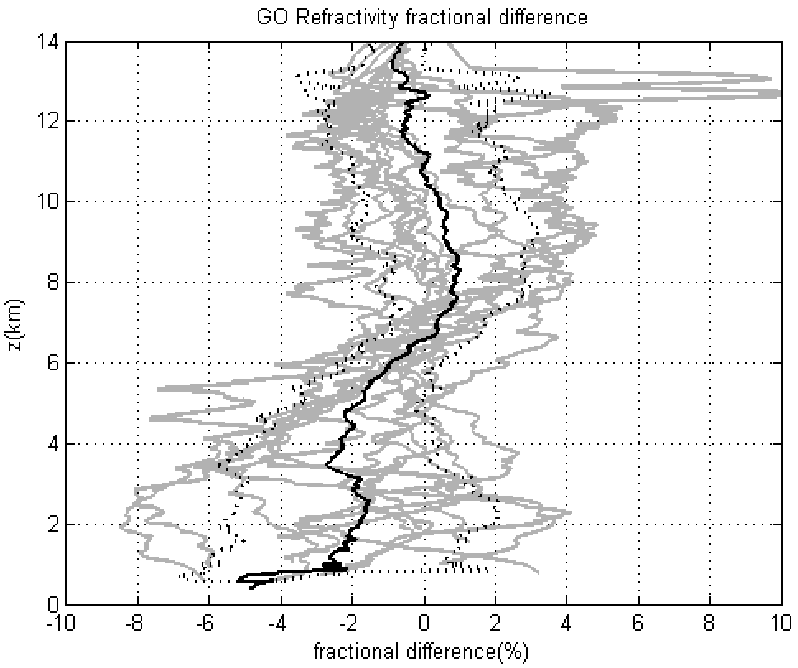
GO Refractivity fractional difference
z(km)
fractional difference(%)
0
2
4
6
8
10
12
14
-10
-8
-6
-4
-2
0
2
4
6
8
10

(g)

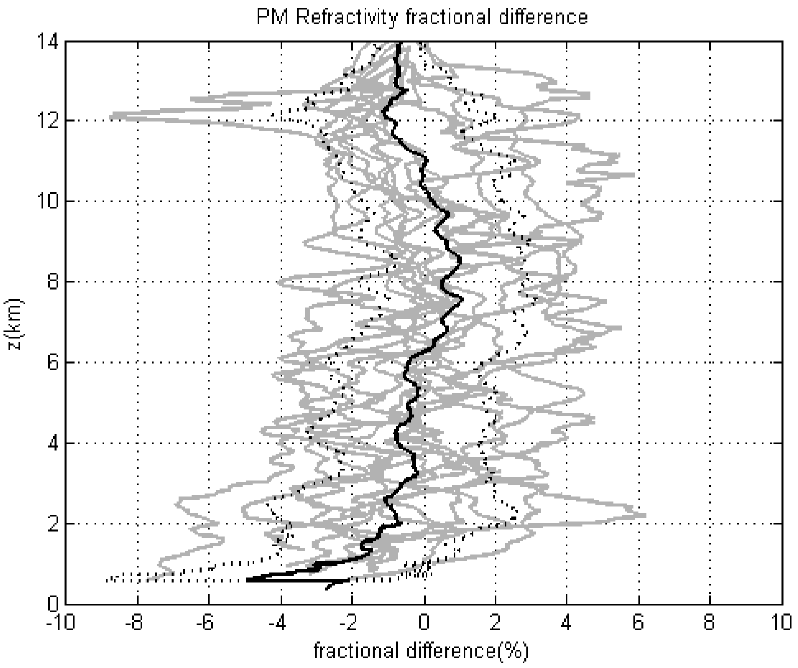
PM Refractivity fractional difference
z(km)
fractional difference(%)
0
2
4
6
8
10
12
14
-10
-8
-6
-4
-2
0
2
4
6
8
10

(h)

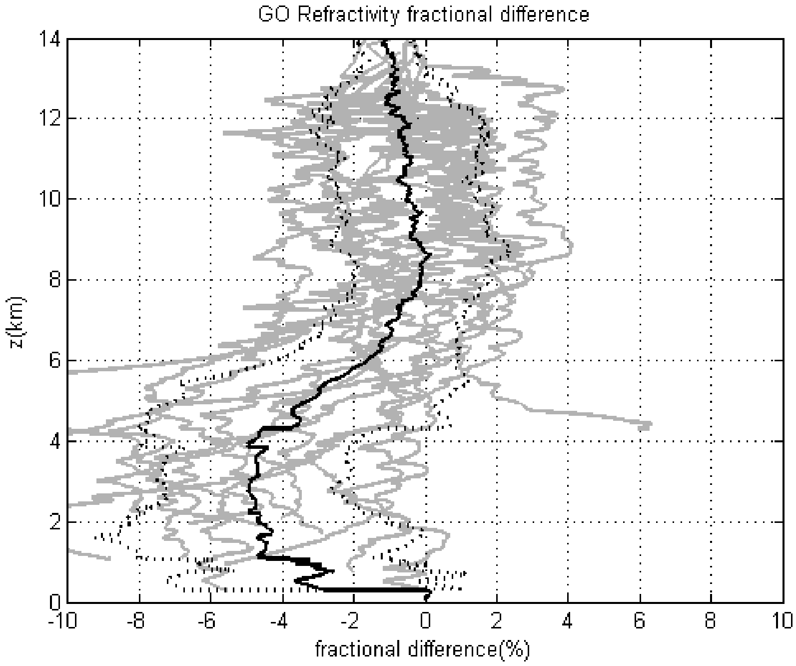

(i)

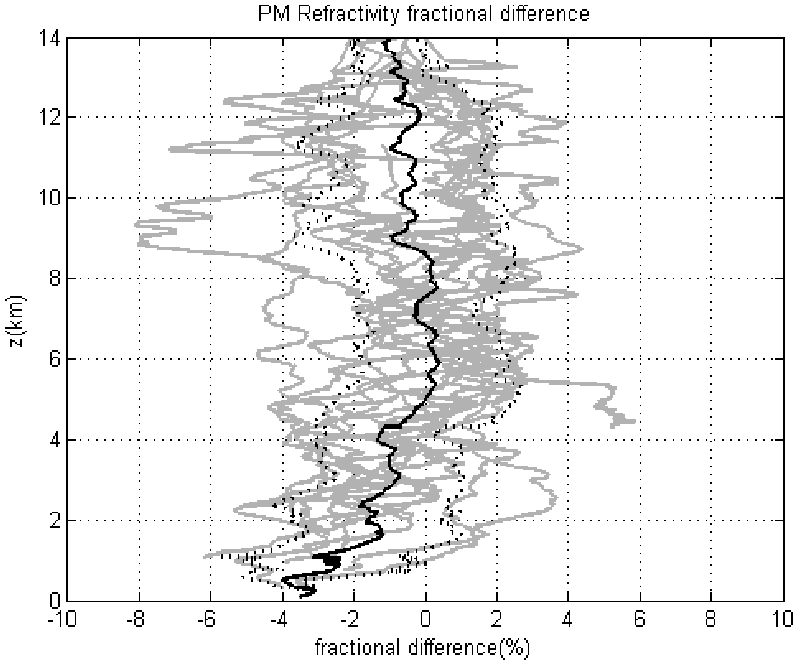

(j)

Figure 4.6. The fractional difference of the ARO refractivity retrieval compared to the ERA-I model for (a)(b)RF14 (c)(d)RF16 (e)(f)RF17 (g)(h)RF18 (i)(j)RF19. The first subfigure of each page is calculated by GO, while the second is calculated by PM. Grey lines are the retrievals for each case, black solid line is the average, and the dashed line is the range of 1-σ. The retrieval results between 2 to 8 km are greatly improved while using PM.

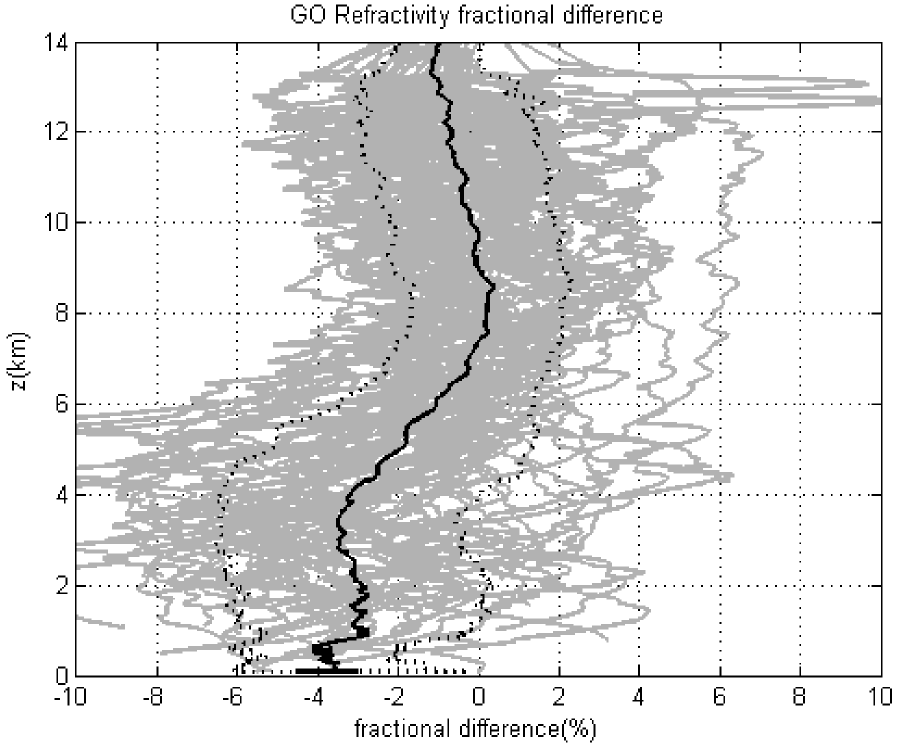

(a)

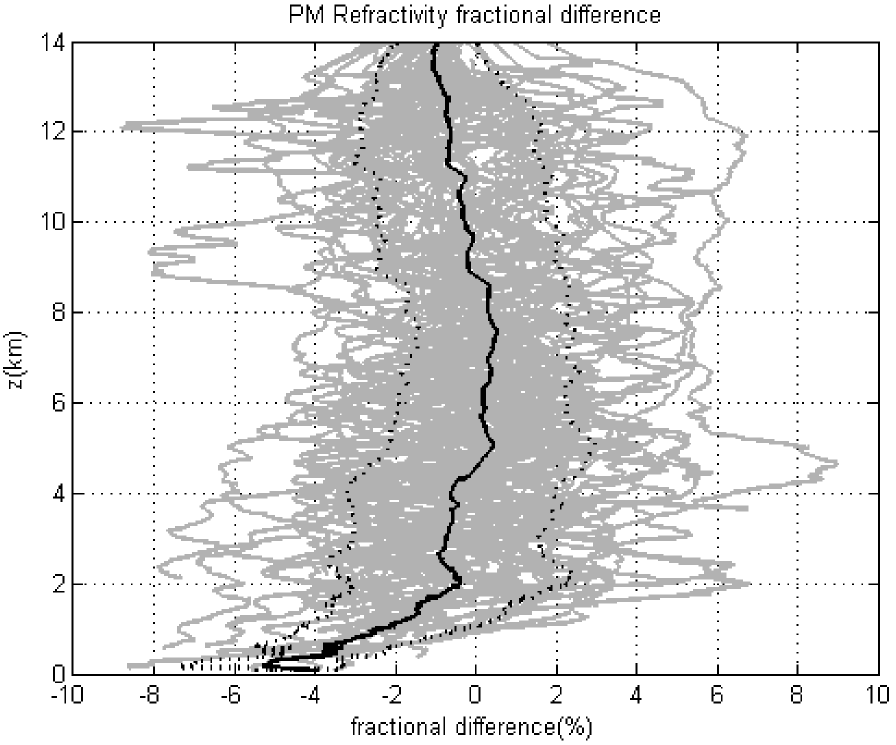

(b)

Figure 4.7. Same as Figure 4.6 but all 5 research flights are shown in the same figure. In average the results by using PM can maintain 1% error above 2 km.

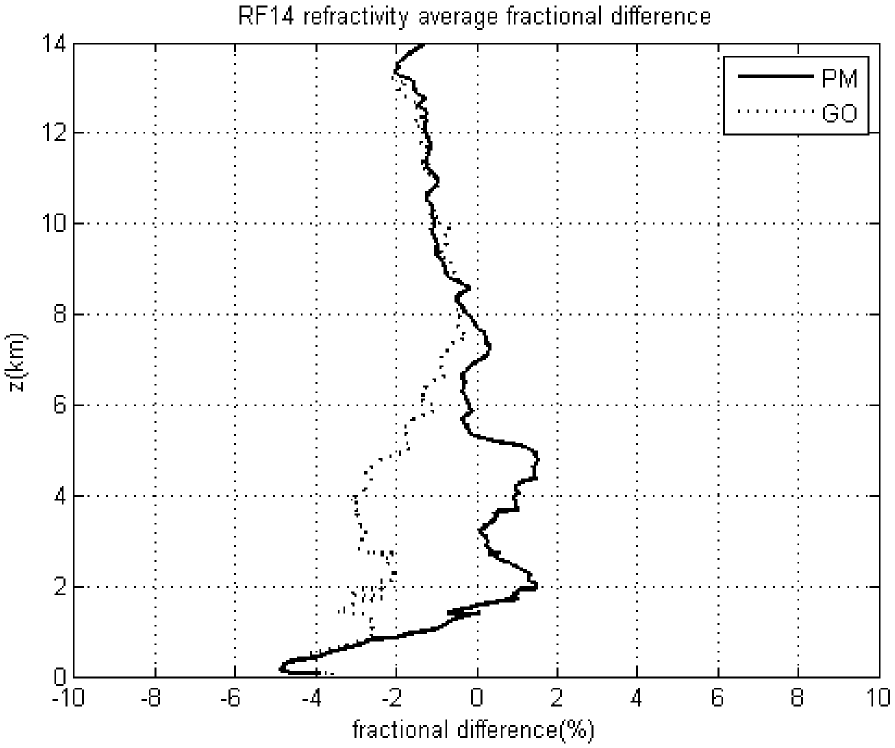
RF14 refractivity average fractional difference
PM
GO
z(km)
fractional difference(%)
0
2
4
6
8
10
12
14
-10
-8
-6
-4
-2
0
2
4
6
8
10

(a)

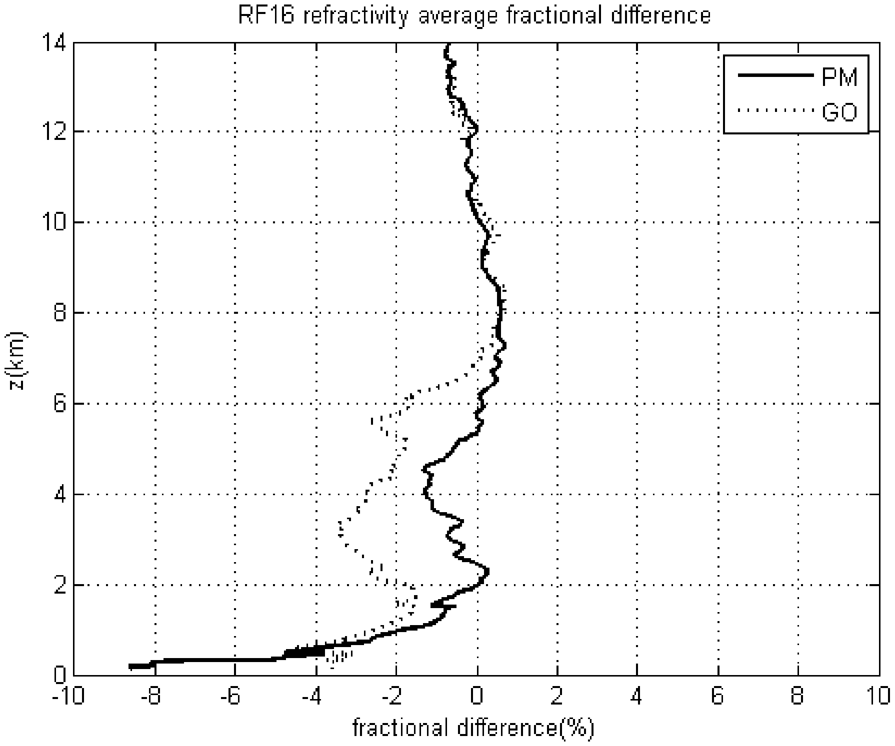
RF16 refractivity average fractional difference
PM
GO
z(km)
fractional difference(%)
0
2
4
6
8
10
12
14
-10
-8
-6
-4
-2
0
2
4
6
8
10

(b)

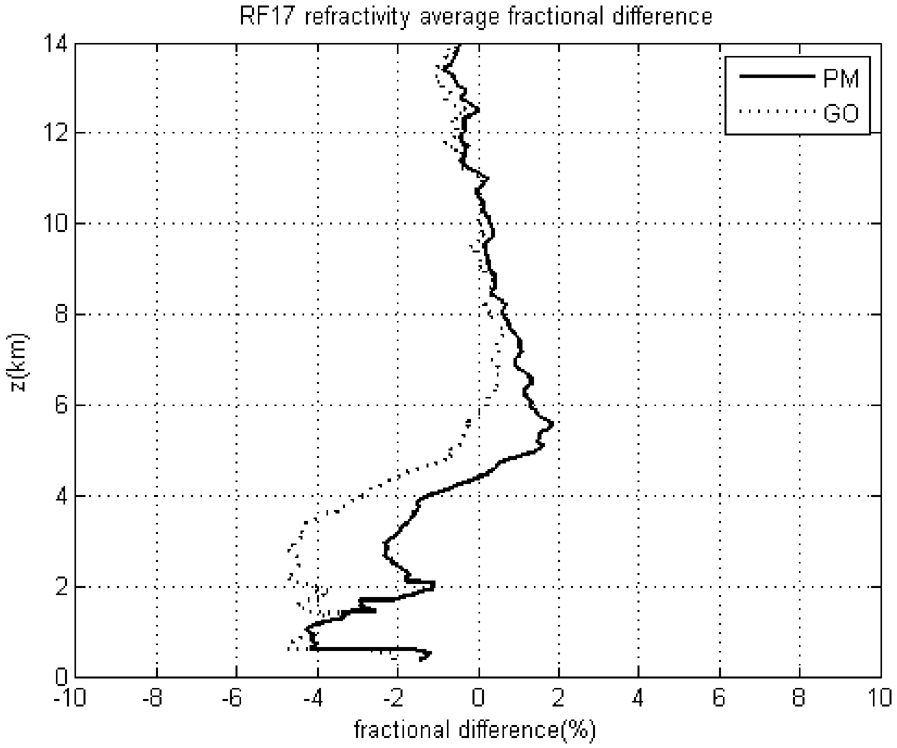
RF17 refractivity average fractional difference
z(km)
fractional difference(%)
PM
GO
0
2
4
6
8
10
12
14
-10
-8
-6
-4
-2
0
2
4
6
8
10

(c)

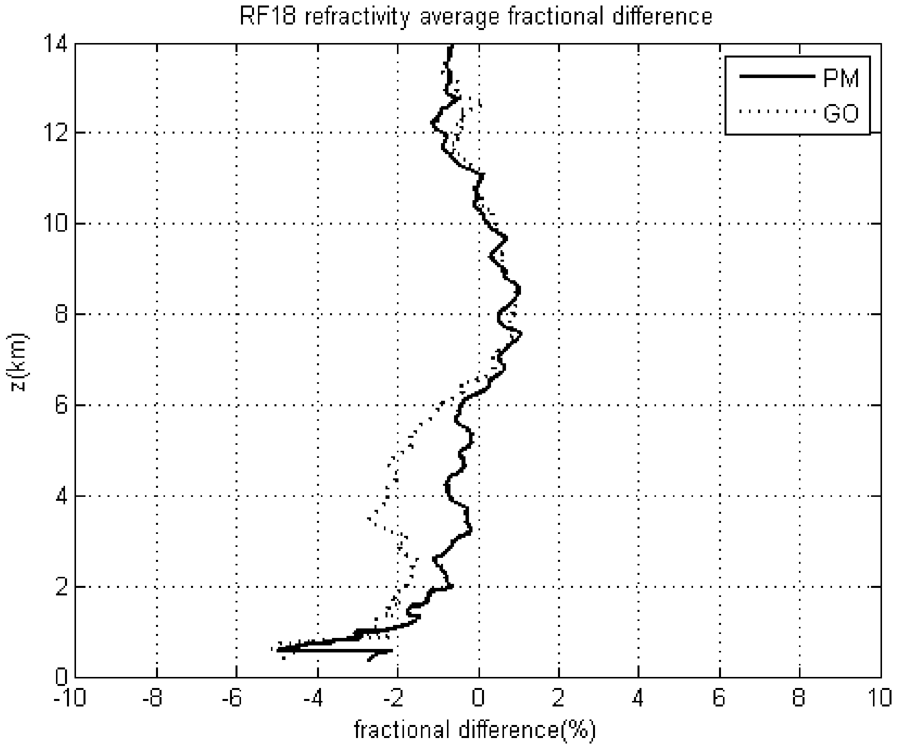
RF18 refractivity average fractional difference
z(km)
fractional difference(%)
PM
GO
0
2
4
6
8
10
12
14
-10
-8
-6
-4
-2
0
2
4
6
8
10

(d)

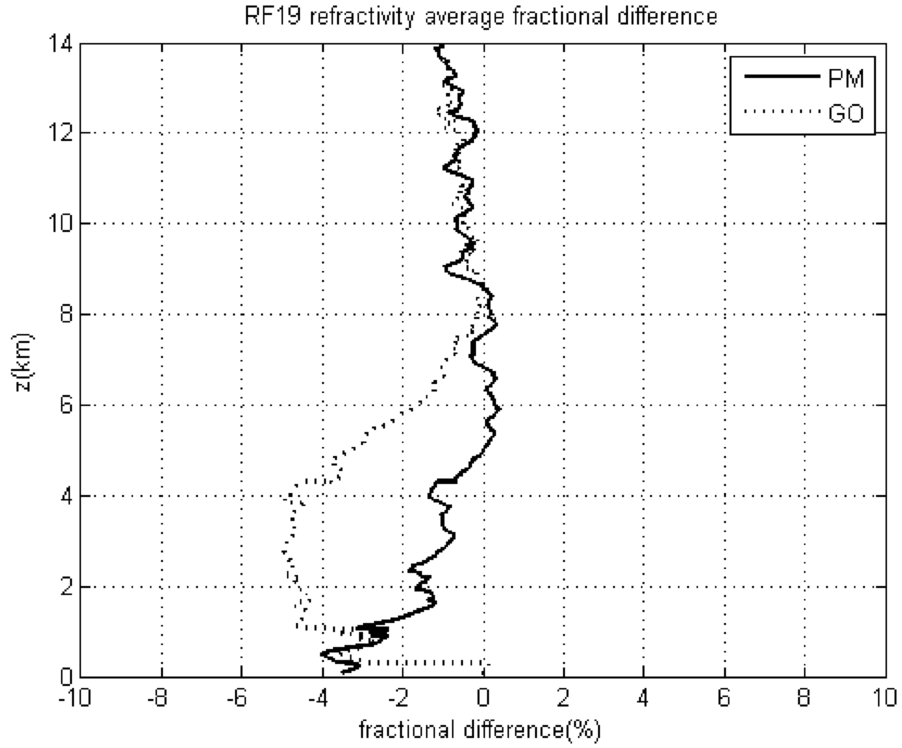

(e)

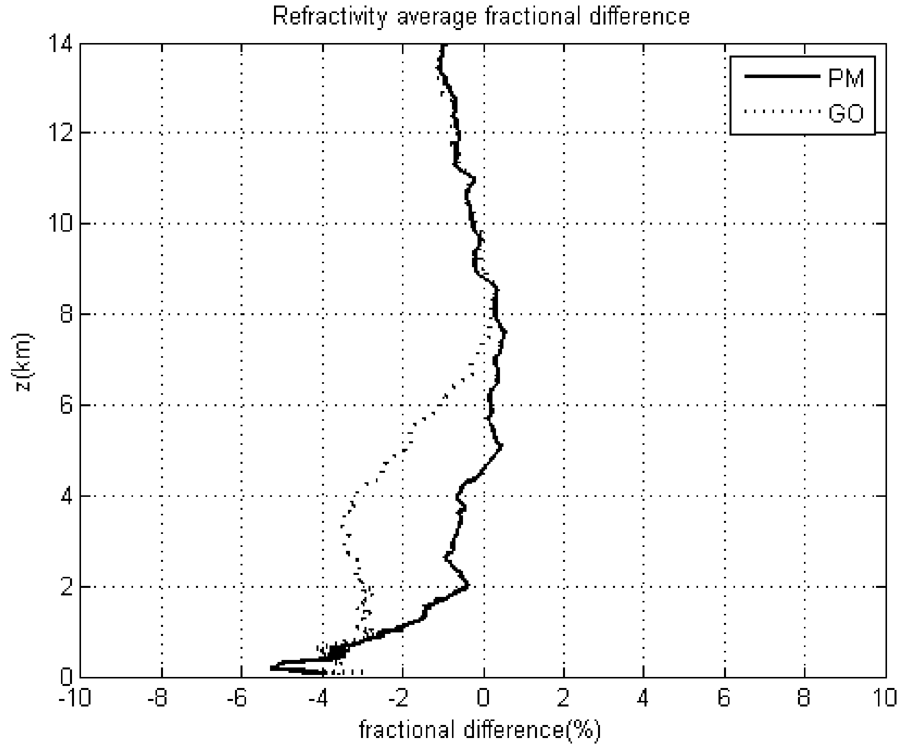

(f)

Figure 4.8. Average fractional difference for (a)RF14 (b)RF16 (c)RF17 (d)RF18 (e)RF19 (f)all research flights with PM and GO. The negative bias when using GO between 2 to 8 km is reduced by 2 %.

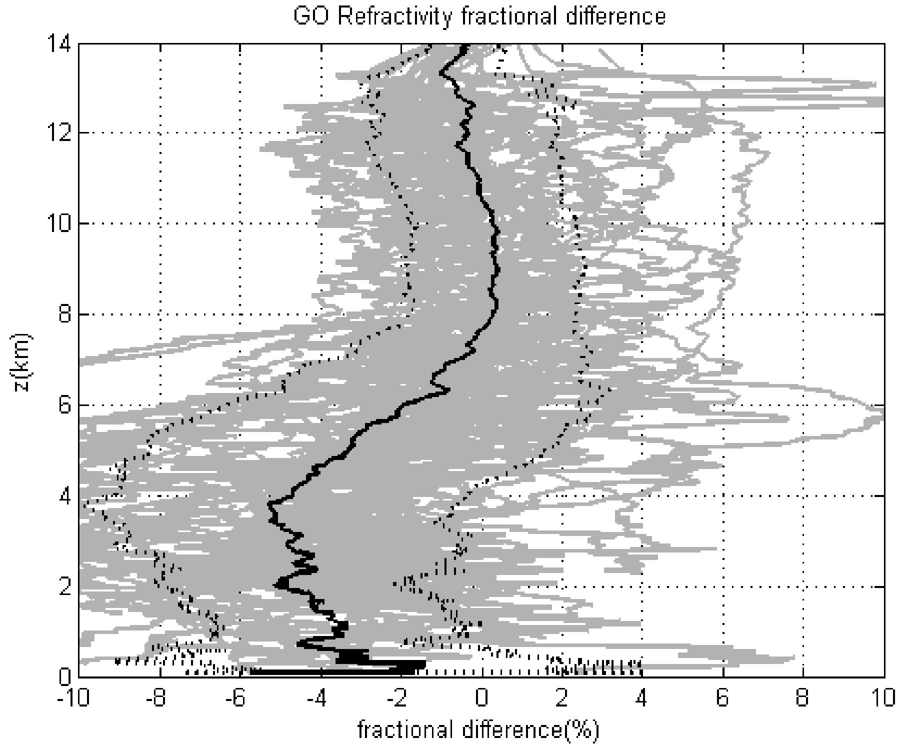
GO Refractivity fractional difference
z(km)
fractional difference(%)
0
2
4
6
8
10
12
14
-10
-8
-6
-4
-2
0
2
4
6
8
10

(a)

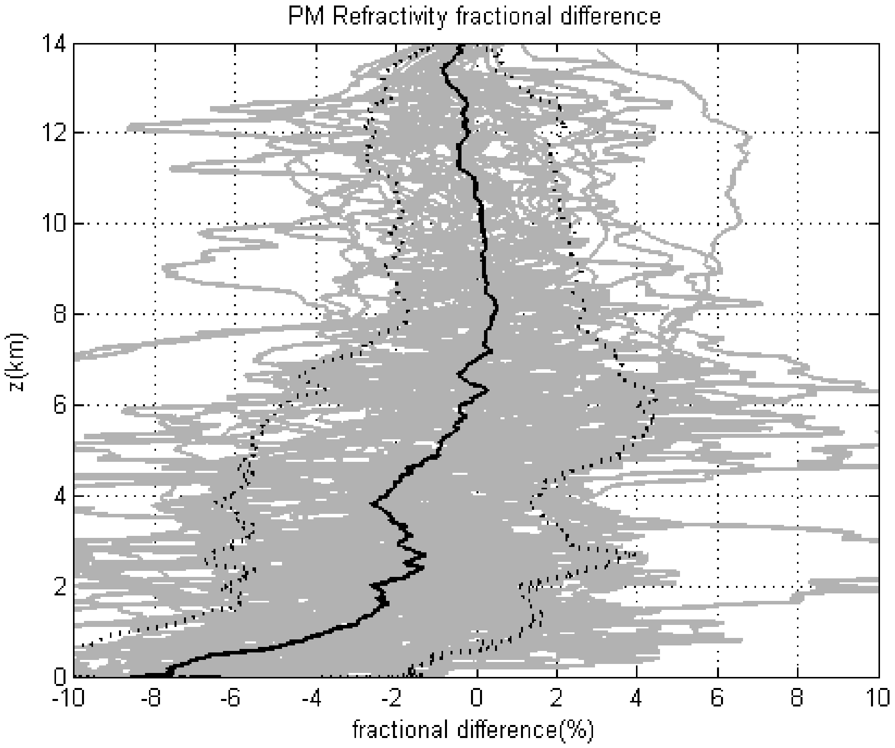
PM Refractivity fractional difference
z(km)
fractional difference(%)
0
2
4
6
8
10
12
14
-10
-8
-6
-4
-2
0
2
4
6
8
10

(b)

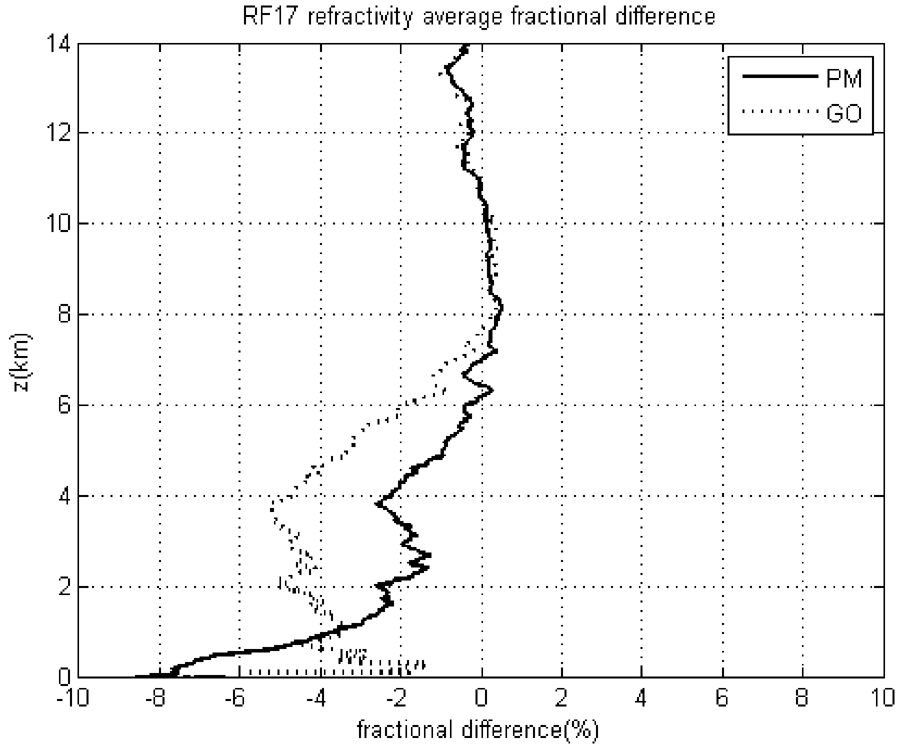

(c)

Figure 4.9. Same as Figure 4.7 and Figure 4.8 but using the dropsonde measurements as the reference refractivity profile. Only 44 qualified cases are compared (see texts). 2% fractional difference improvement can still be observed when compared to the dropsonde data.

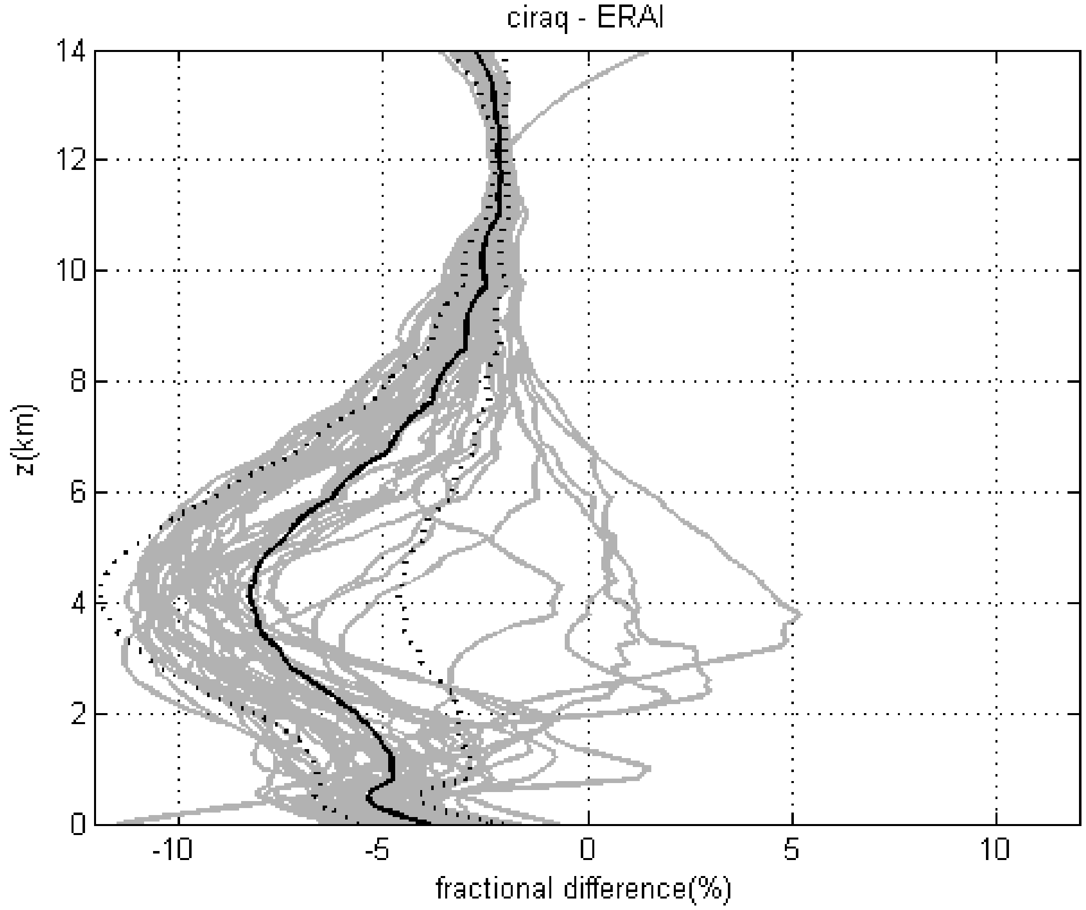

Figure 4.10. The fractional difference of the climatological model CIRAQ compared to the ERA-I model for each ARO case from RF16 to RF19. The −5% bias below 2 km is the can cause large negative bias when the received residual phase is randomly distributed.

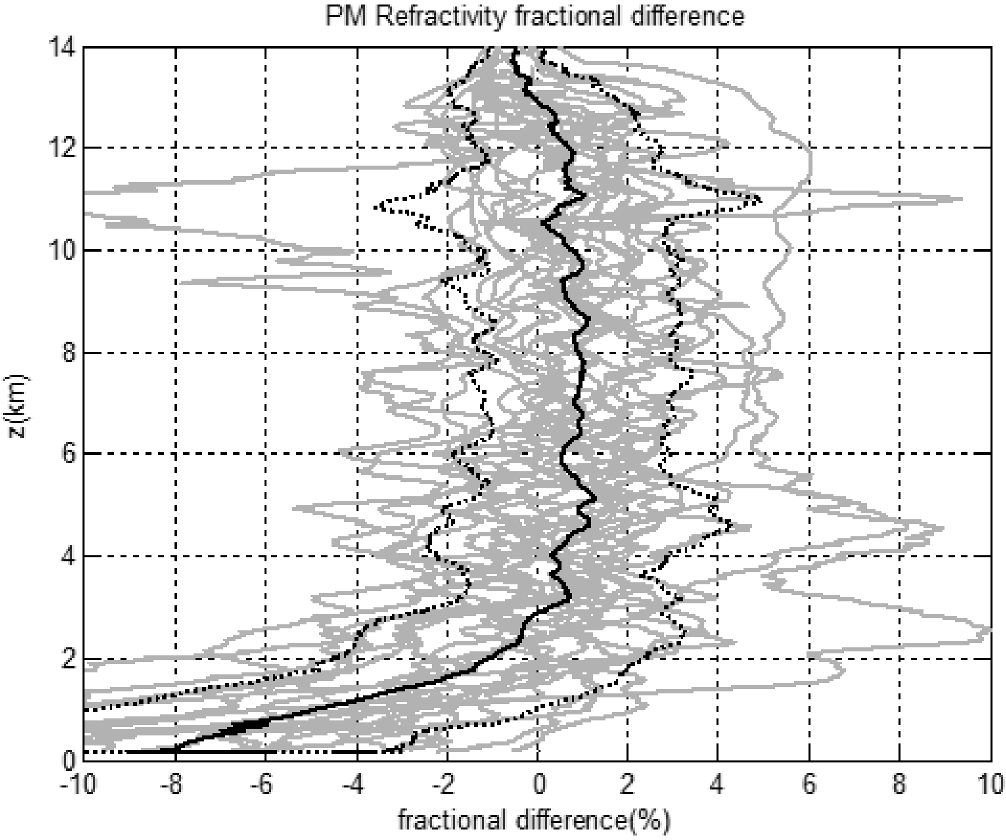

(a)

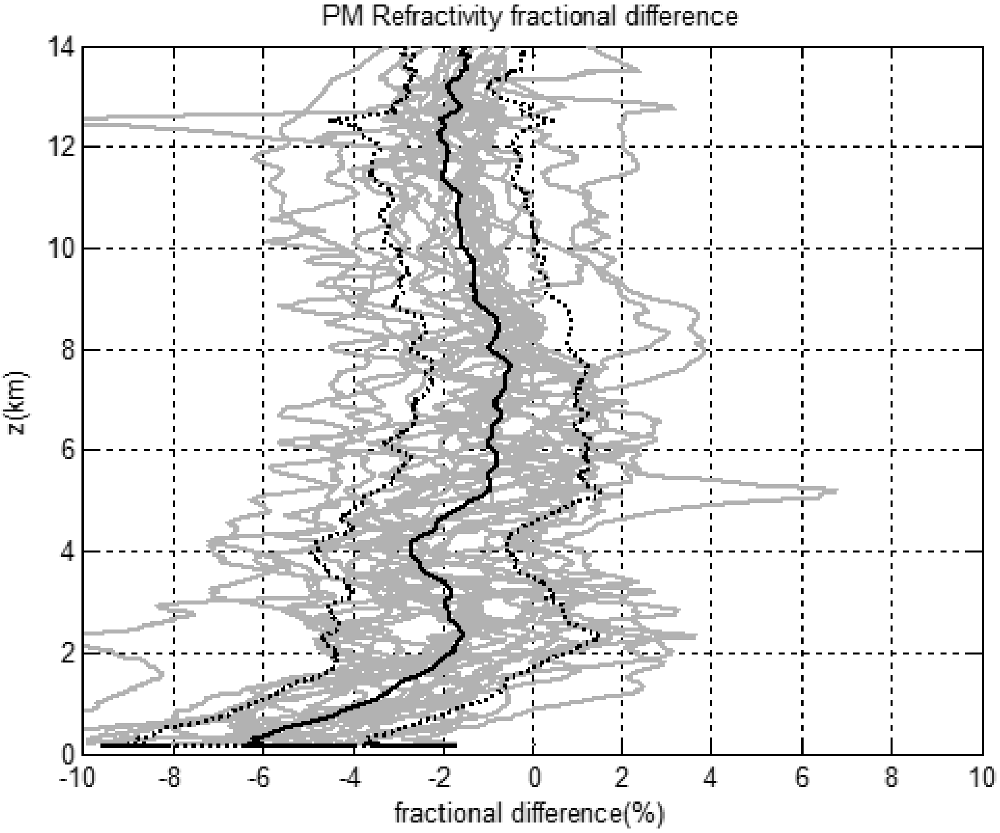

(b)

Figure 4.11. Refractivity retrieval results when setting and rising cases are separated. ARO PM method is used in both subfigures.

5. Summary

The airborne GPS RO technique is a valuable remote sensing technique which is able to use higher regional measurement density to sample localized transient events, and thus could become an appropriate complementary of spaceborne GPS RO. In this thesis the design of an airborne OL tracking software receiver for post-processing are presented and an error model relating SNR to signal phase variance has been developed to derive a model for the cumulative effect of phase unwrapping error. To reduce the negative bias caused by the accumulated unwrapping error, the combination of climatological model and the ray tracing program is utilized to provide more accurate phase model and enhance the SNR at lower heights. Large amount of unwrapping error in excess phase can thus be removed by reducing the number of unwrapping and the unwrapping error rate. However, the antenna design was found to be a limiting feature of the GISMOS implementation, producing measurements with SNR about 9-14 dB below COSMIC profiles collected in the same area. Therefore, for future flight mission the antenna gain pattern and beam orientation should also be considered to improve the likelihood of high-SNR observations. An antenna design with a wider azimuthal beam width, at the expense of a narrower beam width in the vertical direction or electronic beam-steering, can also enhance the ARO retrieval performance along with the ability to extract useful measurements in the lowest part of the troposphere.

In addition to the unwrapping error, the effect of multipath at lower altitude may cause fluctuation in SNR that also contribute to the negative bias in retrieval results and downgrades the applicability of the ARO data. We adapts the PM method, which using MSP for multi-subsignal detection, to the airborne platform to distinguish different subsignals arriving at the same time and untangle the multipath of the GPS RO signal due to complicated structure of moisture variation. The using of radio holographic method can greatly improve the bending angle calculation and decrease the refractivity retrieval negative bias from -3% fractional difference to less than -1% in average of 59 cases between 2 and 8 km height while retaining 2% standard deviation. For future work the negative bias using PM below 2 km which might caused by higher cut-off height could be verified and eradicated by extrapolate the climatological modeled phase to extent the cut-off height. The refractivity retrieval bias observed in rising and setting case should also be further investigated in the future studies.

REFERENCES

REFERENCES

[1] T. P. Yunck, L. Chao-Han, and R. Ware. A history of GPS sounding. *Terr. Atm. Ocean. Sci.*, 11(1):1–20, 2000.

[2] Gunnar Fjeldbo, Arvydas J. Kliore, and Von R. Eshleman. The neutral atmosphere of Venus as studied with the Mariner V radio occultation experiments. *The Astronomical journal*, 76(2), 1971.

[3] E.R. Kursinski, G.A. Hajj, K.R. Hardy, J.T. Schofield, and R. Linfield. Observing earth's atmosphere with radio occultation measurements. *J. Geoph. Res.*, 102(23):23.429–23.465, 1997.

[4] R. Ware, C. Rocken, F. Solheim, M. Exner, W. Schreiner, R. Anthes, D. Feng, B. Herman, M. Gorbunov, S. Sokolovskiy, et al. Gps sounding of the atmosphere from low earth orbit: Preliminary results. *Bulletin of the American Meteorological Society*, 77(1):19–40, 1996.

[5] E. R. Kursinski, G. A. Hajj, W. I. Bertiger, S. S. Leroy, T. K. Meehan, L. J. Romans, J. T. Schofield, D. J. McCleese, W. G. Melbourne, C. L. Thornton, T. P. Yunck, J. R. Eyre, and R. N. Nagatani. Initial results of radio occultation observations of earths atmosphere using the global positioning system. *Science*, 102(271):1107–1110, 1996.

[6] A. D. Collard and S. B. Healy. The combined impact of future space-based atmospheric sounding instruments on numerical weather prediction analysis fields: A simulation study. *Quarterly Journal of Royal Meteorological Society*, 129:2741–2760, 2003.

[7] M. P. Rennie. The impact of GPS radio occultation assimilation at the met office. *Quarterly Journal of Royal Meteorological Society*, 136:116–131, 2010.

[8] J. Wickert, T. Schmidt, C. Marquardt, C. Reigber, K. H. Neumayer, G. Beyerle, R. Galas, and L. Grunwaldt. GPS radio occultation with champ: first results and status of experiment. *Proc. of IAG*, 124(1):273–278, 2001.

[9] C.O. Ao, TK Meehan, GA Hajj, AJ Mannucci, and G. Beyerle. Lower troposphere refractivity bias in GPS occultation retrievals. *J. Geophys. Res*, 108(D18):4577, 2003.

[10] R. A. Anthes, P. A. Bernhardt, Y. Chen, L. Cucurull, K. F. Dymond, D. Ector, S. B. Healy, S. P. Ho, D. C. Hunt, Y. H. Kuo, H. Liu, K. Manning, C. McCormick, T. K. Meehan, W. J. Randel, C. Rocken, W. S. Schreiner, S. V. Sokolovskiy, S. Syndergaard, D. C. Thompson, K. E. Trenberth, T. K. Wee, N. L. Yen, and Z. Zeng. The COSMIC/FORMOSAT-3 mission: Early results. *Bulletin of the American Meteorological Society*, 89(3):313–333, 2008.

[11] *COSMIC Data Analysis and Archive Center.*

[12] A. von Engeln. GRAS radio occultation measurements onboard METOP. In *Fourth FORMOSAT-3/COSMIC Data Users Workshop, 27-29 October 2009*, Boulder, CO, 2009.

[13] K. Cook, Chen-Joe Fong, M.J. Wenkel, P. Wilczynski, N. Yen, and G.S. Chang. FORMOSAT-7/COSMIC-2 GNSS radio occultation constellation mission for global weather monitoring. In *Aerospace Conference, 2013 IEEE*, Big Sky, MT, 2013.

[14] S. B. Healy, J. Haase, and O. Lesne. Abel transform inversion of radio occultation measurements made with a receiver inside the earths atmosphere. *Annales Geophysicae*, 2002.

[15] C. Zuffada, G. A. Hajj, and E. R. Kursinski. A novel approach to atmospheric profiling with a mountain-based or airborne receiver. *J. Geophys. Res*, (104):2443524447, 1999.

[16] T.D. Lulich, J. L. Garrison, J.S. Haase, Yu-Ming Yang, J. Voo, F. Xie, and P. Muradyan. Open loop tracking of radio occultation signals from an airborne platform. In *ION GNSS 2010*, Portland, Oregon, 2010.

[17] P. Muradyan. Profiling the atmosphere with the airborne gps radio occultation technique using open-loop tracking. Master's thesis, Purdue University, 2012.

[18] J. S. Haase, B.J. Murphy, P. Muradyan, F.G. Nievinski, K.M. Larson, J. L. Garrison, and K.-N. Wang. First results from an airborne gps radio occultation system for atmospheric profiling. *Geophysical Research Letters*, 41:1759–1765, 2014.

[19] G. Beyerle, J. Wickert, T. Schmidt, and C. Reigber. Atmospheric sounding by global navigation satellite system radio occultation: An analysis of the negative refractivity bias using champ observations. *Journal of Geophysical Research*, 109(D01106), 2004.

[20] S.V. Sokolovskiy. Effect of superrefraction on inversions of radio occultation signals in the lower troposphere. *Radio Science*, 38:483–498, 2003.

[21] F. Xie, D. L. Wu, C. O. Ao, E. R. Kursinski, A. J. Mannucci, and S. Syndergaard. Super-refraction effects on gps radio occultation refractivity in marine boundary layers. *Geophysical Research Letters*, 37, 2010.

[22] K.-N. Wang, J. L. Garrison, U. Acikoz, J.S. Haase, B. J. Murphy, P. Muradyan, and T. Lulich. Open-loop tracking of rising and setting GPS radio-occultation signals from an airborne platform: signal model and error analysis. *submitted to Transactions on Geoscience and Remote Sensing*, 2015.

[23] F. Xie, J.S. Haase, and S. Syndergaard. Profiling the atmosphere using the airborne GPS radio occultation technique: A sensitivity study. *Trans. IEEE Geosci. and Remote Sens.*, 46(11):3424–3435, 2008.

[24] B. J. Murphy, J.S. Haase, P. Muradyan, J. L. Garrison, and K.-N. Wang. Airborne GPS radio occultation refractivity profiles observed in tropical storm environments. *Journal of Geophysical Research*, 120:1690–1709, 2015.

[25] A.S. Jensen, M.S. Lohmann, H.H. Benzon, and A.S. Nielsen. Full spectrum inversion of radio occultation signals. *Radio Science*, 38(3):1040, 2003.

[26] S. Sokolovskiy, C. Rocken, W. Schreiner, and D. Hunt. On the uncertainty of radio occultation inversions in the lower troposphere. *J. Geophys. Res.*, 115(D22):D22111, 2010.

[27] S.V. Sokolovskiy. Modeling and inverting radio occultation signals in the moist troposphere. *Radio Science*, 36(3):441–458, 2001.

[28] International GNSS Service.

[29] S.V. Sokolovskiy. Tracking tropospheric radio occultation signals from low earth orbit. *Radio Science*, 36(3):483–498, 2001.

[30] CO Ao, GA Hajj, TK Meehan, D. Dong, BA Iijima, AJ Mannucci, and ER Kursinski. Rising and setting GPS occultations by use of open-loop tracking. *J. Geophys. Res*, 114, 2009.

[31] G. Beyerle and K. Hocke. Observation and simulation of direct and reflected GPS signals in radio occultation experiments. *Geophysical Research Letters*, 28(9):1895–1898, 2001.

[32] G.A. Hajj, E.R. Kursinski, L.J. Romans, W.I. Bertiger, and S.S. Leroy. A technical description of atmospheric sounding by gps occultation. *Journal of Atmospheric and Solar-Terrestrial Physics*, 64(2002), 2002.

[33] V. Vorobev and T. Krasilnikova. Estimation of the accuracy of the atmospheric refractive index recovery from doppler shift measurements at frequencies used in the NAVSTAR system. *Physics of the Atmosphere and Ocean*, 29(5), 1994.

[34] M. Born and E. Wolf. *Principles of Optics: Electromagnetic Theory of Propagation, Interference and Diffraction of Light*. Pergamon Press, 1964.

[35] S. Syndergaard. Modeling the impact of Earth's oblateness on the retrieval of temperature and pressure profiles from limb sounding. *J. Atmos. Solar-Terr. Phys.*, 60(2):171–180, 1998.

[36] O. Lesne, J. Haase, G. Kirchengast, J. Ramsauer, and W. Poetzi. Sensitivity analysis for airborne sounding of the troposphere by gnss radio occultation. *Phys. Chem. Earth*, 27(4-5), 2002.

[37] Ulvi Acikoz. Open loop tracking of rising GPS radio occultation signals. Master's thesis, Purdue University, 2011.

[38] S. Sokolovskiy, C. Rocken, W. Schreiner, D. Hunt, and J. Johnson. Postprocessing of l1 gps radio occultation signals recorded in open-loop mode. *Radio Science*, 44(2), 2009.

[39] G. Beyerle, T. Schmidt, J. Wickert, S. Heise, M. Rothacher, G. Konig-Langlo, and K. B. Lauritsen. Observations and simulations of receiver-induced refractivity biases in gps radio occultation. *Journal Of Geophysical Research-Atmospheres*, 111(D12), 2006. D12101.

[40] G. Heckler and J. L. Garrison. Architecture of a reconfigurable software receiver. pages 947–955, 2004.

[41] P. Muradyan, J.S. Haase, F. Xie, J. L. Garrison, T. Lulich, and J. Voo. GPS/INS navigation precision and its effect on airborne radio occultation retrieval accuracy. *GPS Solutions*, 10.1007/s10291-010-0183-7, 2010.

[42] M. Schenewerk. A brief review of basic GPS orbit interpolation strategies. *GPS Solutions*, 6:265267, 2003.

[43] Global positioning system direcorate system engineering and integration interface specification IS-GPS-200. Technical report, Navstar GPS Space Segment/Navigation User Interfaces, Sep 2012.

[44] Pratap Misra and Per Enge. *Global Positioning System-Signals, Measurements, and Performance, 2nd Edition.* Ganga-Jamuna Press, 2006.

[45] COSMIC bit grabber network.

[46] R. N. McDonough and A. C. Whalen. *Detection of Signals in Noise, 2nd Edition.* Academic Press, 1995.

[47] Athanasios Papoulis and S. Unnikrishna Pillai. *Probability, Random Variables and Stochastic Processes.* Mc Graw Hill, 2002.

[48] P. Hoeq, A. Hauchecorne, G. Kirchengast, S. Syndergaard, B. Belloul, R. Leitinger, and W. Rothleitner. Derivation of atmospheric properties using a radio occultation technique. Technical report, Danish Meteorological Institute, Copenhagen, Denmark.

[49] JL Garrison, M. Walker, J. Haase, T. Lulich, F. Xie, BD Ventre, MH Boehme, B. Wilmhoff, and SJ Katzberg. Development and testing of the GISMOS instrument. In *IEEE International Geoscience and Remote Sensing Symposium, 2007. IGARSS 2007*, pages 5105–5108, 2007.

[50] Era-interim.

[51] Oliver Montenbruck and Remco Kroes. In-flight performance analysis of the CHAMP blackjack GPS receiver. *GPS Solutions*, 2003.

[52] Oliver Montenbruck, Miquel Garcia-Fernandez, and Jacob Williams. Performance comparison of semicodeless GPS receivers for LEO satellites. *GPS Solutions*, 2006.

[53] C. Rocken, Y.-H. Kuo, D. Ectorand, and W. S. Schreiner. Developing the COSMIC system at UCAR. Technical report, University Corporation for Atmospheric Research.

[54] H. Aliakbarian, E. Van der Westhuizen, R. Wiid, V. Volski, R. Wolhuter, G. A. E. Vandenbosch, and P. Coppin. A digitally beam-steerable antenna array system for positioning-based tracking applications. *IEEE Antennas and Propagation Magazine*, 55:35–49, 2014.

[55] M. E. Gorbunov and K. B. Lauritsen. Analysis of wave fields by Fourier integral operators and their application for radio occultations. *Radio Sci.*, 39, 2004.

[56] M. Gorbunov and A. Gurvich. Microlab-1 experiment: Multipath effects in the lower troposphere. *J. Geophys. Res.*, 103:13819–13826, 1998.

[57] ME Gorbunov. Canonical transform method for processing radio occultation data in the lower troposphere. *Radio Science*, 37(5):1076, 2002.

[58] A. S. Jensen, M. S. Lohmann, A. S. Nielsen, and H.-H. Benzon. Geometrical optics phase matching of radio occultation signals. *Radio Science*, 39, 2004.

[59] G. Kirchengast, J. Hafner, and W. Poetzi. The cira86aq_uog model: An extension of the cira-86 monthly tables including humidity tables and a fortran95 global moist air climatology mode. Technical report, Eur. Space Agency, Paris, France.

[60] M. E. Gorbunov, A. S. Gurvich, and A. V. Shmakov. Back-propagation and radioholographic methods for investigation of sporadic ionospheric e-layers from microlab-1 data. *International Journal of Remote Sensing*, 23(4), 2002.

[61] Kai Borre, Dennis M. Akos, Nicolaj Bertelsen, Peter Rinder, and Soren Holdt Jensen. *A Software-Defined GPS and Galileo Receiver (A Single-Frequency Approach)*. Birkhauser, 2007.

APPENDICES

A. Radio holographic method

As stated in introduction, radio holographic methods are designed for multipath problem encountered in occultation of low atmosphere. We will have literature review in the first section and show the way we apply FSI on airborne platform simulation data in the following section. Some simulation results and future research direction will also be provided and discussed.

A.1 Literature review

Some algorithms have been developed in last 15 years to cope with multipath issue in spaceborne GPS RO. Most of them can be categorized into 4 main approaches, and we will review them in the following sub-sections.

A.1.1 Back propagation(BP)

BP algorithm is based on the diffraction theory. By this theory we can describe the electromagnetic field in the vacuum with Helmholtz equation:

$$\Delta u + k^2 u = 0 \tag{A.1}$$

where u is the complex amplitude of electromagnetic field. The solution of the external boundary problem for the Helmholtz equation described in [60] can be used to calculate the complex field with a given closed curve and initial value. Therefore, we can calculate the electromagnetic field backward in a vertical plane of RO by using the measurements of signal amplitude and phase (initial value) on a satellite orbit(closed curve).

$$u\left(x\right)=\left(\frac{k}{2\pi}\right)^{1/2}\int_{S}u_{0}\left(y\right)cos\varphi_{xy}\frac{exp\left(-ik\left|x-y\right|+i\pi/4\right)}{\left|x-y\right|^{1/2}}dS_{y} \tag{A.2}$$

The idea of the back propagation is that we can choose the location of this vertical plane where the multipath effect has not occurred. Since the propagation in the vacuum can be seen as the straight line continuation of rays the impact parameter and bending angle characteristic are preserved. In this way we can avoid the multipath and acquire unaffected original impact parameter and bending angle values. BP can provide very high resolution but the finding position of the auxiliary vertical plane is difficult and the computation complexity is high.

A.1.2 Sliding spectral(SS)

Proposed by Sokolovskiy [27] the sliding spectral is the method uses spectral analysis of the received signal with a series of windows on the receiver trajectory. If we consider a signal received in a window of trajectory Δy centered at y_c, the Fourier transform can be calculated as:

$$c_{m}=\frac{1}{2\pi}\int_{y_c-\Delta y/2}^{y_c+\Delta y/2}u\left(y\right)exp\left(-2\pi imy/\Delta y\right)dy \tag{A.3}$$

By using the Fourier transform the signal entered into the window can be divided into different spatial frequency components. Each of them can be taken as a ray path with distinctive impact parameter a_m and bending angleα_m.

$$a_{m}=sin^{-1}\left(\chi_{m}c/f\right) \tag{A.4}$$

$$\alpha_{m}=\left(R_{E}+y_{c}+ltan\left(a_{m}\right)\right)cos\left(a_{m}\right) \tag{A.5}$$

where χ_m is the spatial frequency and l is the distance between the center of earth and observation trajectory. Then by sliding the window along the trajectory we can get the c_j, a_j, and α_j in the whole trajectory. After sorting the data with impact parameter a_j we can apply sliding window averaging the bending angle and impact parameter with the weighting factor $|c_j|^2$ By doing this the function of bending angle with respect to the impact parameter can be acquired directly with analyzing received signal spectrum instead of propagation. The disadvantage of SS is that the resolution is depends on the sliding window size.

A.1.3 Canonical transform(CT)

the CT method utilizes the characteristic that bending angle of the rays is a single value function of impact parameter [57]. Therefore, the received signal can be analyzed under phase space with the transformation to canonical coordinates. To do this, we first have to use BP method in previous section to propagate the wave from observation plane to a the vertical plane. Note that no tuning parameter is needed to choose plane location and we can use the fixed location for every case even the refractivity structure is complicated. Then the wave equation can be transformed to spatial frequency domain by Fourier transform:

$$\tilde{u}\left(\eta\right) = \int e^{-iky\eta} u\left(y\right) dy \tag{A.6}$$

With the signal described by (y, η) we then apply the CT to transform the signal to a new canonical coordinate (p, ξ):

$$\begin{aligned} u\left(p\right) &= \frac{k}{2\pi} \int \left(1-\eta^2\right)^{-1/4} \times e^{ik\left[psin^{-1}\eta\right]} \tilde{u}\left(\eta\right) d\eta \\ &= A\left(p\right) e^{ik\Psi(p)} \end{aligned} \tag{A.7}$$

where p is the impact parameter. Then the momentum ξ can be calculated by MSP as:

$$\xi\left(p\right) = \frac{\partial \Psi(p)}{\partial p} \tag{A.8}$$

With the momentum we can use the Bouger's law to solve the bending angle. By these calculation the relationship of impact parameter and the bending angle can be acquired without doing differentiation of the excess phase. This method can provide high resolution compared to SS. The only drawback of this method is BP pre-processing is necessary in the beginning which is also the most computation-consuming part.

A.1.4 Full spectrum inversion(FSI)

As the way CT dealing the multipath problem with Fourier transform, the FSI use the same approach. If both the transmitter and receiver trajectory are circular, the doppler frequency of the wave field is proportional to the impact parameter of the ray path. By using the characteristic that $t(\omega)$ remains a single valued function in multipath region we can separate the ray path with different impact parameters received at the same time. To keep it single valued we need the assumption that each impact parameter (which means each doppler frequency) will occur only once.

To do this, firstly we consider a signal consists of narrow band subsignals:

$$V\left(t\right)=\sum_{p}Q_{p}\left(t\right)exp\left(i\varphi_{p}\left(t\right)\right) \tag{A.9}$$

where φ_p and Q_p are the phase and amplitude of the p-th subsignal respectively. Then can apply Fourier transform:

$$\hat{V}\left(\omega\right)=\sum_{p}\int_{0}^{T}Q_{p}\left(t'\right)exp\left[i\left(\varphi_{p}\left(t'\right)-\omega t'\right)\right]dt' \tag{A.10}$$

From the MSP method we can approximate equation (A.10) as:

$$\hat{V}\left(\omega\right)=\sqrt{\frac{2\pi i}{\frac{d^{2}\varphi_{q}}{dt^{2}}\left(t_{1}\right)}}Q_{q}\left(t_{1}\right)exp\left[i\left(\varphi_{q}\left(t_{1}\right)-\omega t_{1}\right)\right] \tag{A.11}$$

where t_1 is the arrival time of the corresponding frequency. As equation (A.11) suggested the signal can be divided with different instantaneous frequency components at different arrival time. The arrival time can be calculated by:

$$\frac{d}{d\omega}\left(\varphi_q\left(t_1\right)-\omega t_1\right)=-t_1 \tag{A.12}$$

With this equation we can calculate the instantaneous frequency and its corresponding arrival time at each time step or open angle step. In the paper [25] suggested that the interpolation of open angle instead of time will effectively decrease interference caused by radial accelerations. By using the geometry of transmitter and receiver we can find impact parameter by:

$$\frac{d\varphi_q}{d\theta}=ka+k\frac{dr_L}{d\theta}\sqrt{1-\left(\frac{a}{r_L}\right)^2}+k\frac{dr_G}{d\theta}\sqrt{1-\left(\frac{a}{r_G}\right)^2} \tag{A.13}$$

The by Bouger's law and the geometry we can acquire the bending angle α:

$$\alpha=\theta+\phi_G+\phi_L-\pi \tag{A.14}$$

In this way we can find the relationship of bending angle and impact parameter even in multipath region. The result can be taken as the input of inverse Abel transform for refractivity calculation.

A.2 RH simulation with airborne case

Since FSI doesn't have to implement BP in the beginning but with high resolution performance, we choose FSI for bending angle retrieval from airborne data. Firstly, we simulate an ideal trajectory case which both trajectories of GPS satellite and aircraft are circular with ROSAP ray-tracing program. We use exponential refractivity profile to simplify the model and generate a single ray environment, then the ray tracing program can provide us excess phase and amplitude. The results from equation (A.12) is shown in the figure A.1.

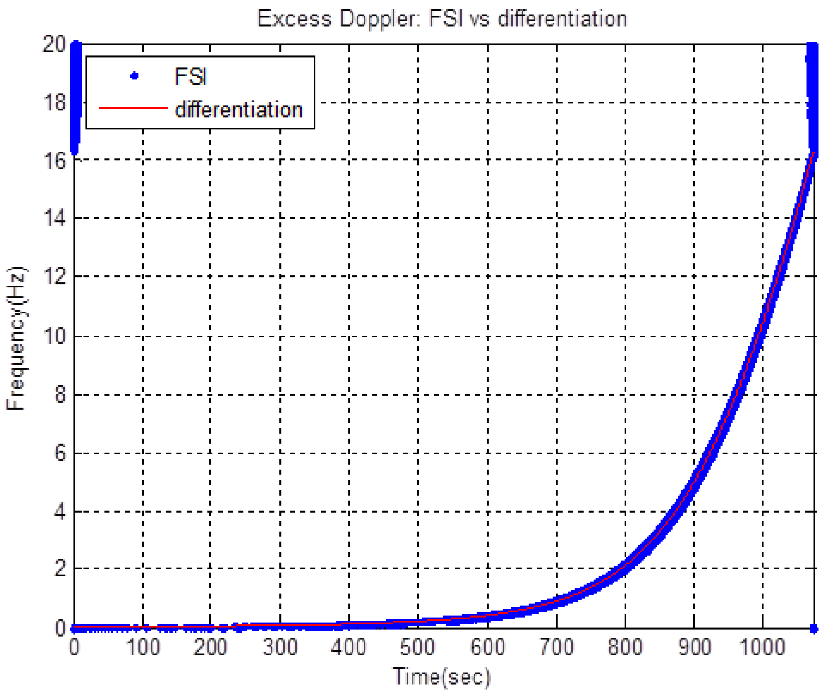

Figure A.1. The derivative of FFT phase. Blue dots are the FFT phase derivative result and the red line is the result from taking differentiation of the signal total phase directly.

As the figure A.1 shows, the FSI can successfully retrieve the relationship between instantaneous frequency and its corresponding arrival time. The results from these two methods are identical since we simulate only single ray area. Also because of the ideal trajectory there is no last two terms in equation(A.13). Then we can use the equation to calculate impact parameter and acquire its corresponding bending angle as shown in figure A.2. The results shows the FSI can calculate the bending angle profile correctly from the excess phase measurements.

To simulate the multipath region we used a complicated bending angle profile and its corresponding geometry for IFSI program to generate the excess phase and signal amplitude. As the previous case, we used the ideal trajectory to simplify the calculation. The FSI is again utilized to analyze the signal's instantaneous frequency and arrival time. The result is shown in figure A.3

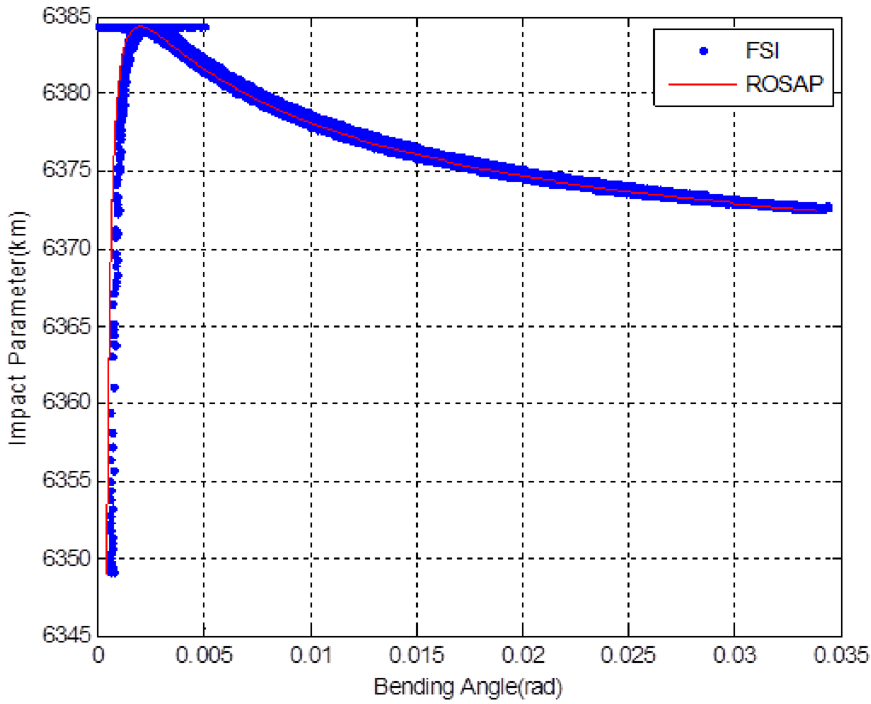

Figure A.2. The bending angle with respect to impact parameter calculated by FSI (blue dots) and the ROSAP program(red line)

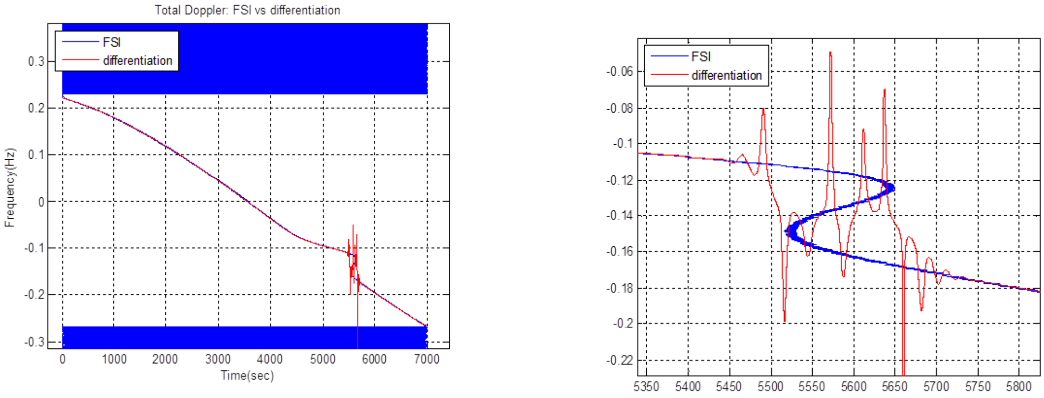

(a) zoom out

(b) zoom in

Figure A.3. The derivative of FFT phase. Blue dots are the FFT phase derivative result and the red line is the result from taking differentiation of the signal total phase directly.

In figure A.3, the red line is the result of taking direct differentiation of the signal phase and it shows very noisy behavior during the multipath region. It's obvious that this traditional method cannot deal with the complicated signal structure. In the other hand, the FSI can distinguish different frequencies from different signals and provide an unambiguous function of arrival time with respect to instantaneous frequency. This is an good example to demonstrate the advantage of the FSI method. Then the function of bending angle and its corresponding impact parameter can be calculated by equation(A.14) and the results are shown in figure A.4. As the figure shows the FSI can successfully retrieve the original bending angle profile even under multipath effects.

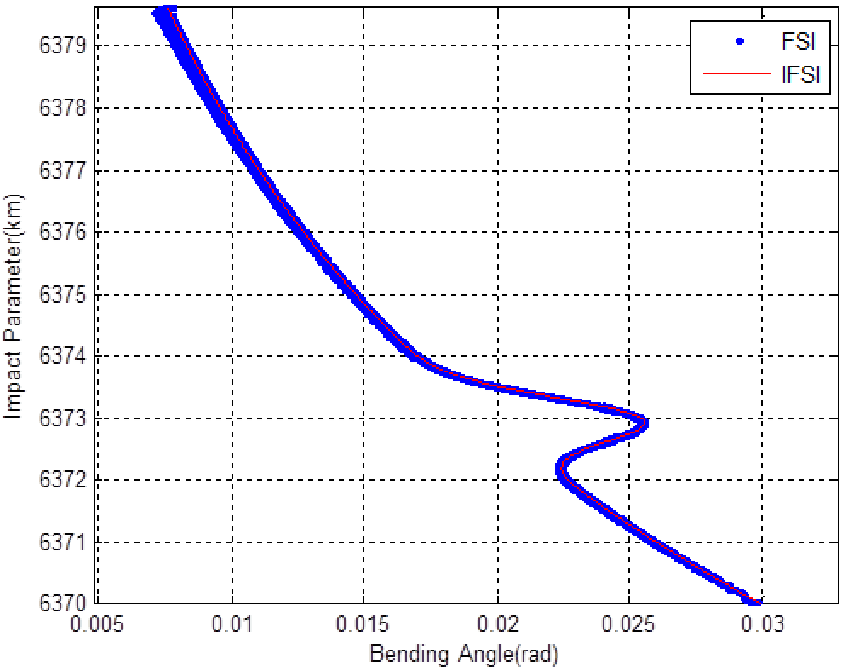

Figure A.4. The derivative of FFT phase in multipath region. Blue dots are the FFT phase derivative result and the red line is the result from taking differentiation of the signal total phase directly.

B. Purdue Software Receiver (PSR)

PSR is the GNSS software receiver developed by Purdue Navigation Lab. The receiver prototype was designed in C language by Heckler, G. [40], and the OL function were added by Ventre, B. G. [49]. The Doppler prediction module was refined by Lulich, T. [16], and the backward tracking feature was developed by Acikoz, U. [37]. In this research, the PSR is modified to become more streamlined, complete, and user friendly. The following are the introduction of the whole process and the procedure of executing each individual module.

B.1 Processing procedure

The flow chart of the latest version PSR is shown as Figure B.1.

As the figure shows, the latest PSR can be divided into 4 different modules, which can be individually handled by 4 separate C-shell scripts. The C-shell scripts, which can be controlled through the .inp files, will call C++ (while correlation included) or Matlab (correlation does not included) functions for specific purpose. These 4 modules will be discussed further in the following subsections.

B.1.1 psr_prep

<u>INPUT</u>:

- prep.inp
- raw GRS data

<u>OUTPUT</u>:

- Acq_CHx.txt

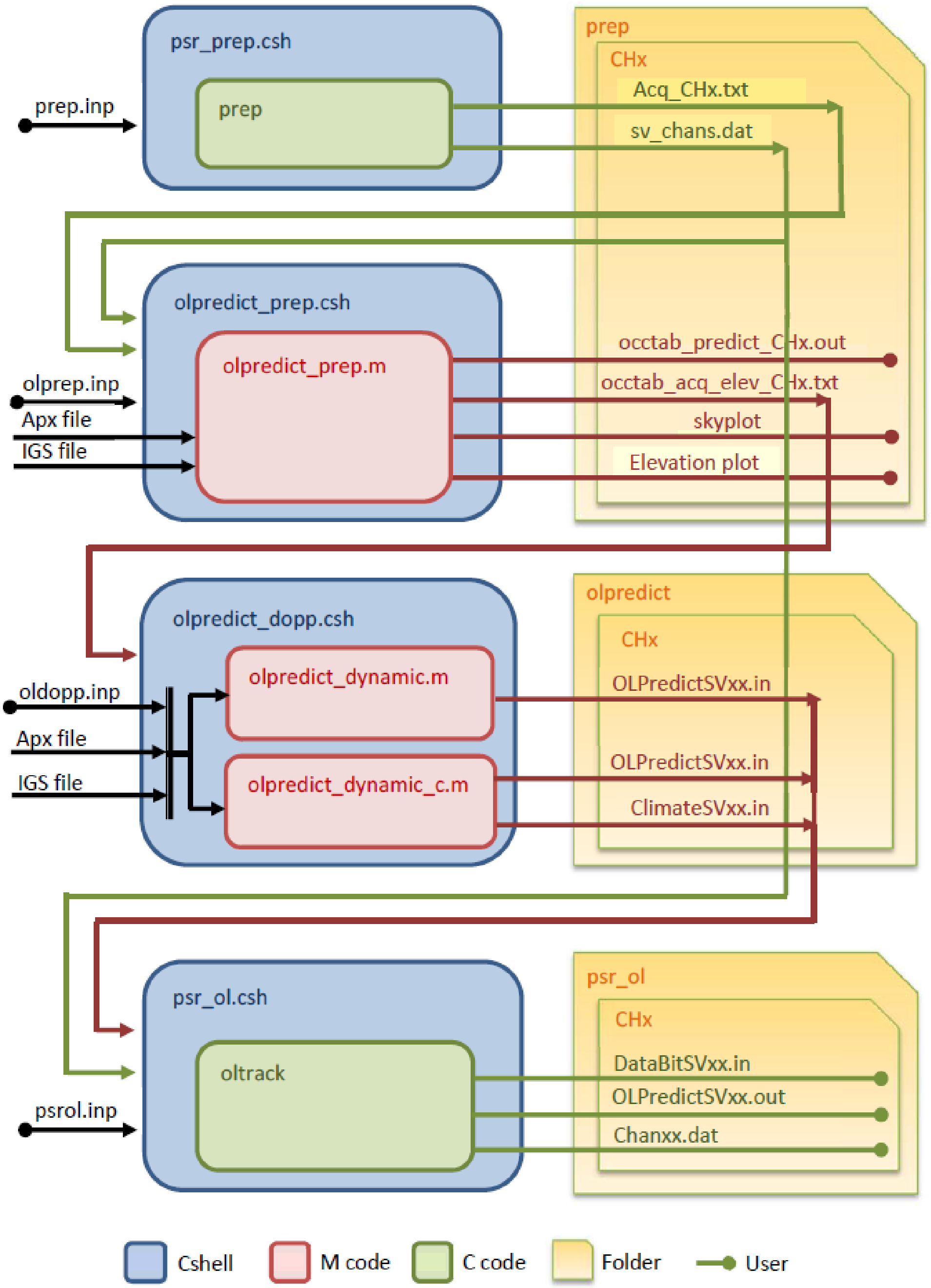

Figure B.1. The flow chart of PSR OL tracking process.

- sv_chans.dat

This module applies acquisition process on the raw GRS collected data. No other information (satellite orbit, flight trajectory, etc.) is used in this process because we want to determine the available PRN only by the data. The acquisition are applied on the first and the last 5 ms of each GRS file and search the available PRN, corresponding Doppler and code phase in forward and backward order. The result will be saved in two files which can be used in the next module.

B.1.2 olpredict_prep

INPUT:

- olprep.inp
- sv_chans.dat
- Applanix file
- IGS file

OUTPUT:

- occtab.out

This module "plans" which PRN to be processed within the given time frame and determine the beginning and ending time of each channel. The GPS satellite orbit calculated from downloaded IGS file and the flight trajectory acquired from applanix file can be used to predict the azimuth and elevation at each time step for each PRN in the list provided by sv_chans.dat. By setting up the threshold on elevation and the time period, the available PRN list for each PRN along with their range of time in terms of sec of week and GRS file number can be acquired and saved in the occtab.out. In this output file, all the details of the available satellites will be listed, including setting/rising determination, occultation start time and end time, and when the specific PRN will show up in either prediction or GRS data. The user can decide which PRN they would like to investigate further by using the information given by the list and put their decision into the input file in the next module. In this way the channel needed for OL tracking can be allocated before the process begins.

B.1.3 olpredict_dopp

INPUT:

- oldopp.inp
- occtab.out
- Applanix file
- IGS file

OUTPUT:

- OLPredictSVxx.in
- ClimateSVxx.in

This module makes the Doppler and climatological phase prediction for each PRN that user requested. The CIRA-Q model and the ROSAP ray tracing program are called in the script to calculate the excess phase under the refractivity profile model. The signal transmission time has also been considered for geometry phase calculation in coordinate transformation. The calculated phase prediction will be saved in two output files.

B.1.4 psr_ol

INPUT:

- psrol.inp
- OLPredictSVxx.in
- ClimateSVxx.in
- sv_chans.dat

- Bit archive

OUTPUT:

- DataBitSVxx.in
- OLPredictSVxx.out
- Chanxx.dat

This is the main module doing OL tracking and output the correlation result between the received GRS data and the phase prediction. The OL tracking details and the algorithm used in this module are described in Chapter 3. Note that the bit archive is used at this stage for reading and rewriting to the new format. The error detection and reconstruction process of the downloaded data bit archive will be described in the next section.

B.2 Databit preprocessing

There are 2 parity bits in the data bit file name given by the downloaded bit archive which can be used as the indication of error in the file. Once the error in the certain file has been confirmed, the data bit reconstruction process can be used to remove the invalid bit and rebuild the bit file. The idea is that most data bits transmitted by GPS satellites are repeating itself in a limited time frame, thus the data bit in the next or the previous block can be utilized to reconstruct the data. The data message structure of the GPS signal is shown in Figure B.2.

The data message, which can be divided in to different "frames", of the GPS signal is transmitted at 50Hz bit rate. Each frame contains 30 sec of data (which means 1500 bits), and can be divided further by 5 subframes (which means 300 bits). The first 3 subframes contains the satellite health and the ephemeris data which will be repeated every in every frame until about 2 hours. The almanac data which will be repeated every 12.5 minutes until several days away is stored in the last two subframes. The repeating characteristic of the GPS signal can be used to reconstruct the incomplete or fault data in bit archive.

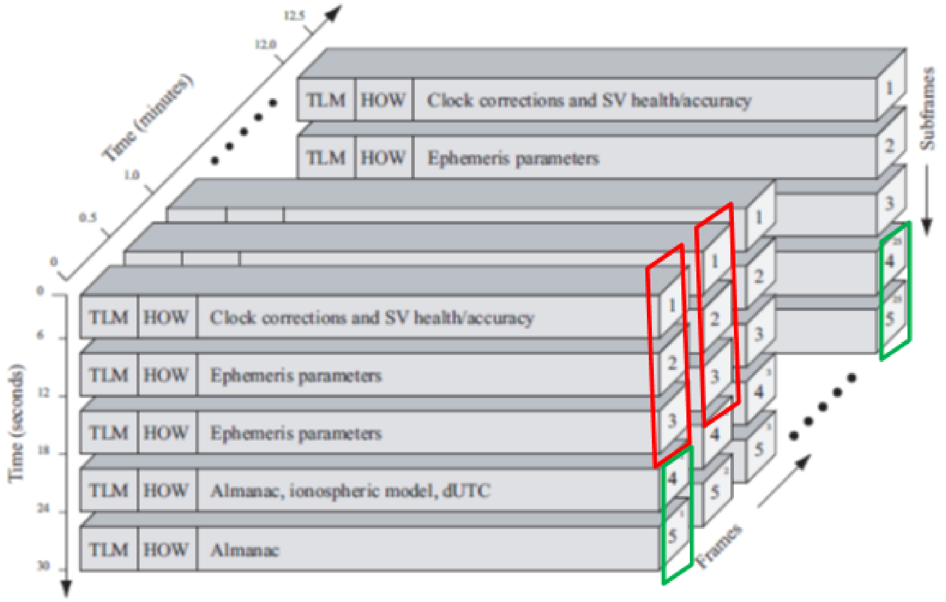

Figure B.2. The data message structure of the GPS signal. Red block is the satellite health and the ephemeris data which will be repeated every 30 sec. The green block is the almanac data which will be repeated every 12.5 minutes. This figure is modified from the figure in [61].

The only problem is that the word ”HOW” in each subframe is not going to repeat itself, which should be calculated independently by transmitting time. Therefore, the reconstruction process will be executed as follows:

- Identify the faulty bit file - which is one of the bit message frame.
- Determine if the reconstruction is possible:
  - Search the closest frame that contains normal (or healthy) first 3 subframe bits. If they are too far from the injured data (¿30 minutes) then the data will not be used and the recontruction fails.
  - Search the closest frame that contains normal (or healthy) last 2 subframe bits which has 12.5 minutes interval. If they are too far from the injured data (¿2 hours) then the data will not be used and the recontruction fails.

- If the reconstruction is feasible and the source frames are identified, replace the targeted subframes from those two source frames.
- Calculate the "HOW" word by using Zcount from the previous or next frame.

By using this strategy most error bit archive can be reconstructed and significantly decrease the error rate in OL tracking. An obvious example is shown in the Figure B.3. It can be seen that error bit file will cause SNR drop to noise level at about 16.948 hour, while the SNR is greatly improved by using the reconstructed data bit files.

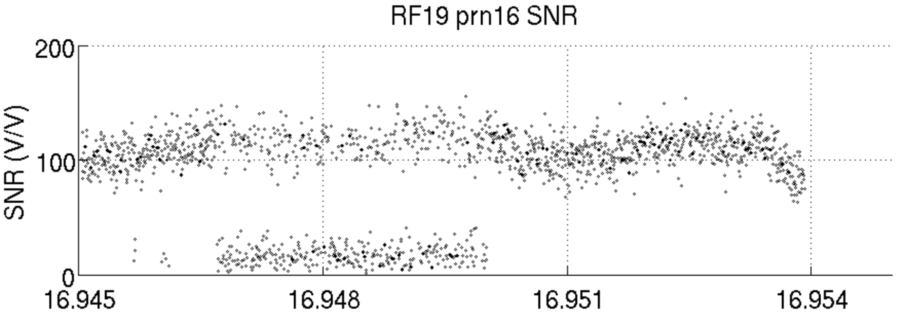

(a) zoom out

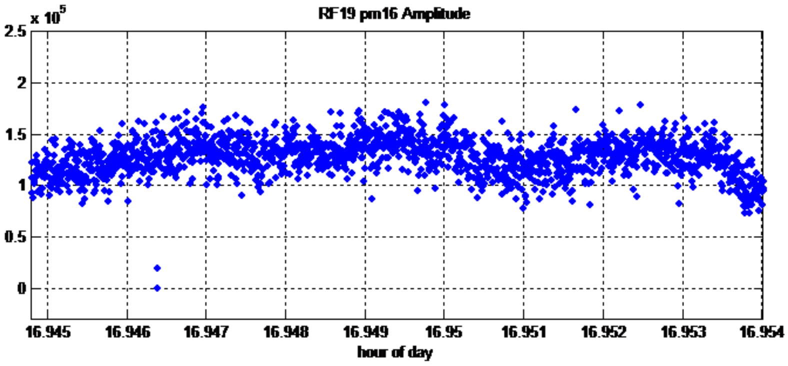

(b) zoom in

Figure B.3. The improvement of the reconstruction data bit files. (a) Original SNR using error data bit file (b) New SNR using reconstructed data bit file

VITA

VITA

Kuo-Nung Wang was born in Taipei, Taiwan. He grew up in Taichung city, Taiwan and attended National Chenh Kung University (NCKU) In Tainan, Taiwan. He received a B.A. and a M.S. degree in electrical engineering from NCKU. He began as a doctoral student in the School of Aeronautics and Astronautics in the fall of 2010, working under the supervision of his major professor, Dr. Jame L. Garrison. His dissertation defense was in the Fall of 2015 and he anticipates receiving a Ph.D. in December, 2015.